ISSN: 2150-4091 (Print), 2150-4105 (Online) Volume 2, Number 1, January 2010

Scientific Research

Natural Science

www. scirp. org/journal/ns/

Editor-in-Chief
Kuo-Chen Chou

Journal Editorial Board

ISSN: 2150-4091 (Print) ISSN: 2150-4105 (Online)
http://www.scirp.org/journal/ns/

Editor-in-Chief

Prof. Kuo-Chen Chou Gordon Life Science Institute, San Diego, California, USA

Managing Executive Editor

Dr. Feng Liu Scientific Research Publishing, USA Email: fengliu@scirp.org

Managing Production Editor

Fiona Qu Scientific Research Publishing, USA Email: ns@scirp.org

Editorial Advisory Board

Prof. James J. Chou Harvard Medical School, USA
Prof. Reba Goodman Columbia University, USA
Dr. Robert L. Heinrikson Proteos, Inc., USA
Prof. Robert H. Kretsinger University of Virginia, USA
Dr. P. Martel Chalk River Laboratories, AFCL Research, Canada
Dr. Michael Mross Vermont Photonics Technologies Corp., USA
Prof. Harold A. Scheraga Baker Laboratory of Chemistry, Cornell University, USA

Editorial Board

Fridoon Jawad Ahmad University of the Punjab, Pakistan
Giangiacomo Beretta University of Milan, Italy
Bikas K. Chakrabarti Saha Institute of Nuclear Physics, India
Dr. Brian Davis Research Foundation of Southern California, USA
Mohamadreza Baghaban Eslaminejad Cell Sciences Research Center, Royan Institute, Iran
Dr. Marina Frontasyeva Frank Laboratory of Neutron, Russia
Neelam Gupta National Bureau of Animal Genetic Resources, India
Dr. Yohichi Kumaki Institute for Antiviral Research, Utah State University, USA
Dr. Petr Kuzmic BioKin Ltd., USA
Dr. Ping Lu Communications Research Centre, Canada
Dimitrios P. Nikolelis University of Athens, Greece
Caesar Saloma University of the Philippines Diliman, Philippines
Prof. Kenji Sorimachi Dokkyo Medical University, Japan
Swee Ngin Tan Nanyang Technological University, Singapore
Dr. Fuqiang Xu National Magnetic Resonance Research Center, China
Dr. W.Z. Zhong Pfizer Global Research and Development, USA

Guest Reviewers (According to Alphabet)

Salvador Alfaro
Takayuki Ban
Marina FRONTASYEVA
Rafael Luque
Fan Peng
Mohd.Yusri bin Abd.Rahman
Ruediger Schweiss
Shahida Waheed
Jamshed Hussain Zaidi
Nenghui Zhang
Hongzhi Zhong
Junwu Zhu

TABLE OF CONTENTS

Volume 2, Number 1, January 2010

Predicting numerically the large increases in extra pressure drop when Boger fluids flow through axisymmetric contractions

H. R. Tamaddon-Jahromi, M. F. Webster, K. Walters.....1

Synthesis of nano crystalline spatulae of lead zirconate titanate ($PbZr_{0.52}Ti_{0.48}O_3$)

S. S. Bhatt, S. C. Chaudhry, N. Sharma, S. Gupta.....12

Hydriding and dehydriding kinetics of melt spun nanocrystalline $Mg_{20}Ni_{10-x}Cu_x$ (x=0-4) alloys

Y. H. Zhang, D. L. Zhao, B. W. Li, H. P. Ren, S. H. Guo, X. L. Wang.....18

Study of some Indian medicinal plants by application of INAA and AAS techniques

R. Lokhande, P. Singare, M. Andhele, R. Acharya.....26

Toxicity evaluation of produced formation waters after filtration treatment

L. Manfra, C. Maggi, J. Bianchi, M. Mannozzi, O. Faraponova, L. Mariani, F. Onorati, A. Tornambè, C. V. Lamberti, E. Magaletti.....33

Review on nano-drugs

Y. Liu, T. S. Niu, L. Zhang, J. S. Yang.....41

Face recognition based on manifold learning and Rényi entropy

W. M. Cao, N. Li.....49

Relationship between normalized thermal energy and conductivity for cylindrical tokamak geometry

M. Asif.....54

Research of handwriting detecting system for space pen

Z. Y. Gao, D. S. Li, W. Wang, C. J. Yang.....56

Photocurrents induced by stimulated absorption of light

A. Kavokin, G. Eramo.....63

SciRes Copyright © 2010

Natural Science

Journal Information

SUBSCRIPTIONS

The *Natural Science* (Online at Scientific Research Publishing, www.SciRP.org) is published monthly by Scientific Research Publishing, Inc., USA.

E-mail: service@scirp.org

Subscription rates: Volume 2 2010

Print: $50 per copy.

Electronic: free, available on www.SciRP.org.

To subscribe, please contact Journals Subscriptions Department, E-mail: service@scirp.org

Sample copies: If you are interested in subscribing, you may obtain a free sample copy by contacting Scientific Research Publishing, Inc at the above address.

SERVICES

Advertisements

Advertisement Sales Department, E-mail: service@scirp.org

Reprints (minimum quantity 100 copies)

Reprints Co-ordinator, Scientific Research Publishing, Inc., USA.

E-mail: service@scirp.org

COPYRIGHT

Copyright© 2010 Scientific Research Publishing, Inc.

All Rights Reserved. No part of this publication may be reproduced, stored in a retrieval system, or transmitted, in any form or by any means, electronic, mechanical, photocopying, recording, scanning or otherwise, except as described below, without the permission in writing of the Publisher.

Copying of articles is not permitted except for personal and internal use, to the extent permitted by national copyright law, or under the terms of a license issued by the national Reproduction Rights Organization.

Requests for permission for other kinds of copying, such as copying for general distribution, for advertising or promotional purposes, for creating new collective works or for resale, and other enquiries should be addressed to the Publisher.

Statements and opinions expressed in the articles and communications are those of the individual contributors and not the statements and opinion of Scientific Research Publishing, Inc. We assumes no responsibility or liability for any damage or injury to persons or property arising out of the use of any materials, instructions, methods or ideas contained herein. We expressly disclaim any implied warranties of merchantability or fitness for a particular purpose. If expert assistance is required, the services of a competent professional person should be sought.

PRODUCTION INFORMATION

For manuscripts that have been accepted for publication, please contact:

E-mail: ns@scirp.org

Vol.2, No.1, 1-11 (2010)
doi:10.4236/ns.2010.21001

Natural Science

Predicting numerically the large increases in extra pressure drop when boger fluids flow through axisymmetric contractions

H. R. Tamaddon-Jahromi[1], M. F. Webster[1*], K. Walters[2]

[1]Institute of Non-Newtonian Fluid Mechanics, School of Engineering, Swansea University, Swansea, UK; m.f.webster@swan.ac.uk
[2]Institute of Mathematics and Physics, University of Aberystwyth, Aberystwyth, UK

Received 10 October 2009; revised 3 November 2009; accepted 5 November 2009.

ABSTRACT

Recent numerical studies on pressure-drops in contraction flows have introduced a variety of constitutive models to compare and contrast the competing influences of extensional viscosity, normal stress and shear-thinning. Early work on pressure-drops employed the constant viscosity Oldroyd-B and Upper Convected Maxwell (UCM) models to represent the behavior of so-called Boger fluids in axisymmetric contraction flows, in (unsuccessful) attempts to predict the very large enhancements that were observed experimentally. In more recent studies, other constitutive models have been employed to interpret observed behavior and some progress has been made, although finding a (respectable) model to describe observed contraction-flow behavior, even qualitatively, has been frustratingly difficult. With this in mind, the present study discusses the ability of a well-known FENE type model (the so-called FENE-CR model) to describe observed behavior. For various reasons, an axisymmetric (4:1:4) contraction/expansion geometry, with rounded corners, is singled out for special attention, and a new hybrid finite element/volume algorithm is utilized to conduct the modeling, which reflects an incremental pressure-correction time-stepping structure. New to this algorithmic formulation are techniques in time discretization, discrete treatment of pressure terms, and compatible stress/velocity-gradient representation. We shall argue that the current simulations for the FENE-CR model have resulted in a major improvement in the sort-for agreement between theory and experiment in this important bench-mark problem.

Keywords: Contraction Flows; Extra Pressure Drop; Numerical Simulation; Extensional Viscosity; Normal Stress Differences

1. INTRODUCTION

In the early days of Computational Rheology, the so-called Upper-Convected Maxwell (UCM) and Oldroyd-B models were strongly favored. This was partly due to the fact that they were assumed to be the 'bottom-line' of acceptable mathematical simplicity, whilst also being able to mimic the complex rheometrical behavior for a class of dilute polymer solutions known as Boger fluids, which became popular in the late 1970s. (A Boger fluid has a reasonably constant shear viscosity, a high extensional viscosity as the extensional strain rate increases, and a high first normal stress difference, which has a quadratic dependence on shear rate at low to moderate shear rates, before becoming weaker than quadratic at higher shear rates.)

It is well known that simulations for the UCM and Oldroyd B models failed to predict the large increases in the so-called Couette correction (or equivalently the "extra pressure difference" (*epd*)) in axisymmetric contraction flows. Interestingly, the work of Debbaut and Crochet [1], Debbaut *et al*. [2] and Binding [3] already provided strong hints as to the likely cause of the inadequacies of these models in predicting the observed increases in excess pressure drop (*epd*) found in experimental work.

On the experimental side, Nigen and Walters [4] found significant differences in pressure-drop between Boger and Newtonian liquids with the same shear viscosity for axisymmetric contraction flow. (However, no distinction could be drawn between corresponding pressure drops for Newtonian and Boger fluids in planar configurations). Around the same time, Rothstein and McKinley [5] switched attention to axisymmetric contraction/expansion geometries of various contraction ratios (between two and eight), various degrees of re-

SciRes Copyright © 2010

ntrant corner curvature, and covering a large range of Deborah numbers. In this work, large Couette corrections were observed above that for a Newtonian fluid. These were independent of contraction ratio and re-ntrant corner curvature.

So, the increase in the Couette correction for Boger fluids flowing in various axisymmetric contractions can be very high. These experimental observations clearly presented theoretical (computational) rheologists with several significant challenges, some of which have already been resolved (see for example, Phillips and Williams [6]; Aboubacar *et al*. [7]; Walters and Webster [8]; Alves *et al*. [9]).

The present paper is a continuation of our previous works (Aguayo *et al*. [10]; Walters *et al*. [11-13], in predicting pressure-drops for Boger fluids in expansion-contraction flow. As a general conclusion from our earlier findings (particularly those in Walters *et al*. [12,13]), our numerical simulations confirmed earlier comments by Binding [3] and Debbaut and Crochet [1] that, whereas high extensional viscosity levels can give rise to large increases in the so-called *epd*, increasing normal-stress difference levels can have the opposite effect. Moreover, in Walters *et al*. [12,13], we attempted to show how generalizations of the so-called White-Metzner model (White and Metzner [14]) can help rheologists to understand the competing influence of the various rheometrical functions on important flow characteristics.

In this paper, a further numerical study of the 4:1:4 expansion/contraction (adopted in Rothstein and McKinley [5], and Szabo *et al*. [15]) is made, and the effect on the excess pressure drop *(epd*) analyzed. In particular, we employ the FENE-type model proposed by Chilcott and Rallison [16], useful for its constant shear viscosity and bounded extensional characteristics. As in previous work, we attempt to relate the observed behavior of highly-elastic Boger fluids in complex flows to their rheometrical behavior.

1.1. Rheometrical Functions

In this communication, we shall be referring frequently to two important 'rheometrical' flows, namely steady simple shear flow and extensional flow. In the former, there is flow only in the x direction and this depends simply and linearly on the *y* coordinate. i.e.

$$v_x = \dot{\gamma} y, \quad v_y = v_z = 0 \tag{1}$$

where v_i is the velocity vector and $\dot{\gamma}$ is the constant shear rate.

For a non-Newtonian elastic liquid, the stress tensor components σ_{ik} can be conveniently written in the form:

$$\begin{aligned} \sigma_{xy} &= \sigma = \dot{\gamma}\eta(\dot{\gamma}) \\ \sigma_{xx} - \sigma_{yy} &= N_1(\dot{\gamma}) \\ \sigma_{yy} - \sigma_{zz} &= N_2(\dot{\gamma}) \end{aligned} \tag{2}$$

where σ is the shear stress, η is the shear viscosity and N_1 and N_2 are the so-called first and second normal stress differences, respectively (see, for example, Barnes *et al*. [17]).

For a Newtonian fluid, the stress distribution simply involves one material constant–the coefficient of viscosity η and the two normal stress differences are zero. In the case of a non-Newtonian elastic liquid, η can now be a function of the shear rate, with so-called 'shear thinning' the most commonly observed behavior. Also, both normal stresses are of potential importance, particularly N_1.

A typical Boger fluid would be a dilute (often a very dilute) solution of a high molecular weight polymer in a very viscous 'Newtonian' solvent. Usually, the shear viscosity is constant for such fluids; N_1 is often higher than the shear stress σ, indicating that the fluid is in the "highly-elastic" category. N_2 is invariably found to be much smaller than N_1 and, in many (most) computational studies, N_2 is taken to be zero.

At this point, it is important to stress that, from a continuum mechanics standpoint, the initial dependence of N_1 on $\dot{\gamma}$ has to be quadratic and there is experimental evidence that this quadratic dependence can persist over a reasonable range of shear rates. However, there is also rheometrical evidence available that the dependence of N_1 on $\dot{\gamma}$ can become weaker than quadratic as the shear rate increases further. This is sometimes accompanied by slight shear thinning. For example, in a comprehensive study entitled "A rheometrical study of Boger fluids", Jackson *et al*. [18] concluded "It will be seen that over a range of shear rates, σ is a linear function of $\dot{\gamma}$ and N_1 is a quadratic function of $\dot{\gamma}$, but that there is a departure from this second-order behavior at the high shear rates".

The second rheometrical flow of importance in the present study is that called 'uniaxial extensional flow', with a velocity field which can be expressed as

$$v_x = \dot{\varepsilon} x, \quad v_y = -\frac{\dot{\varepsilon} y}{2}, \quad v_z = -\frac{\dot{\varepsilon} z}{2} \tag{3}$$

where $\dot{\varepsilon}$ is the so-called extensional strain rate. We can write the corresponding stress distribution in the form:

$$\sigma_{xx} - \sigma_{yy} = \sigma_{xx} - \sigma_{zz} = \dot{\varepsilon}\eta_E(\dot{\varepsilon}) \tag{4}$$

where η_E is the 'extensional viscosity'. For a Newtonian fluid, $\eta_E = 3\eta$, a result first obtained by Trouton over a hundred years ago (see, for example, Tanner and

SciRes Copyright © 2010

Walters [19]). For this reason, the ratio between the two viscosities is called the 'Trouton ratio T_R', and this clearly takes the value 3 for a Newtonian fluid. For a non-Newtonian elastic fluid, T_R can be significantly higher than 3, with 'orders of magnitude' increases not uncommon.

From the above discussion and the relevant literature, we can associate the following rheometrical behavior with Boger fluids:

1) A reasonably constant shear viscosity η.

2) A potentially high extensional viscosity η_E as the extensional strain rate increases.

3) A high first normal stress difference N_1, which has a quadratic shear rate dependence on $\dot{\gamma}$, at least for small to moderate shear rates.

4) A second normal stress difference N_2 which is negative and at most one tenth of the magnitude of N_1. It is often taken as zero in computational studies.

Clearly, any constitutive model that we use to describe Boger fluids has to satisfy (1)-(4), at least in a semi-quantitative sense.

2. THE CONTRACTION/EXPANSION PROBLEM

In conventional contraction flow, liquids are forced through a contraction under a pressure gradient. At specific locations on the walls, upstream and downstream of the contraction, pressure measurements are made. These locations must be far enough away from the contraction for the flows to be deemed to be unaffected by the contraction, i.e. we may consider the flows to be 'fully developed' and 'Poiseuille like' at the pressure-measurement stations.

In contraction flows, there is often significant interest in the *kinematics* of the flow structure, particularly the vortices which provide computational rheologists with significant challenges (see, for example, Walters and Webster [8]). However, in the present work, we shall confine attention to the *dynamics* of the flow, which is often studied through the so-called Couette correction C, defined by

$$C = \left[\Delta p - \Delta p_u L_u - \Delta p_d L_d \right] / 2\sigma_w \qquad (5)$$

Here, Δp is the total pressure difference between the inlet and outlet transducers, Δp_u is the fully-developed pressure gradient in the upstream section, Δp_d is the fully-developed pressure gradient in the downstream section, L_u and L_d are their respective lengths, σ_w is the fully-developed wall shear stress in the downstream channel.

The Couette correction C is usually plotted as a function of the Deborah number

$$\text{De} = \lambda \dot{\gamma}_w \qquad (6)$$

λ is a characteristic relaxation time and $\dot{\gamma}_w$ is the shear-rate at the downstream wall.

In this paper, the Deborah number is defined as De= $\lambda \dot{\gamma}_{avg}$, where $\dot{\gamma}_{avg}$ is the average shear-rate in the constriction zone.

An alternative measure of 'resistance to flow' is the so-called Excess Pressure Drop (*epd*), defined by Binding *et al*. [20].

$$p^* = \frac{\left(\Delta p - \Delta p_{fd}\right)_B}{\left(\Delta p - \Delta p_{fd}\right)_N}, \quad \Delta p_{fd} = \Delta p_u L_u + \Delta p_d L_d \qquad (7)$$

In this form, p^* can be equated to the ratio of Couette corrections for constant-viscosity Boger and Newtonian fluids, with corresponding wall shear stress.

The subscripts N and B represent the corresponding Newtonian and Boger fluid values, respectively, when these are applicable.

In our recent computational work on contraction flows (Walters *et al*. [11-13,21]), we decided to concentrate on the related contraction-expansion (4:1:4) geometry, with rounded corners (see **Figure 1**).

We did this for a number of different reasons. For example:

1) We found the geometry to be far easier to handle in the computations than the conventional 4:1 geometry with sharp corners. Pressure differences were an order of magnitude lower for the 4:1:4 geometry than with 4:1 geometry flows, with shorter downstream distances demanded to establish relaxed stress beyond the constriction (see also Szabo *et al*. [15] for FENE results). We have certainly been able to reach higher values of the Deborah number in the simulations. Furthermore, application of the basic numerical method was already well developed in the Swansea research group.

2) Importantly, experimental data for the 4:1:4 geometry had been supplied by McKinley and his co-workers (see, for example, Rothstein and McKinley

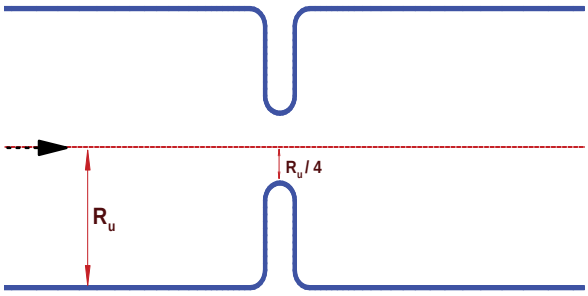

Figure 1. Schematic diagram of contraction-expansion geometry.

SciRes Copyright © 2010

[5]). These showed the same trends as those already well known in the conventional 4:1 geometry. Of major importance was the appearance in the Rothstein and McKinley experiments of substantial increases in the *epd* for increasing Deborah numbers in the case of Boger fluids.

3. CONSTITUTIVE EQUATIONS

We now need to address the question of choosing appropriate constitutive equations for the Boger fluids, which we shall concentrate on in this publication.

Confining attention to incompressible fluids, we can write the Cauchy stress tensor σ_{ik} in the form:

$$\sigma_{ik} = -p\delta_{ik} + T_{ik} \tag{8}$$

where p is an arbitrary isotropic pressure, δ_{ik} the Kronecker delta, and T_{ik} is the so-called extra-stress tensor.

Constitutive equations relate the extra-stress tensor T_{ik} to a suitable kinematic variable such as the rate-of-strain tensor d_{ik}. For two specific but very different reasons, it is often convenient to introduce a so- called "stress splitting":

$$T_{ik} = T_{ik}^{(1)} + T_{ik}^{(2)} \tag{9}$$

and to write $T_{ik}^{(1)}$ as a Newtonian contribution

$$T_{ik}^{(1)} = 2\eta_1 d_{ik} \tag{10}$$

Computational rheologists have often found that the introduction of the Newtonian component can greatly assist in the numerical simulation of complex flows, and experimental rheologists, particularly those working with Boger fluids, have also found the modification to be useful. They invariably associate η_1 with the solvent viscosity.

As an example of this stress splitting, consider the well-known Oldroyd B model, with constitutive equations are usually expressed in the form:

$$T_{ik} + \lambda_1 \overset{\nabla}{T}_{ik} = 2\eta_0 \left[d_{ik} + \lambda_2 \overset{\nabla}{d}_{ik} \right] \tag{11}$$

where the triangle denotes the usual upper-convected time derivative introduced by Oldroyd [22].

It is often convenient to write this equation in the form:

$$\begin{aligned} T_{ik}^{(1)} &= 2\eta_0 \beta d_{ik} \\ T_{ik}^{(2)} + \lambda_1 \overset{\nabla}{T}_{ik}^{(2)} &= 2\eta_0 (1-\beta) d_{ik} \end{aligned} \tag{12}$$

where $\beta = \lambda_1 / \lambda_2$.

For the Boger fluids, which have been used in many fundamental experimental contraction-flow studies (see, for example, Boger and Walters [23]), the polymer contribution to the total viscosity is very low. This is dominated by the solvent contribution, so that β is usually in the range 0.9 to 0.95, or even higher.

The important rheometrical functions for the Oldroyd B model are given by

$$\begin{aligned} &\eta = \eta_0, \\ &\mathrm{N}_1 = 2\eta_0 (1-\beta)\lambda_1 \dot{\gamma}^2, \quad \mathrm{N}_2 = 0, \\ &\eta_E = 3\beta\eta_0 + 3(1-\beta)\eta_0 \left[\frac{1}{1-\lambda_1 \dot{\varepsilon} - 2\lambda_1^2 \dot{\varepsilon}^2} \right] \end{aligned} \tag{13}$$

We see that the Oldroyd B model predicts a constant shear viscosity η_0, a quadratic first normal stress difference N_1, a zero second normal stress difference N_2, and a potentially high extensional viscosity η_E. In fact, η_E reaches an infinite value at a finite value of the extensional strain rate $\dot{\varepsilon}$.

As we have indicated, shear thinning is (virtually) absent in Boger fluids. Furthermore, the uniaxial extensional viscosity levels can be very high indeed. These factors have been the main reasons for the popularity of the Oldroyd B model in Computational Rheology studies for Boger fluids. The relative simplicity of the model has been another factor of importance.

However, at this point, it needs to be stressed again that all existing simulations for the Oldroyd B have been unable to predict the large increases in the Couette correction found when Boger fluids flow through axisymmetric contraction/expansion flows (see, for example Walters *et al*. [11-13]).

With this in mind, Walters *et al*. [12,13] introduced some new constitutive models to help elucidate the situation. These were in part guided by ideas put forward by Debbaut and Crochet (see Debbaut and Crochet [1] and Debbaut *et al*. [2]). In these papers, use was made of two rate-of-strain invariants, which we shall conveniently refer to as $\dot{\gamma}$ and $\dot{\varepsilon}$ in what follows:

$$\dot{\gamma} = 2\sqrt{\mathbf{II}_d}, \quad \dot{\varepsilon} = 3\mathbf{III}_d / \mathbf{II}_d \tag{14}$$

Here, $\mathbf{II}_d$ and $\mathbf{III}_d$ are the two nonzero invariants of the rate of strain tensor d_{ik} in their usual form:

$$\mathbf{II}_d = \frac{1}{2}\mathrm{tr}\left(\boldsymbol{d}^2\right), \quad \mathbf{III}_d = det\left(\boldsymbol{d}\right) \tag{15}$$

The reason for the choice (14) instead of (15) has been fully explained by Debbaut and Crochet [1] and Debbaut *et al*. [2]. Clearly, the invariant $\dot{\gamma}$ reduces to the usual shear rate in a steady simple shear flow and the invariant $\dot{\varepsilon}$ reduces to the usual extensional strain rate in a uniaxial extensional flow. Hence, the reason for the notation, Walters *et al*. [12,13] introduced four constitutive models that they defined as A-D, all of which have the structure introduced in **Eqs.8** to **10**.

SciRes Copyright © 2010

Model A is simply the Newtonian fluid with $T_{ik}^{(2)}$ given by

$$T_{ik}^{(2)} = 2\eta_0(1-\beta)d_{ik} \tag{16}$$

Model D is the Oldroyd B model we have already introduced in **Eqs.11** and **12** with rheometrical functions given in **Eq.13**.

Models B and C can be seen as extensions of the models GNM1 and UCM1 in the Debbaut *et al*. [2] papers. B is an inelastic model with $T_{ik}^{(1)}$ given as in **Eq.12** and

$$T_{ik}^{(2)} = \frac{2\eta_0(1-\beta)\,d_{ik}}{\left(1-\lambda_1\dot{\varepsilon}-2(\lambda_1\dot{\varepsilon})^2\right)} \tag{17}$$

The rheometrical functions for model B are

$$\begin{aligned} &\eta = \eta_0, \\ &\mathrm{N}_1 = 0, \\ &\eta_E = 3\beta\eta_0 + 3(1-\beta)\eta_0\left[\frac{1}{1-\lambda_1\dot{\varepsilon}-2\lambda_1^2\dot{\varepsilon}^2}\right] \end{aligned} \tag{18}$$

i. e. the same η and η_E as the Oldroyd B model, but with N_1=0.

Model C has viscoelastic properties with $T_{ik}^{(1)}$ given as in **Eq.12** and

$$\begin{aligned} &T_{ik}^{(2)} + \lambda_1 \overset{\nabla}{T}_{ik}^{(2)} = 2\eta(\dot{\gamma},\dot{\varepsilon})\,d_{ik}, \\ &\eta(\dot{\gamma},\dot{\varepsilon}) = \eta_0(1-\beta)\left(1-\lambda_1\dot{\varepsilon}-2(\lambda_1\dot{\varepsilon})^2\right) \end{aligned} \tag{19}$$

In this case, the rheometrical functions are

$$\begin{aligned} &\eta = \eta_0, \\ &\mathrm{N}_1 = 2\eta_0(1-\beta)\lambda_1\dot{\gamma}^2, \quad \mathrm{N}_2 = 0, \\ &\eta_E = 3\eta_0. \end{aligned} \tag{20}$$

This time it is η and N_1 that match the expressions for the Oldroyd B model, but η_E now has the Newtonian expression.

Model C can be viewed as a "Generalized White-Metzner model" (see, for example Walters *et al*. [12]).

The benefit of having the four A-D models available was that it allowed us the luxury of the following comparisons:

1) A comparison of the simulations for models A and B provided an indication of the effect of extensional viscosity on flow characteristics, since $\eta = \eta_0$ and N_1= 0 for both models.

2) A comparison of the simulations for models A and C provided an indication of the effect of "normal stresses" on flow characteristics, with a "Newtonian" extensional viscosity in both.

3) A comparison of the simulations for models B and C provided an indication of the relative strengths of normal stress and extensional viscosity effects on flow characteristics.

4) A comparison of the simulations for models C and D (i.e. the Oldroyd B model) highlighted further the effect of a high extensional viscosity in the case of elastic liquids.

5) Lastly, a comparison of the simulations for models B and D highlighted further the normal stress effect, keeping in mind however that, in this comparison, model B is inelastic and model D is viscoelastic.

We felt that numerical simulations for the four constitutive models (A-D) could throw considerable light on the influences of the various rheometrical functions on flow characteristics.

We show in **Figure 2** simulations for the contraction/expansion geometry provided by Walters *et al*. [12,13]. We summarize their findings here, as these have been fundamental and serve as a basis for the present study, where a number of additional factors are taken into account.

The respective simulations of **Figure 2** for the four constitutive models (A-D) demonstrate the influence of the various rheometrical functions on excess pressure drop (*epd*) read against increasing deformation rate (De). A comparison of models A to B shows the increasing effect that extensional-viscosity alone has on *epd*, as both models support vanishing N_1. Alternatively, under constant extensional viscosity, a comparison of models A to C indicates that the increasing influence of normal stress difference can give rise to the opposite effect, that is a decrease in *epd* (as suggested in Binding [3]).

3.1. Comparison of Results for Models B and D

Taking this comparison one step further we may contrast the *epd* results for model B with those for model D (Oldroyd B). Here, we note that the Oldroyd B model reflects the same extensional viscosity as model B (an example of extreme strain-hardening), but with a non-zero normal stress difference of quadratic variation in shear rate (so, $\boldsymbol{N_1}\neq 0$). Model D is often used to approximate experimental results for Boger fluids, due to its constant shear viscosity and strain-hardening properties. Consistent with the above, the results again demonstrate a decline in *epd* from model B to model D, this being associated with the associated rise in $\boldsymbol{N_1}$. We note in addition, that there is the usual upper limit on *De* attainable in the simulations for model D (attributed to the unbounded nature of η_e). Here, there is a slight dip in *epd* before reaching the limiting value at the Newtonian reference line (for this level of solvent fraction, 0.9), which lies disappointingly short of the large positive *epd* experimental expectations reported for Boger fluids (Nigen and Walters [4]; Rothstein and McKinley [5]).

SciRes Copyright © 2010

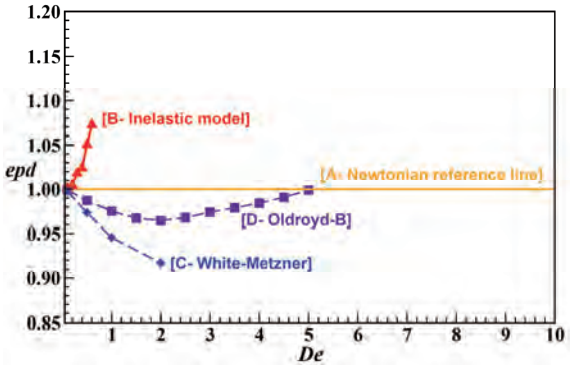

Figure 2. Normalized pressure drop (*epd*) vs. De(= $\lambda\dot{\gamma}_{avg}$) for models A-D (cf. Walters *et al*. [12,13]), β=0.9.

3.2. Comparison of Results for Models C and D

Following this line of study, a direct comparison of *epd* results for models C and D, both of which share the same quadratic N_1 behavior, represents the effects of extensional viscosity alone (recall that model C bears a constant extensional viscosity). Here, once again, we discern an increase in *epd* from model C to that for model D.

Clearly, the simulations for models A-D contained in **Figure 2** provide insights into the possibility of providing numerical simulations which match the experimental data, at least in a semi-quantitative sense. However, we still lack definitive evidence that simulations for a (respectable) constitutive equation, which would have general acceptance, can provide the required agreement between experiment and theory. Hence the reason and motivation for the present work.

We require a model that leads to a constant shear viscosity and possesses other rheometrical features of relevance to Boger-type fluids (also, vanishing N_2, see Chilcott and Rallison [16]). For this reason, we have alighted on the so-called FENE-CR (Finite Extendible Nonlinear Elasticity-Chilcott and Rallison [16]) model, which we shall conveniently refer to as model E. This has the following constitutive equations:

$$T_{ik} = T_{ik}^{(1)} + T_{ik}^{(2)}$$

$$T_{ik}^{(1)} = 2\eta_1 d_{ik} \tag{21}$$

$$T_{ik}^{(2)} = \frac{(1-\beta)\, f(Tr(A))(A-I)}{\lambda_1}$$

where the stress is expressed through a conformation transformation (**A**) as

$$f(Tr(A))A + \lambda_1 \overset{\nabla}{A} + f(Tr(A))I = 0 \tag{22}$$

The stretch function $f(Tr(A))$ depends on L (the so-called extensibility parameter), and is given by:

$$f(Tr(A)) = \frac{1}{1 - Tr(A)/L^2} \tag{23}$$

In this equation, $Tr(A)$ is the trace operator and L essentially measures the size of the polymer molecule in relation to its equilibrium size. I is the identity tensor.

The associated rheometrical functions are given by

$$\eta = \eta_0$$

$$N_1 = \frac{2\eta_0(1-\beta)\lambda_1\dot{\gamma}^2}{f^2}, \quad N_2 = 0 \tag{24}$$

$$\eta_e = 3\beta\eta_0 + 3(1-\beta)\eta_0\left[\frac{f}{f^2 - f\lambda_1\dot{\varepsilon} - 2\lambda_1^2\dot{\varepsilon}^2}\right]$$

where $f = f(Tr(A))$ is defined in **Eq.23**.

The rheometrical response of the FENE-CR model is displayed in **Figures 3** and **4**. The model predicts a constant shear viscosity, but the first normal stress difference (N_1) is weaker than the strong quadratic form exhibited by the Oldroyd-B model. One notes, however, that predictions for large values of the extensibility parameter (L>100) asymptote to Oldroyd-B behavior in N_1 and η_e. For small values of L (e.g. L=3), significant departure in N_1 is observed from an Oldroyd-B response. A monotonic decline in N_1 is apparent with decreasing L (**Figure 3**).

The extensional viscosity behavior of the FENE- CR model for low extensional strain-rates up to 0.5 is practically identical to that for the Oldroyd-B model. Beyond this station, the extensional viscosity for the FENE-CR model is capped, with the limiting level of the extensional viscosity plateau depending on the elevation of L. This is illustrated in **Figure 4**, where the trend in extensional viscosity for the FENE-CR model is almost flat for L=3. There is advancing earlier departure from Oldroyd-B trends with appropriate choices of L.

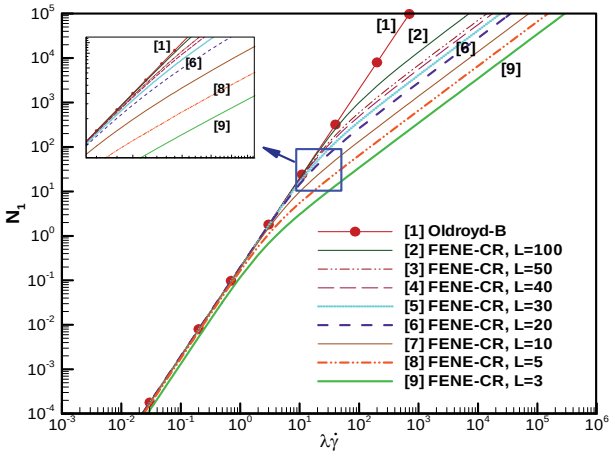

Figure 3. Normal stress data for model E (FENE-CR), increasing L.

SciRes Copyright © 2010

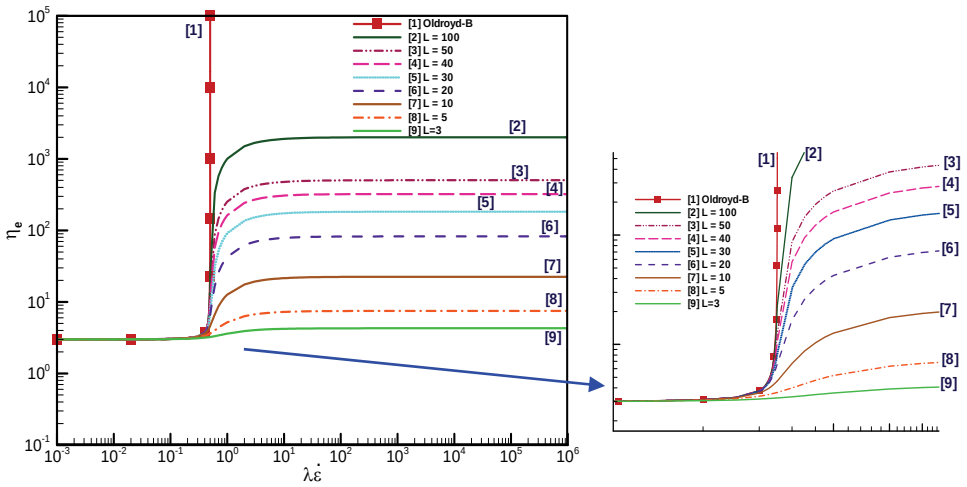

Figure 4. Extensional viscosity data for model E (FENE-CR), increasing L.

These are some of the reasons why we thought that a numerical study of model E in contraction/expansion flow would be useful.

4. NUMERICAL BACKGROUND

4.1. Hybrid Finite Element/Finite Volume Scheme

The hybrid finite element/volume scheme employed is a semi-implicit, time-splitting, fractional staged formulation, which draws upon finite element discretization for velocity-pressure approximation and finite volume for stress (see Webster *et al*. [24], Matallah *et al*. [25]). Under the *fe* construction, a two-step Lax-Wendroff scheme is employed, a Taylor-Galerkin variant (Donea [26], Zienkiewicz [27]), alongside an incremental pressure-correction procedure (with $0\le\theta_1\le1$). For solenoidal conditions and with a forward time increment factor $\theta_2=0.5$, this pressure-correction scheme attracts second-order temporal accuracy, with its incremental form ($\theta_1>0$) proving superior in uniform temporal error bound attainment over its non-incremental counterpart ($\theta_1=0$). The three-stage structure can be conveniently expressed (Wapperom and Webster [28]) in semi-discrete representation on the single time step $[t^n; t^{n+1}]$, with starting values $[u^n; \tau^n, p^n, p^{n-1}]$, via:

$$\textit{Stage 1a:}\quad \frac{2\,\mathrm{Re}}{\Delta t}\left(u^{n+\frac{1}{2}}-u^{n}\right)=\left[\nabla\tau\right]^{n}+\nabla\cdot\left(2\beta\frac{d^{n+\frac{1}{2}}+d^{n}}{2}\right)-\nabla\left(p^{n}+\theta_1(p^{n}-p^{n-1})\right)+F_G^{n}$$

$$\frac{2We}{\Delta t}\left(\tau^{n+\frac{1}{2}}-\tau^{n}\right)=\left(fI-f\tau-\lambda_1\left(u\cdot\nabla\tau-L\cdot\tau+\tau\cdot L^{T}\right)\right)^{n}$$

$$\textit{Stage 1b:}\quad \frac{\mathrm{Re}}{\Delta t}\left(u^{*}-u^{n}\right)=\left[\nabla\tau\right]^{n+(1/2)}+\nabla\cdot\left(2\beta\frac{d^{*}+d^{n}}{2}\right)-\nabla\left(p^{n}+\theta_1(p^{n}-p^{n-1})\right)+F_G^{n+(1/2)}$$

$$\frac{We}{\Delta t}\left(\tau^{n+1}-\tau^{n}\right)=\left(fI-f\tau-\lambda_1\left(u\cdot\nabla\tau-L\cdot\tau+\tau\cdot L^{T}\right)\right)^{n+\frac{1}{2}}$$

$$\textit{Stage 2:}\quad \nabla^2\left(p^{n+1}-p^{n}\right)=\frac{\mathrm{Re}}{\theta_2\Delta t}\nabla\cdot\left(u^{*}\right)$$

$$\textit{Stage 3:}\quad \frac{2\,\mathrm{Re}}{\Delta t}\left(u^{n+1}-u^{*}\right)=-\theta_2\nabla\left(p^{n+1}-p^{n}\right)\qquad(25)$$

Here, $L=\nabla\mathbf{u}$, and the Reynolds number is defined according to convention as $\mathrm{Re}=\rho U\ell/\eta_0$, where ρ is the fluid density and U, ℓ are characteristic velocity and length scale of the flow, and η_0 is the total viscosity.

Galerkin discretization may be applied to the embedded Stokesian system components; the momentum equation at Stage 1, the pressure-correction equation at Stage 2 and the incompressibility satisfaction constraint at Stage 3 (to ensure higher order precision). An

SciRes Copyright © 2010

element-y-element Jacobi solution procedure is utilized at Stage 1 (momentum) and Stage 3 for the resulting Galerkin-type Mass matrix-vector equations. This is an efficient and accuracy technique, requiring only a handful of iterations and a mixture of exact and numerical integration rules. This offers a space-time trade-off, so that huge problems may be accommodated (3D, multiple relaxation times, multi-scale). At Stage 2, a direct Choleski decomposition is required, necessitating only a single matrix reduction phase necessary at the outset. Then, semi-implicitness is introduced at Stages 1a,b on pressure and diffusive terms to enhance stability in the strongly viscous regime. Note that, pressure temporal increments invoke multi-step reference across three successive time levels [t^{n-1}, t^n, t^{n+1}].

4.2. Finite Volume Fluctuation Distribution Scheme

The theory may be exposed by first expressing the extra-stress equation in non-conservative form, with flux ($\boldsymbol{R} = \mathbf{u}.\nabla\boldsymbol{\tau}$,) and absorbing remaining terms under the source ($\boldsymbol{Q}$), one may obtain:

$$\frac{\partial \boldsymbol{\tau}}{\partial t} + \boldsymbol{R} = \boldsymbol{Q} \tag{26}$$

Then, cell-vertex *fv*-schemes are applied to this equation utilizing fluctuation distribution as the upwinding technique, to distribute control volume residuals and furnish nodal solution updates (Wapperom and Webster [29]). We consider each scalar stress component, τ, acting on an arbitrary volume $\Omega = \sum_l \Omega_l$, whose variation is controlled through corresponding components of fluctuation of the flux (R) and the source term ($\boldsymbol{Q}$),

$$\frac{\partial}{\partial t}\int_{\Omega_l} \tau d\Omega = -\int_{\Omega_l} R d\Omega + \int_{\Omega_l} Q d\Omega \tag{27}$$

Flux and source variations are evaluated over each finite volume triangle (Ω_l), and are subsequently allocated by the chosen cell-vertex distribution scheme to its three vertices. In this manner, by summing all contributions from its control volume Ω_l, the nodal update is obtained composed of all *fv*-triangles surrounding node (l). The flux and source residuals may be evaluated over two separate control volumes associated with a given node (l) within the *fv*-cell T. This generates a contribution governed over the *fv*-triangle T, (R_T, Q_T), and that subtended over the median-dual-cell zone, (R_{mdc}, Q_{mdc}). For reasons of temporal accuracy, this procedure demands appropriate area-weighting to maintain consistency, with extension to time-terms likewise. A generalized *fv*-nodal update equation may be expressed per stress component, by separate treatment of individual time derivative, flux and source terms, and integrating over associated control volumes, yielding,

$$\left[\sum_{\forall T_l} \delta_T \alpha_l^T \Omega_T + \sum_{\forall MDC_l} (1-\delta_T)\hat{\Omega}_l^T\right]\frac{\Delta\tau_l^{n+1}}{\Delta t} = \sum_{\forall T_l} \delta_T \alpha_l^T b^T + \sum_{\forall MDC_l} (1-\delta_T) b_l^{MDC} \tag{28}$$

where $b^T = (-R_T - Q_T)$, $b_l^{MDC} = \left(-R_{MDC} + Q_{MDC}\right)^l$, Ω_T is the area of the *fv*-triangle T, and $\hat{\Omega}_l^T$ is the area of its median-dual-cell (*MDC*). The weighting parameter, $0 \le \delta_T \le 1$, directs the balance taken between the contributions from the median-dual-cell and the *fv*-triangle T. The discrete stencil of **Eq.27** identifies fluctuation distribution and median dual cell contributions, area weighting and upwinding factors (α_l^T - scheme dependent). The interconnectivity of the *fv*-triangular cells (T_i) surrounding the sample node (l), the blue-shaded zone of *mdc*, the parent triangular *fe*-cell, and the fluctuation distribution (*fv*-upwinding) parameters (α_i^T), for *i=l, j, k* on each *fv*-cell, are all features illustrated in **Figure 5**.

5. NUMERICAL PREDICTIONS

As we have indicated, the benchmark problem we wish to address is that of flow within a 4:1:4 axisymmetric rounded-corner contractions (**Figure 1**). In this study, creeping flow is assumed (Re≈10^{-2}). We concentrate again on the *epd* defined in **Eq.7**, rather than the Couette correction, and we restrict attention to β=0.9 and 1/9.

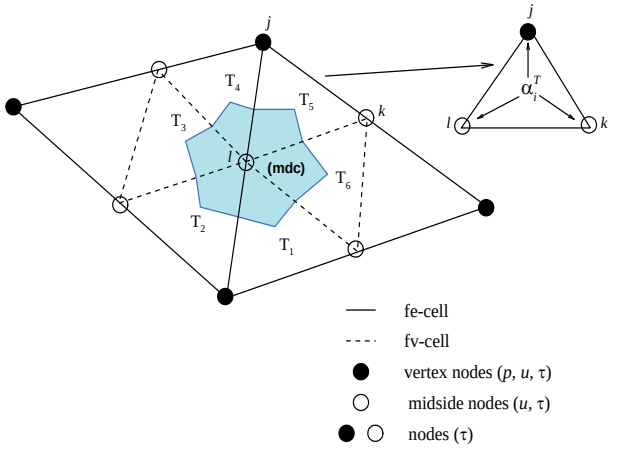

Figure 5. Spatial discretisation: fe-cell with four fv-subcells and fv control volume for node l with median-dual-cell (shaded).

SciRes Copyright © 2010

5.1. Effect of Normal Stress (N_1) and Extensional Viscosity (η_e) on *epd* Comparison of Results for Models D (Oldroyd B) and E (FENE-CR)

The important new simulation results are contained in **Figures 6-10**, in which we see *epd* data for both the Oldroyd B model and variants of the FENE-CR model.

It is clear that our simulations for the Oldroyd B model reach a limit at De_{crit}=5.1 (see **Figure 8**), evidently due to unbounded η_e and over-strong N_1; and we have been unable to reach higher Deborah numbers. Hence, unfortunately, for β=0.9, we have been unable to break through the *epd*=1.0 barrier (*epd*=0.999792 at *De* =5.1), whilst for β=0.95, a positive value of *epd* is obtained. We have previously confirmed such results through spatial resolution with three different meshes; see Aguayo *et al*. [10].

This state of affairs may be contrasted with that for the FENE-CR model, which is bounded in extension and has a weakened N_1 behavior (see **Figure 3**). As above, we can anticipate a lowering of *epd* values due to η_e damping and an elevation due to N_1 damping. There must clearly be a trade-off between these two factors; but at least we have been able to reach relatively high values of *De* in the FENE-CR simulations. Over the range of *De* values covered in **Figure 6**, we see an increase in *epd* values for L=5 of approximately 15% at *De*=10, and in the extended range covered in **Figure 7** this rises to approximately 28%. Here, in the several decades beyond *De*=10, η_e is noted to approach its limiting upper plateau, so that continued further increase in *epd* can only be attributed to continual weakening of N_1 from its quadratic form. So, from a qualitative standpoint, much progress has been made, although it must be admitted that we are still some way from the extravagant increases in *epd* found in some of the experiments on Boger fluids.

In Aguayo *et al*. [10] and for steady flow, it was shown that *epd* in these 4:1:4 flows can only be influenced by shear and extensional contributions within the geometry constriction region excluding the shear upstream-downstream zones. Below we note just how important the shear component (N_1) can be in this mixed flow region (best interpreted in a Lagrangian sense). One can attempt to segregate the various competing factors through comparison with pairings of L-parameter *epd* data. For example, comparing data in **Figure 6** for lower values of L={3,5} and the deformation rate range 0≤*De*≤3.33, one can observe the elevating effect from L=5 to L=3 on *epd* of gradually weakening N_1 (which is the dominant influence in this range). This outcome cannot be attributed to the declining influence of η_e (see **Figure 4**), as if anything, this would have a counter-effect on *epd*. Subsequently, in the range *De*>3.33, extensional viscosity effects begin to dominate, as observed in the consistently larger *epd*-values for L=5; leading to upper limits at *De*=10 (above the Newtonian reference level) some three times larger with L=5 (*epd*=1.15) than for L=3 (*epd*=1.05). Note, that the transition zone-point (*De*≈ 3.33) is highlighted in **Figure 6**, where N_1 and η_e influential dominance switches over.

The same argument for domination of N_1-weakening/ η_e-strengthening holds true for the L={3,10} and {5,10} data; with shifts in the transition point to *De*≈7 for L={3,10} and to *De*≈8.5 for L={5,10}. For L=10 data and in contrast to Oldroyd-B *epd*-data in **Figure 8**, weakening N_1 behavior for the FENE-CR model elevates *epd* up to the intersection/transition point (*De*≈2.5). Over 2.5≤*De*≤5, the stronger η_e of the Oldroyd model increasing prevails, so that larger η_e gives larger *epd*, a trend anticipated to continue as *De* rises (*nb*. De_{crit}=5.1, Oldroyd-B). In contrast, the F extension/weakening of N_1) achieves a De_{crit}=9 at which the increase in *epd* advances to around 18%.

Considering larger values of the extensibility parameter (L≥40, with larger η_e plateaux) in **Figure 9**, all FENE-CR *epd* results are now qualitatively similar to those-for the Oldroyd-B model, with transition point (gov-

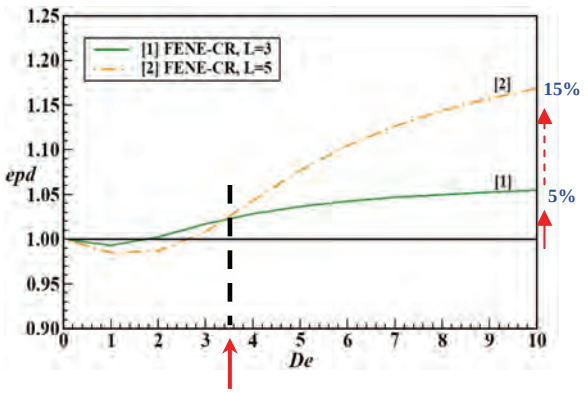

Figure 6. Normalised pressure-drop (*epd*) vs $De(=\lambda\dot{\gamma}_{avg})$ for model E (FENE-CR, L=3, 5), β=0.9.

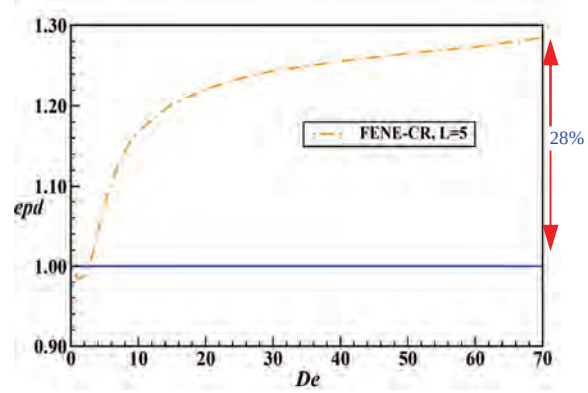

Figure 7. Normalised pressure-drop (*epd*) vs $De(=\lambda\dot{\gamma}_{avg})$ for model E (FENE-CR, L=5), β=0.9.

SciRes Copyright © 2010

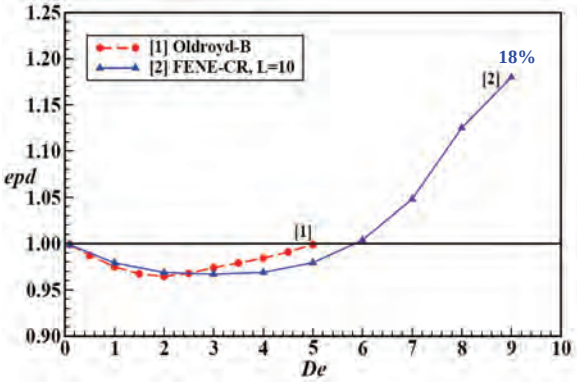

Figure 8. Normalised pressure-drop (*epd*) vs $De(=\lambda\dot{\gamma}_{avg})$ for model E (FENE-CR, L=10) and model D (Oldroyd-B), β=0.9.

erning dominance) shifting to the lower value $De\approx 2$.

Here, relative to the Oldroyd-B *epd*-data, there is slight elevation of *epd* for $De\leq 2$ (N_1-dominating) and slight suppression of *epd* for De>2 (η_e-dominating).

For completeness, we include simulations for a (lower) value of solvent fraction β, namely β=1/9. In the early days of Computational Rheology, this value was favored, the reasoning being associated with the realization that, for some models such as the so-called Corotational Oldroyd Model, higher values of β would lead to a non-monotonic shear-stress/shear-rate response. It must be emphasized that such a restriction is *not* relevant to the Oldroyd B model and is certainly not appropriate for Boger fluids, where we have argued that β=0.9 (and higher) is more realistic. However, to enable a comparison to be made with some earlier studies, we include in **Figure 10** simulations for β=1/9 (low solvent fraction, high polymeric contribution).

These simulations are in general agreement with those of Szabo *et al*. [15], who also noted *epd* enhancement for L=5, β=1/9, accompanied with the explanation that…"a particular value of L=5 needed less stretch to achieve full extension" and a sink flow (pure extension) analysis to identify pressure drop upturn and vortex behavior. We observe, by inspection across L-values at fixed *De* for β=1/9, that it is the dominating influence of N_1 that is clearly apparent with no transition points to η_e domination. Interpreted at any particular *De*, as L rises, N_1 increases in strength and *epd* declines monotonically. Under such conditions, η_e-plateaux also rise and so would be anticipated to only contribute to *epd*-enhancement. Hence, the suppressive influence of N_1-rise must counter this to generate decline in *epd*.

Viewed at each L-value and rising *De*, earlier arguments reapply governing the competing influences upon *epd*. This yields a rise of around 13% in *epd* for L=3 at *De*=4. In contrast, the position is adjusted accordingly for L=5 and L=10 data, with gradual strengthening of N_1-influence. Hence, for L=10, one detects a local minimum at *De*=3, beyond which there is an 'upturn'.

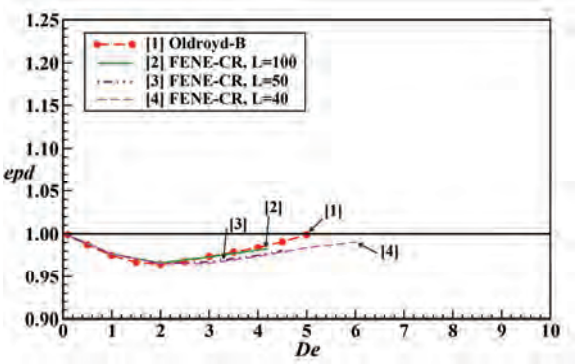

Figure 9. Normalized pressure-drop (*epd*) vs *De* $(=\lambda\dot{\gamma}_{avg})$ for model E (FENE-CR, L=40,50,100) and model D (Oldroyd-B), β=0.9.

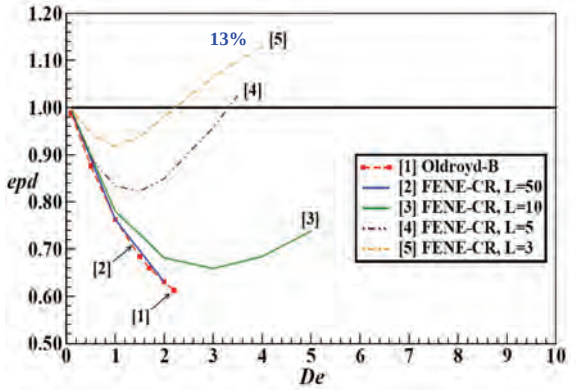

Figure. 10. Normalised pressure-drop (*epd*) vs $De(=\lambda\dot{\gamma}_{avg})$ for model E (FENE-CR, L=3-50) and model D (Oldroyd-B), β=1/9.

However, the overall lowering of *epd*-level at L=10 is such that there is insufficient recovery for *De*>3 to cross the Newtonian reference line, as occurs with L=3 and L=5 *epd*-data.

6. CONCLUSIONS

The current work has covered the numerical prediction of the excess pressure drop (*epd*) for the flow of FENE-CR fluids through a 4:1:4 contraction/expansion geometry with rounded corners. A detailed study of *epd* and associated parameters has revealed some interesting and provocative results.

Unlike the inadequacies of the Oldroyd B model in observing the experimentally observed increases in *epd*, various forms of the FENE CR model, possessing first normal stress differences weaker than the strong quadratic form of the Oldroyd B model, are capable of predicting enhanced *epd*.

We are encouraged by the fact that we have been able to reach epd elevations of nearly 30%, and this is clearly a step in the right direction. However, this is still some way short of some of the large epd-levels found experi-

SciRes Copyright © 2010

mentally for Boger fluids. In addition, we are a little concerned that the various parameters in the FENE-CR model, such as L, are not physically representative at the molecular level, (something which is of course well documented in the literature), and, more importantly, that they have needed to be chosen so precisely in the present work to obtain the desired effect. This suggests some form of dynamic and locally rate-responsive scale would be more appropriate, as commended through the FENE-Adaptive- Length-Scale (ALS) model (Ghosh *et al*. [30]).

So, there are still questions to be answered, but at least some progress has been (and is being) made! In the future, this work will be extended to analyze the additional adjustment when shear-thinning properties are introduced; and also alternative flow scenarios where energy related issues are pertinent, such as drag characteristics in flow past a sphere.

REFERENCES

[1] Debbaut, B. and Crochet, M.J. (1988) Extensional effects in complex flows. *J Non-Newton Fluid Mech*, **30,** 169-184.

[2] Debbaut, B., Crochet, M.J., Barnes, H.A. and Walters, K. (1988) Extensional effects in inelastic liquids. *Xth Inter. Congress on Rheology*, Sydney, 291-293.

[3] Binding, D.M. (1991) Further considerations of axisymmetric contraction flows. *J Non-Newton Fluid Mech*, **41,** 27-42.

[4] Nigen, S. and Walters, K. (2002) Viscoelastic contraction flows: comparison of axisymmetric and planar configurations. *J Non-Newton Fluid Mech* , **102,** 343-359.

[5] Rothstein, J.P. and McKinley, G.H. (2001) The axisymmetric contraction-expansion: The role of extensional rheology on vortex growth dynamics and the enhanced pressure drop. *J Non-Newton Fluid Mech*, **98,** 33-63.

[6] Phillips, T.N. and Williams, A.J. (2002) Comparison of creeping and inertial flow of an Oldroyd B fluid through planar and axisymmetric contractions. *J Non-Newton Fluid Mech*, **108,** 25-47.

[7] Aboubacar, M., Matallah, H., Tamaddon-Jahromi, H.R. and Webster, M.F. (2002) Numerical prediction of extensional flows in contraction geometries: Hybrid finite volume/element method. *J Non-Newton Fluid Mech*, **104,** 125-164.

[8] Walters, K. and Webster, M.F. (2003) The distinctive CFD challenges of computational rheology. *Inter J for Numer Meth in Fluids*, **43,** 577-596.

[9] Alves, M.A., Oliveira, P.J. and Pinho, F.T. (2004) On the effect of contraction ratio in viscoelastic flow through abrupt contractions. *J Non-Newton Fluid Mech*, **122,** 117-130.

[10] Aguayo, J.P., Tamaddon-Jahromi, H.R. and Webster, M.F. (2008) Excess pressure-drop estimation in contraction flows for strain-hardening fluids. *J Non-Newton Fluid Mech*, **153,** 186-205.

[11] Walters, K., Webster, M.F. and Tamaddon-Jahromi, H.R. (2009a) The numerical simulation of some contraction flows of highly elastic liquids and their impact on the relevance of the Couette correction in extensional rheology. *Chem Eng Sci*, **64,** 4632-4639.

[12] Walters, K., Webster, M.F. and Tamaddon-Jahromi, H.R. (2009b) The White-Metzner model then and now. *Proceedings of the 25th Annual Meeting of the PPS meeting*, Goa, India, **02,** 1-14.

[13] Walters, K., Tamaddon-Jahromi, H.R., Webster, M.F., Tomé, M.F. and McKee, S. (2010) The competing roles of extensional viscosity and normal stress differences in complex flows of elastic liquids. *Korean-Australian Journal (to be published)*, 2010.

[14] White, J.L. and Metzner, A.B. (1963) Development of constitutive equations for polymeric melts and solutions. *J Appl Polym Sci*, **7,** 1867-1889.

[15] Szabo, P., Rallison, J.M. and Hinch, E.J. (1997) Start-up of flow of a FENE-fluid through 4:1:4 constrictions in a tube. *J Non-Newton Fluid Mech*, **72,** 73-86.

[16] Chilcott, M.D. and Rallison, J.M. (1988) Creeping flow of dilute polymer solutions past cylinders and spheres. *J Non-Newton Fluid Mech*, **29,** 381-432.

[17] Barnes, H.A., Hutton, J.F. and Walters, K. (1989) An introduction to rheology. *Elsevier*, Amsterdam.

[18] Jackson, K.P., Walters, K. and Williams, R.W. (1984) A rheometrical study of Boger fluids. *J Non-Newton Fluid Mech*, **14,** 173-188.

[19] Tanner, R.I. and Walters, K. (1998) Rheology: An historical perspective, *Elsevier Science & Technology*, Netherlands.

[20] Binding, D.M., Phillips, P.M. and Phillips, T.N. (2006) Contraction/expansion flows: The pressure drop and related issues. *J Non-Newton Fluid Mech*, **137,** 31-38.

[21] Walters, K., Webster, M.F. and Tamaddon-Jahromi, H.R. (2008) Experimental and computational aspects of some contraction flows of highly elastic liquids and their impact on the relevance of the Couette correction in extensional rheology. *Proc. 2nd Southern African Conference on Rheology (SASOR 2)*, 1-6.

[22] Oldroyd, J. G. (1950) On the formulation of rheological equations of state. *Proc. Roy .Soc*., **A200,** 523-541.

[23] Boger, D.V. and Walters, K. (1993) *Rheological phenomena in focus*, Elsevier Science Publishers.

[24] Webster, M.F., Tamaddon-Jahromi, H.R. and Aboubacar, M. (2005) Time-dependent algorithms for viscoelastic flow: Finite element/volume schemes. *Numer Meth Par Diff Equ*, **21,** 272-296.

[25] Matallah, H., Townsend, P. and Webster, M.F. (1998) Recovery and stress-splitting schemes for viscoelastic flows. *J Non-Newton Fluid Mech*, **75,** 139-166.

[26] Donea, J. (1984) A Taylor-Galerking method for convective transport problems. *Int J Numer Methods Eng*, **20,** 101-119.

[27] Zienkiewicz, O.C., Morgan, K, Peraire, J., Vandati, M. and Löhner R. (1985) Finite elements for compressible gas flow and similar systems. *Seventh International Conference on Computational Methods of Applied Science and Engineering*.

[28] Wapperom, P. and Webster, M.F. (1999) Simulation for viscoelastic flow by a finite volume/element method. *Comput Meth Appl Mech Eng*, **180,** 281-304.

[29] Wapperom, P. and Webster, M.F. (1998) A second-order hybrid finite-element/volume method for viscoelastic flows. *J Non-Newton Fluid Mech*, **79,** 405-431.

[30] Ghosh, I., Lak, Joo Y., McKinley, G.H., Brown, R.A. and Armstrong, R.C. (2002) A new model for dilute polymer solutions in flows. *J Rheol*, **46(5),** 1057-1089.

SciRes Copyright © 2010

Vol.2, No.1, 12-17 (2010)
doi:10.4236/ns.2010.21002

Synthesis of nano crystalline spatulae of lead zirconate titanate ($PbZr_{0.52}Ti_{0.48}O_3$)

S. S. Bhatt*, S. C. Chaudhry, Neeraj Sharma, Sonia Gupta

Department of Chemistry, Himachal Pradesh University, Shimla, India; ssbhatt2k@yahoo.com

Received 15 October 2009; revised 29 October 2009; accepted 2 November 2009.

ABSTRACT

A simple and effective method for the synthesis of nano-crystalline PZT spatulae has been reported near MPB via a new *Solution-Ignition Synthesis* route and has been characterized by FT-IR, XRD, TG/DTG/DTA and SEM techniques. X-ray line broadening and Scherrer formula show crystallite size to be~20 nm. Densities of nano-crystalline spatulae of PZT in pellet form made by using 2% PVA and without PVA have been found to be 5.35 and 7.51 gm/cm^3 respectively compared to the theoretical value of 7.78 gm/cm^3. Dielectric constants of 83 and 227 of these spatulae with dielectric loss 0.118 and 0.0609 at 1 MHz and a high resistivity value of 3.043 * 10^7 Ω cm for PZT pellets made without PVA suggest these nano-crystalline PZT spatulae to be the potential candidates for high frequency applications.

Keywords: Nanostructures; Chemical Synthesis; Infrared Spectroscopy; X-ray Diffraction; Dielectric Properties

1. INTRODUCTION

In advanced ceramics technology, the production of good quality powders using different synthetic routes has always been an essential requirement to obtain materials with desired properties, purity and stoichiometry. It is because of an ever-increasing pace of development of various technological innovations to sustain competitive advantage, that various synthetic methods such as self-propagating high temperature synthesis (SHS) [1], sol-gel [2], hydrothermal [3-6], solution combustion synthesis (SCS) [7] and wet grinding solid state thermal reaction (a combination of SHS and SCS methods) [8] have been reported in literature for the preparation of inorganic oxide materials. Metal oxide of composition $PbZr_{0.52}Ti_{0.48}O_3$, synthesized by sintering process between 1200°C and 1300°C is known to be quite important for technological applications due to its ferroelectric and piezoelectric properties near morphotropic phase boundary (MPB) [9,10]. For multilayer components and thick film devices, it is desirable to bring down its sintering temperature, thereby reducing energy consumption and PbO evaporation.

In view of these interesting reports, we have therefore made an attempt to synthesize nano-crystalline spatulae of lead zirconate titanate, $PbZr_{0.52}Ti_{0.48}O_3$, near morphotropic phase boundary (MPB) by a novel method, solution ignition synthesis (SIS). This method is better than other methods in a way that by igniting the solution drop-wise, the surface area is increased and heat produced during ignition is sufficient to rise the internal temperature per ignited drop, thereby reducing the overall high temperature sintering requirement for the ceramics.

2. MATERIALS AND METHODS

2.1. Chemicals

The starting materials used for the preparation of lead zirconate titanate powder i.e. lead acetate $Pb(CH_3COO)_2.3H_2O$, zirconyl nitrate $ZrO(NO_3)_2\ H_2O$ and titanium tetra isopropoxide Ti [$(OPr^i_4]$ were of E Merck and used as such without further purification.

2.2. Preparation of 'As-Ignited Powder'

A solution of lead acetate $Pb(CH_3COO)_2.\ 3H_2O$ (5 gm, 0.0131 mol) in acetic anhydride was added drop-wise to a mixture solution of $ZrO(NO_3)_2.\ H_2O$, (1.5848gm,. 00685 mol) and titanium tetra isopropoxide $Ti(OPr^i)_4$, (1.7984 gm, 0.006326 mol) dissolved in the same solvent, with continuous stirring and a temperature of 60°C during the course of addition was maintained. The resulting clear mixture solution was then ignited by drop-wise addition over aperiod of 4-5 hours into preheated silica crucible kept at 200°C. Yellow colored solid mass formed during the course of addition was scratched from the walls of silica crucible after cooling it to room temperature. It was finally grinded to a fine powder and labeled as "as-ignited powder". The post annealing of the

SciRes Copyright © 2010

"as-ignited powder" was done in an electric furnace at 600°C and 700°C for four hours in each case.

2.3. Instrumentation

FTIR spectra were scanned in KBr pellets using single grating Nicolet 5700 series FTIR spectrophotometer in the range of 4000-200 cm^{-1}. Thermal analysis curves (TGA/DTG/DTA) of the synthesized powders were recorded on a double pan SHIMADZU DTG-60H (simultaneous TG/DTA module) thermal analyzer. The thermocouple used was Pt/Pt-Rh (10%) with a temperature range from ambient to 1300°C. The thermal investigations were carried out by heating the sample in a Pt crucible in nitrogen atmosphere and using α-Al_2O_3 as reference. A heating rate of 20°C min^{-1} was employed. The instrument calibration was checked periodically with a sample of $CuSO_4.5H_2O$. Powder X-Ray Diffraction patterns were recorded on PANalytical XPERT-PRO diffractometer system using a typical wavelength of 1.54060 A° (Cu-Kα radiation). The diffraction angle 2θ was varied from 10-70°. The morphology, exact size and shape of the lead zirconate titanate (PZT) particles were determined by recording FESEM of PZT powder annealed at 700°C on Hitachi S-4700 model.

For electrical measurements, two types of pellets, one by using 2% PVA as binder and other without PVA, were made from nano-crystalline PZT spatulae annealed at 700°C. Pelletization was done by applying 15 tons of pressure on nano PZT powder put into a circular dye, from a hydraulic press for 5 minutes and then sintered at 700°C. Both the sides of the sintered pellets were cleaned, smoothened with a very fine sand paper and electroded by applying silver paste. Current Voltage (I-V) measurements were made by using two probe method on Kaithley Source Meter (Model 2611), while dielectric studies were done by measuring capacitance of the sample with metal-insulator-metal (MIM), Agilent 4285A, 75 KHz to 3 MHz precision LCR meter.

3. RESULTS AND DISCUSSION

The synthesis of nano-crystalline PZT powder of composition $Pb(Zr_{0.52}Ti_{0.48})O_3$ near MPB by Solution-Ignition Synthesis has been shown in **Figure 1**.

3.1. FTIR Studies

A perusal of the FTIR spectra of as-ignited PZT powder (**Figure 2a**) shows no absorption bands at 2912cm^{-1}, 1652cm^{-1} and 1560 cm^{-1} attributed to ν_{C-H} and $\nu_{C=O}$ modes of acetate group indicating complete ignition of organic material used for the synthesis of samples. The absorption bands occurring at 1428 cm^{-1} and 1110 cm^{-1}, may be ascribed to ν_{C-O} modes of the trapped atmospheric carbon dioxide in the PZT material [11]. Interestingly, the intensity of these two bands decreases significantly when annealed at 600°C (**Figure 2b**) and disappears completely at 700°C (**Figure 2c**). Another distinct absorption band observed at 563 cm^{-1} has been assigned to ν_{M-O} mode which is characteristic of the formation of ABO_3 type of perovskite structure of PZT powder [12]. The effect of annealing at 600°C and 700°C on the characteristic bands is apparent from the shift of ν_{M-O} band from 563cm^{-1} to higher wave numbers, 590cm^{-1} and 592cm^{-1} respectively, presumably due to increased number of M-O bonds in the perovskite phase of PZT material. In addition, the band at 592cm^{-1} in the sample annealed at 700°C has been found to be more intense than the band at 590cm^{-1} annealed at 600°C, confirming thereby the formation of more of perovskite phase at higher temperature.

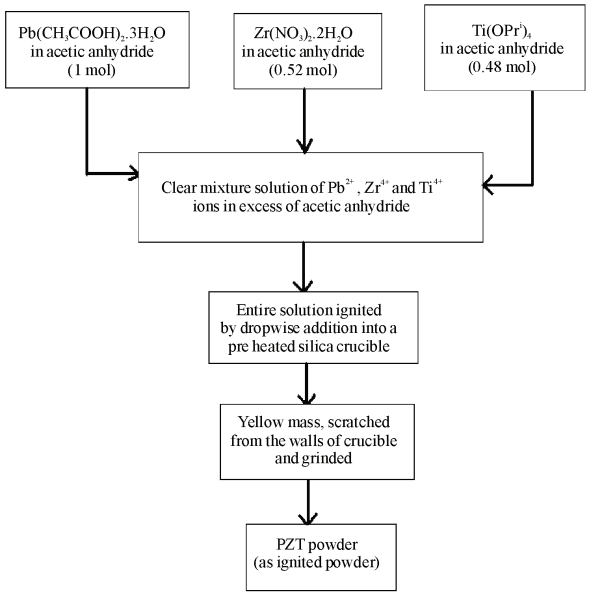

Figure 1. Scheme for the preparation of lead zirconate titanate powder by solution-ignition synthesis (SIS).

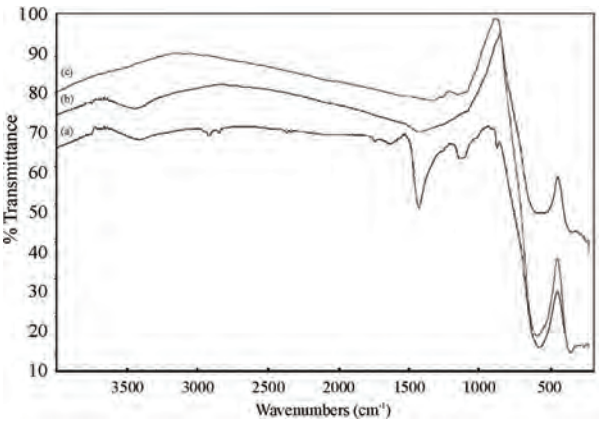

Figure 2. FTIR spectra of a) as-ignited PZT powder; b) powder annealed at 600°C; c) powder annealed at 700°C.

SciRes Copyright © 2010

3.2. Thermal Analysis

Thermo analytical curves (TG/DTG/DTA) for as-ignited PZT powder (**Figure 3** blue in color) show only one step decomposition in the range 275.93°C to 331.77°C with a weight loss of only 1.005% as is also substantiated by only one peak in DTG at 311.52°C and an endothermic peak at 307.51°C in DTA curve indicated the escape of carbon dioxide gas trapped in as-ignited PZT powder. The TG/DTA curves (**Figure 3** red in color) of as-ignited powder annealed at 600°C, however, has shown neither any weight loss in TG nor any peak in DTA curve indicating the complete removal of carbon dioxide gas trapped in the lattice of nano-crystalline PZT powder.

3.3. XRD Studies

Powder XRD pattern of as-ignited PZT powder (**Figure 4a**) shows broad and an ordered arrangement of peaks, indicating the formation of nano-crystalline lead zirconate titanate, presumably resulting from the internal heat produced during drop-wise ignition of the reaction mixture solution. Further, the pyrochlore phase which was present initially at 28.5° 2θ with relative intensity of 100% (657 counts) in as-ignited PZT powder (**Figure 4a**) gets significantly reduced at 600°C and completely transformed into perovskite phase at 31.0538° 2θ value after annealing at 700°C (**Figures 4b** and **4c**). Apparently, therefore, the results of the PXRD patterns of as-ignited PZT powder coupled with FTIR and thermo analytical curves suggest that the solution ignition synthesis (SIS) is a novel method of synthesis of nanocrystalline PZT spatulae.

Indexing of the XRD patterns of nano-crystalline PZT powder annealed at 700°C (**Figure 4c**) has been done by matching them with the patterns of known PZT powder of composition $Pb(Zr_{0.52}Ti_{.48})O_3$ [13,14]. Lattice parameters of the sample annealed at 700°C (c=4.32159A° and a=b= 4.06907A°) obtained from (001) and (100) reflections at 20.5522° and 21.8429° 2θ values respectively in XRD pattern with slight lattice distortion (c/a) values to be 1.0620 have been found to be very close to that of 1.066 of pure tetragonal phase [15]. Further, the sharpness of the diffraction peaks in the XRD pattern (**Figure 4c**) suggests better homogeneity and crystallinity of the nano PZT spatulae. It is pertinent to mention here that with the increase in annealing temperature of as-ignited powder from 600°C and finally to 700°C, a substantial increase in the intensity (counts) of the perovskite (110) orientation has been observed thereby confirming the enhanced crystallinity.

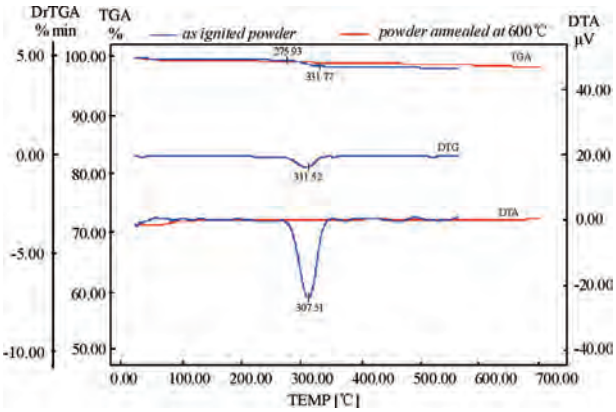

Figure 3. Thermal analysis (TGA/DTA/DTG) curves of as-ignited PZT powder (red) and PZT powder annealed at 600°C (blue).

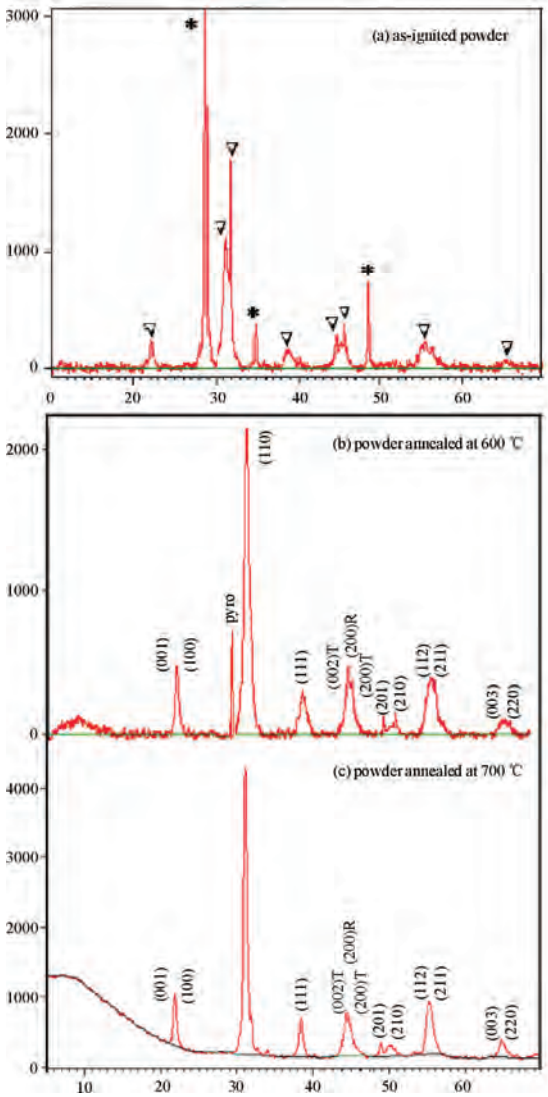

Figure 4. Powder X-ray diffraction patterns of: a) as-ignited PZT Powder; b) PZT powder annealed at 600°C; and c) at 700°C (∇-*Perovskite phase* and ⁎-*Pyrochlore phase*).

The relative amounts of perovskite and pyrochlore phases (**Table 1**) have been determined from the relative intensity of XRD peaks by using following equation [16]:

$$\% \text{ perovskite phase} = \frac{I_{(110)}}{I_{(110)} + I_{(pyro)}}$$

where $I_{(110)}$-relative intensity of the peak due to (110) orientation and $I_{(pyro)}$-relative intensity of pyrochlore phase. A perusal of the results in **Table 1** indicates that amount of pyrochlore phase decreases while the perovskite phase increases with the increase in annealing temperature.

Apart from the tetragonal phase depicted from the XRD pattern of the PZT powder annealed at 700°C, the relative percentage of rhombohedral and tetragonal phases has been calculated from the triplets of the type (002)T, (200)R and (200)T appearing at 44°-46° 2θ range in the XRD pattern [17] using relation:

$$P_R = \frac{I_{R(200)}}{I_{R(200)} + I_{T(200)} + I_{T(002)}}$$

where P_R represents rhombohedral phase, $I_{R(200)}$ is intensity of (200) reflection of rhombohedral phase, $I_{T(200)}$ and $I_{T(002)}$ is intensity of (200) and (002) reflections of tetragonal phase. The results show that percentage of rhombohedral and tetragonal phase in the present nano-crystalline PZT powder is 30% and 70% respectively indicating thereby that the chemical composition of synthesized nano-crystalline PZT powder lies near to Morphotropic Phase Boundary.

3.4. Crystallite Size, Shape and Density

3.4.1. Size

Broadening of the peaks observed in the XRD patterns (**Figures 4a-4c**) indicates particles in the nano range. Crystallite size of the nano-crystalline PZT powder annealed at 600°C and 700°C has been calculated by using Scherrer Equation i.e.

Table 1. % phases in the nano-crystalline PZT powder samples.

S. No.	Name of Sample	% Perovskite	% Pyrochlore
1	As-ignited powder	36.10	63.89
2	Powder annealed at 600°C	71.81	28.18
3	Powder annealed at 700°C	97.43	2.57

$$\text{Crysttalite size} = \frac{k\lambda}{\beta \cos\theta}$$

where ***k*** is the constant of proportionality (Scherrer constant) and depends on how the width line is determined and value of k is generally taken as 0.9. ***λ*** represents the wavelength of the X rays and has a value of 1.54060A°, ***θ*** is the half of the angle (2θ) of diffraction and ***β*** is the value of broadening of (110) line at Full Width Half Maximum (FWHM) of in radians and has been found to be 13.6 nm which increases to 21.4 nm respectively. Such an increase in the crystallite size with increase in annealing temperature finds support from earlier reports in literature [18,19].

3.4.2. Shape

FESEM of the nano-crystalline PZT powder annealed at 700°C (**Figure 5**) shows a mixture of both spherical particles and stacks of nano spatulae of about 204 nm in width. The spherical nature of the crystallite has been attributed to the high pressure exerted by the evolution of gases such as CO_2, N_2, O_2, etc. during the course of ignition reaction [20] while the formation of stacks of nano spatulae may be attributed to the partial melting and subsequent solidification during dropwise ignition of the PZT powder in the preheated silica crucible.

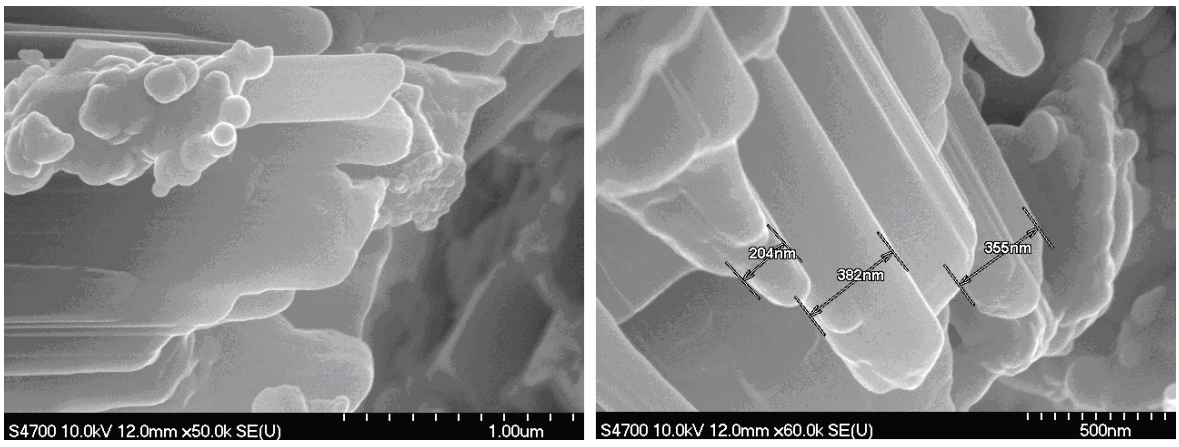

Figure 5. FESEM of nano-crystalline PZT spatulae.

SciRes Copyright © 2010

3.4.3. Densities and Porosity

Densities of pellets of nano-crystalline PZT powder (one made with 2% PVA as a binder and other without PVA each of 15 mm in diameter and 1.3 mm thickness) measured by Archimedes Principle have been found to be 5.35 and 7.51 gm/cm^3 respectively. These densities are 68.76% and 96.5% of the theoretical value (7.78 gm/cm^3). The percentage porosity of PZT pellets has been calculated from the relation:

$$\%\ porosity = (1 - \rho/\rho_0) \times 100$$

where **ρ** and **ρ$_o$** are the experimental and the theoretical densities of PZT (7.78 gm/cm^3) and have been found to be 31.24 % and 3.48 %.

3.5. Electrical Properties of Lead Zirconate Titanate of Composition Pb ($Zr_{0.52}Ti_{0.48}$)O_3

3.5.1. D. C. Resistivity

Resistivity has been obtained from current-voltage studies of the pellet prepared from nano-crystalline PZT powder annealed at 700°C by the two probe method using a Keithley Source meter (Model 2611). From a plot of Current vs Voltage (**Figure 6**) resistance 'R' has been calculated from the slope of the plot as, $slope\ (R) = I/V$ and the resistivity 'ρ' using the well known relation, $\rho\ (\text{ohm meter}) = \frac{RA}{d}$ where ***A*** represents the area of the cross section and ***d*** is the thickness of the pellet.

A high resistivity value of 3.043 * 10^7 Ω cm found in the present studies has been attributed to the stoichiometric composition, better crystal structures and improved microstructures obtained by this new solution ignition synthesis (SIS) technique. The higher value of resistivity is also of significant importance as it makes this nano-crystalline PZT spatulae suitable for high frequency application.

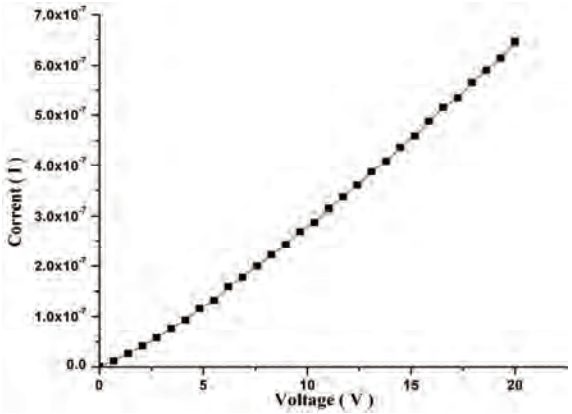

Figure 6. Current (I) vs Voltage (V) plot of nano-crystalline PZT pellet.

3.5.2. Dielectric Studies

The dielectric constant (ε) and dielectric loss (tan δ) of sintered pellets of nano-crystalline PZT spatulae (with 2% PVA and without PVA) as function of frequency at different temperatures have been studied and trends are shown as graphs in **Figures 7a** and **7b**. The values of 83 and 227 for dielectric constant and 0.118 and 0.0609 for dielectric loss have been found at a frequency of 1MHz which remains nearly same in the higher frequency range (up to 3MHz). Further, a comparison of the values of both dielectric constant (227 and 249) and dielectric loss (0.0609 and 0.042) at 298 K and 373 K respectively at constant frequency of 1MHz (**Figure 8**) shows an increase in dielectric constant with decrease in dielectric loss values. These observed low values of dielectric constants have been found to be in agreement with the fact that small grains attain low values of dielectric constant and can stabilize dielectric relaxation up to higher frequency region [21]. These studies also indicate that nano-crystalline spatulae of lead zirconate titanate, Pb ($Zr_{0.52}Ti_{0.48}$)O_3 synthesized near MPB with almost same values of dielectric constant and dielectric loss over a large range of frequencies (up to 3 MHz) may find their role as successful and stable dielectrics in the field of electronics.

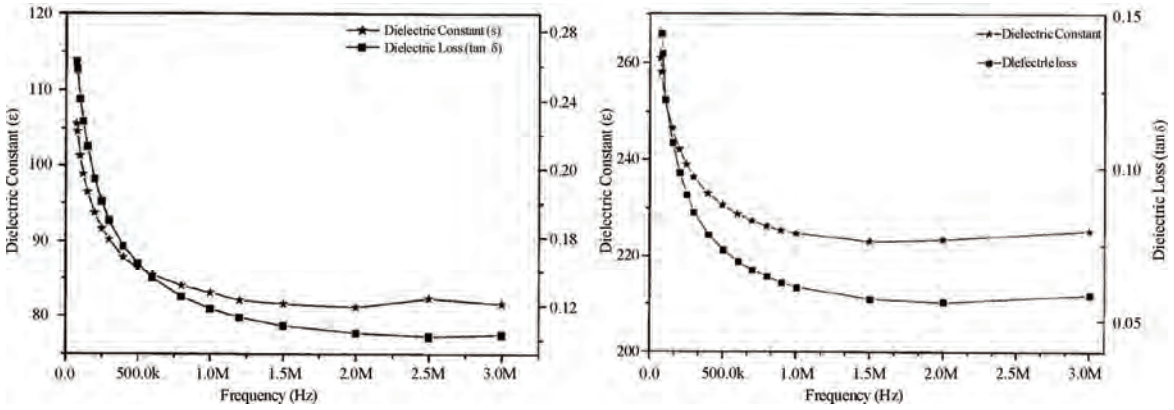

(a) (b)

Figure 7. Variation of dielectric constant and dielectric loss with frequency at room temperature for: a) PZT pellet with 2% PVA; and b) PZT pellet without PVA.

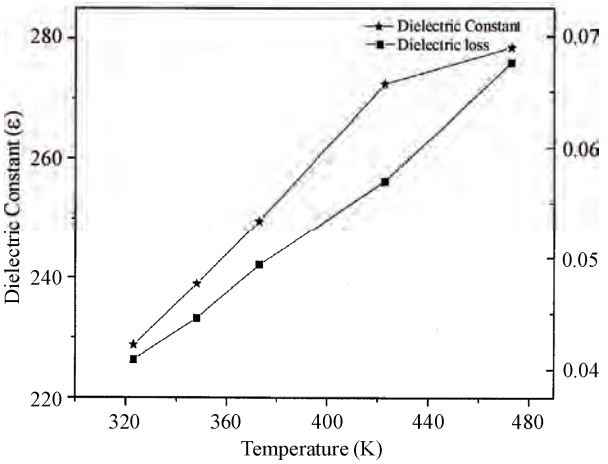

Figure 8. Variation of dielectric constant and dielectric loss with temperature at 1 MHz frequency for PZT pellet without PVA.

4. CONCLUSIONS

The present work describes a simple, effective and novel synthetic strategy namely Solution Ignition Synthesis (SIS) route for the preparation of nano-crystalline PZT, which is advantageous over other commonly employed methods. The FTIR and XRD patterns of the nano crystalline PZT spatulae confirmed their perovskite structure near MPB. The dielectric constant and high values of resistivity also suggest that they may find their role as potential materials suitable for high frequency applications and as stable dielectrics.

5. ACKNOWLEDGEMENTS

The authors wish to acknowledge University Grants Commission, New Delhi and Department of Science and Technology, GOI for providing necessary instrumentation facilities and financial support in the form of SAP and FIST programs to the Department of Chemistry.

REFERENCES

[1] Merzhanov, A.G. (1990) Twenty years of search and findings in combustion and Plasma Synthesis of high temperature materials. Edited by Munir, Z.A. and Holt, J. B., New York VCH Publ. Inc., 1-35.

[2] Livage, J. (1994) The sol-gel route to advanced materials. *Mater. Sc. Forum*, **152 & 153,** 43-54.

[3] Cheng, H.M., Ma, J.M., Zhu, B. and Cui, Y.H. (1993) Reaction mechanisms in the formation of lead zirconate titanate solid solutions under hydrothermal conditions. *J. Am. Ceram. Soc.*, **76(3),** 625-629.

[4] Traianidis, M., Courtois, C., Leriche, A. and Thierry, B. (1999) Hydrothermal synthesis of lead zirconium titanate (PZT) powders and their characteristics. *J. Europ. Ceram. Soc.*, **12(19),** 1023-1026.

[5] Kutty, T.R.N. and Balachandran, R. (1984) Direct precipitation of lead zirconate titanate by the hydrothermal method. *Mater. Res. Bull.*, **19(11),** 1479-1488.

[6] Lencka, M.M., Anderko, A. and Riman, R.E. (1995) Hydrothermal precipitation of lead zirconate titanate solid solutions: thermodynamic modeling and experimental synthesis. *J. Am. Ceram. Soc.*, **78(10),** 2609-2618.

[7] Mukasyan, A.S. and Dinka, P. (2007) Novel approach to solution-combustion synthesis of nano-materials. *Int. J. Self Propagating High Temperature Synthesis*, **16(1),** 23-35.

[8] Vijaya, M.S., Senthilkumar, R., Sridevi, K. and Subramnia, A. (2005) Preparation and piezoelectric properties of lead zirconate titanate ceramics. *Ferroelectrics*, **325,** 43-48.

[9] Jaffe, B., Roth, R.S. and Marzullo, S. (1954) Piezoelectric properties of lead zirconate lead titanate solid solution ceramics. *J. Appl. Phys.*, **25,** 809-810.

[10] Kakegawa, K., Mohri, J., Shirasaki, S. and Takahasi, K. (1982) Sluggish pansition between tetragonal and rhombohedral phases of $Pb(Zr,Ti)0_3$ prepared by application of electric field. *J. Am. Ceram. Soc.*, **65(10),** 515-519.

[11] Wang, Y. and Jorge, J. (2003) FTIR characterization of PZT nano fibers synthesized from metallo-organic compounds using electro spinning. *Mat. Res. Soc. Symp. Proc.*, **736,** D2.9.1-D2.9.6.

[12] Samuneva, B., Jambazov, D., Lepkova, D. and Dimitriev, Y. (1990) Sol-gel synthesis of $BaTiO_3$ and $Ba_{1-x-y}\,a_ySr_x\,Zr_yTi_{1-y})O_3$ perovskite powders. *Ceram. Int.*, **16,** 355-360.

[13] Sen, A., Seal, A., Das, N., Mazumdar, R. and Maiti, H.S. (2005) Technological challenges of making PZT based piezoelectric wafers. *Proc. Int. Conf. Smart Mater. Str. Sys.*, SC41-SC48.

[14] Kakegawa, K., Mohri, J., Takahashi, T., Yamamura, H. and Shirasaki, S. (1977) Compositional fluctuation and properties of $Pb(Zr,Ti)O_3$. *Powder Diffraction File PDF-2 Database Sets* 1-45, *International Centre for Diffraction Data* (*ICDD*), **24,** 769-772.

[15] Chu, S.Y. and Chen, C.H. (2001) Effect of calcium on the piezoelectric and dielectric properties of Sm-modified $PbTiO_3$ ceramics. *Sensors and Actuators*, **89 (3)**, 210-214.

[16] Lakeman, C.D.E. and Payne, D.A. (1992) Processing effects in the sol gel preparation of PZT dried gels, powders and ferroelectric thin layers. *J. Am Ceram. Soc.*, **75,** 3091.

[17] Mishra, S.K., Pandey, D. and Singh, A.P. (1996) Effect of phase coexistence at morphotropic phase boundary on the properties of Pb $(Zr_xTi_{1-x})O_3$ ceramics. *Appl. Phys. Lett.*, **69,** 1707-1709.

[18] Thamjaree, W., Nhuapeng, W. and Tunkasiri, T. (2004) Analysis of X-ray diffraction line profiles of lead zirconate titanate using fourier method. *Ferroelectric Letter*, **31,** 79-85.

[19] Verma, K.C., Kotnala, R.K., Mathpal, M.C., Thakur, N., Gautam, Prikshit and Negi, N.S. (2009) Dielectric properties of nano-crystalline $Pb_{0.8}Zr_{0.2}TiO_3$ thin films at different annealing temperature. *Materials Chemistry and Physics*, **114,** 576.

[20] Nersisyan, H.H., Lee, J.H. and Won, C.W. (2005) SHS of ceramic powders in the fusion salts of alkali metal. *J. Ceram. Process. Res.*, **6(1),** 41-47.

SciRes Copyright © 2010

Vol.2, No.1, 18-25 (2010)
doi:10.4236/ns.2010.21003

Natural Science

Hydriding and dehydriding kinetics of melt spun nanocrystalline $Mg_{20}Ni_{10-x}Cu_x$ (x = 0-4) alloys

Yang-Huan Zhang[1,2,*], Dong-Liang Zhao[1], Bao-Wei Li[2], Hui-Ping Ren[1], Shi-Hai Guo[1], Xin-Lin Wang[1]

[1]Department of Functional Material Research, Central Iron and Steel Research Institute, Beijing, China
[2]School of Material, Inner Mongolia University of Science and Technology, Baotou, China; zyh59@yahoo.com.cn

Received 22 October 2009; revised 13 November 2009; accepted 17 November 2009.

ABSTRACT

The nanocrystalline Mg_2Ni-type electrode alloys with nominal compositions of $Mg_{20}Ni_{10-x}Cu_x$ (x = 0, 1, 2, 3, 4) were synthesized by melt-spinning technique. The microstructures of the alloys were characterized by XRD, SEM and HRTEM. The hydrogen absorption and desorption kinetics of the alloys were measured using an automatically controlled Sieverts apparatus. The results show that all the as-spun alloys hold typical nanocrystalline structure. The substitution of Cu for Ni does not change the major phase Mg_2Ni but it leads to the formation of the secondary phase Mg_2Cu. The hydrogen absorption capacity of the alloys first increases and then decreases with rising Cu content, but the hydrogen desorption capacity of the alloys monotonously grows with increasing Cu content. The melt spinning significantly improves the hydrogenation and dehydrogenation capacities and kinetics of the alloys.

Keywords: Mg_2Ni-Type Alloy; Substituting Ni with Cu; Melt Spinning; Hydriding and Dehydriding Kinetics

1. INTRODUCTION

Mg and Mg-based alloys has been considered as potential materials for solid state hydrogen storage in the form of metallic hydrides such as MgH_2 and Mg_2NiH_4. The theoretical hydrogen storage capacities of MgH_2 and Mg_2NiH_4 are 7.6 wt.% and 3.6 wt.% [1,2] respectively, which is quite adequate for commercial applications as a hydrogen fuel source [3]. Unfortunately, the slow sorption/desorption kinetics and high dissociation temperature of these kinds of metal hydrides limit their practical application. Therefore, finding ways of improving the hydration kinetics of Mg-based alloys has been one of the main challenges faced by researchers in this area. Various attempts, involving mechanical alloying (MA) [4], GPa hydrogen pressure method [5], melt spinning [6], gravity casting [7], polyol reduction [8], hydriding combustion synthesis [9], surface modification [10], alloying with other elements [11,12], adding catalysts [13] etc, have been undertaken to improve the activation and hydriding property.

Gennari *et al.* [14] reported that the nanocrystalline Mg_2Ni synthesized by combined milling-annealing procedure can readily hydrogen absorption during the first cycle and show excellent absorption kinetics at 200℃. Muthukumar *et al.* [15] confirmed that a maximum hydrogen capacity of 3.67 wt.% for the Mg_2Ni alloy prepared by mechanical alloying (MA) could be achieved for an initial absorption temperature of 300 ℃ and supply pressure of 20 bar. Recham *et al.* [16] found that the hydrogen absorption property of ball-milled MgH_2 can be enhanced by adding NbF_5, and the milled MgH_2+ NbF_5 composite can desorbs 3 wt.% H_2 at 150℃. Dobrovolsky *et al.* [17] synthesized a MgH_2 (50 wt.%) + TiB_2 (50 wt.%) composite by intensive mechanical milling and found that TiB_2 addition decreases the dissociation temperature of the MgH_2 hydride by about 50℃.

Indubitably, ball-milling is a very effective method for the preparation of nanocrystalline and amorphous Mg and Mg-based alloys. Particularly, it is suitable to solubilize particular elements into MgH_2 or Mg_2NiH_4 above the thermodynamic equilibrium limit, which is helpful to destabilize MgH_2 or Mg_2NiH_4 [18]. However, the milled Mg and Mg-based alloys show very poor hydrogen absorbing and desorbing stability due to the fact that the metastable structures formed by ball milling tended to vanish during multiple hydrogen absorbing and desorbing cycles [19]. Alternatively, melt-spun technique can overcome the above mentioned shortcoming and effective avoiding the significant degradation of hydrogen absorbing and desorbing cycle properties of Mg and Mg-based [20]. Additionally, the melt-spinning technique is a very effective method to obtain a nanocrystalline structure and is very suitable for mass-production of nanocrystalline Mg-based alloys. It was also clarified that nanocrystalline alloys produced by melt-spinning could

SciRes Copyright © 2010

have excellent hydriding characteristics even at room temperature, similar to the alloys produced by the MA process. Spassov *et al.* [21] prepared Mg_2(Ni, Y) hydrogen storage alloy with exact composition $Mg_{63}Ni_{30}Y_7$ by rapid solidification, and its maximum hydrogen absorption capacity (about 3.0 wt.%) and hydrogenation kinetics of the as-spun Mg_2(Ni, Y) alloy were found to exceed those of the polycrystalline Mg_2Ni alloys prepared by conventional technology and to be comparable to the hydrogen absorption characteristics of ball-milled nanocrystalline Mg_2Ni. It was determined that the addition of third element stabilizes the nanostructure of Mg-Ni based alloy, which could be very important for practical H-storage materials.

Our previous work indicated that the substitution of Co for Ni significantly improved the hydriding and dehydriding kinetics of the Mg_2Ni-type alloys [22]. Therefore, it is very desirable to investigate the influence of substituting Ni with Cu on the hydriding and dehydriding characteristics of Mg_2Ni-type alloys prepared by melt-spinning. The objective of this work is to produce the Mg-Ni-based ternary nanocrystalline alloys by melt spinning and to examine their structures and hydriding and dehydriding kinetics.

2. EXPERIMENTAL METHODS

The alloy ingots were prepared using a vacuum induction furnace in a helium atmosphere at a pressure of 0.04 MPa. Part of the as-cast alloys was re-melted and spun by melt-spinning with a rotating copper roller. The spinning rate was approximately expressed by the linear velocity of the copper roller because it is too difficult to measure a real spinning rate i.e. cooling rate of the sample during spinning. The spinning rates used in the experiment were 15, 20, 25 and 30 m/s, respectively. The nominal compositions of the experimental alloys were $Mg_{20}Ni_{10-x}Cu_x$ (x = 0, 1, 2, 3, 4). For convenience, the alloys were denoted with Cu content as Cu_0, Cu_1, Cu_2, Cu_3 and Cu_4, respectively.

The morphologies of the as-cast alloys were observed by scanning electron microscope (SEM) (Philips QUANTA 400). The phase structures of the as-cast and spun alloys were determined by XRD diffractometer (D/max/2400). The diffraction, with the experimental parameters of 160 mA, 40 kV and 10°/min respectively, was performed with $CuK_{\alpha 1}$ radiation filtered by graphite. The thin film samples of the as-spun alloys were prepared by ion etching for observing the morphology with high resolution transmission electron microscope (HRTEM) (JEM-2100F, operated at 200 kV), and for determining the crystalline state of the samples with electron diffraction (ED).

The hydrogen absorption and desorption kinetics of the alloys were measured by an automatically controlled Sieverts apparatus. The hydrogen absorption was conducted at 1.5 MPa at 200 ℃ and the hydrogen desorption in a vacuum **(**1×10^{-4} MPa**)** at 200 ℃ too.

3. RESULTS AND DISCUSSIONS

3.1. Microstructure Characteristics

The SEM images of the as-cast alloy are illustrated in **Figure 1**, displaying a typical dendrite structure. The substitution of Cu for Ni does not change the morphology of the alloys but it causes a significant refinement of the grains. The result obtained by energy dispersive spectrometry (EDS) indicates that the major phase of the as-cast alloys is Mg_2Ni phase (denoted as A). Some small massive matters in the alloys containing Cu can clearly be seen in **Figure 1**, which are determined by EDS to be Mg_2Cu phase (denoted as B).

Figure 2 presents the XRD profiles of the as-cast and spun $Mg_{20}Ni_{10-x}Cu_x$ (x = 0, 1, 2, 3, 4) alloys, showing that the substitution of Cu for Ni does not change the phase structure. All the as-cast and spun alloys display a single phase structure. This seems to be contrary with the result of SEM observation. It is most probably associated with the fact that Mg_2Ni and Mg_2Cu hold completely identical structure and nearly same lattice constants. On the other hand, the amount of the Mg_2Cu phase is very little so that the XRD observation can not detect its presence. Listed in **Table 1** are the lattice parameters, cell volume and full width at half maximum (FWHM) values of the main diffraction peaks of the as-cast and spun (20 m/s) alloys which were calculated by software of Jade 6.0. It can be derived from **Table 1** that the substitution of Cu for Ni causes the FWHM values of the main diffraction peaks of the as-cast and spun alloys significantly increased, and it leads to the lattice parameters and cell volume of the alloys cleverly enlarged, which is attributed to the slightly larger atomic radius of Cu than Ni. It can be seen from **Table 1** that melt spinning causes the FWHM values of the main diffraction peaks of the alloys significantly increased which is doubtless attributed to the refinement of the grains and the stored stress in the grains produced by melt spinning. Based on the FWHM values of the broad diffraction peak (203) in **Figure 2b**, the crystallite size $\langle D_{hkl} \rangle$ (Å) of the as-spun alloy was calculated using Scherrer's equation. The grain sizes of the as-spun alloys are in a range of 2-6 nm, consistent with results reported by Friedlmeier *et al.* [23]. It is very important to notice that $\langle D \rangle$ values were calculated on the same peak having Miller indices (203) due to better possibility of mutual comparison.

Figure 3 shows HRTEM micrographs and electron diffraction patterns of the as-spun Cu_1 and Cu_3 alloys, which reveal a nanocrystalline microstructure, with an average crystal size of about 2-5 nm. This result agrees very well with the XRD observation shown in **Figure 2**.

SciRes Copyright © 2010

From HRTEM observations there is some evidence that the as-spun alloys are strongly disordered and nanostructured, but they are free of amorphous phase. Spassov *et al*. [21] reported that Mg-based alloys with nanocrystalline microstructures can be obtained by controlling the cooling rates. The crystal defects in the as-spun alloy, stacking faults (denoted as A), twin-grain boundaries (denoted as B), dislocations (denoted as C) and sub-grain boundaries (denoted as D), can clearly be seen in **Figure 4**.

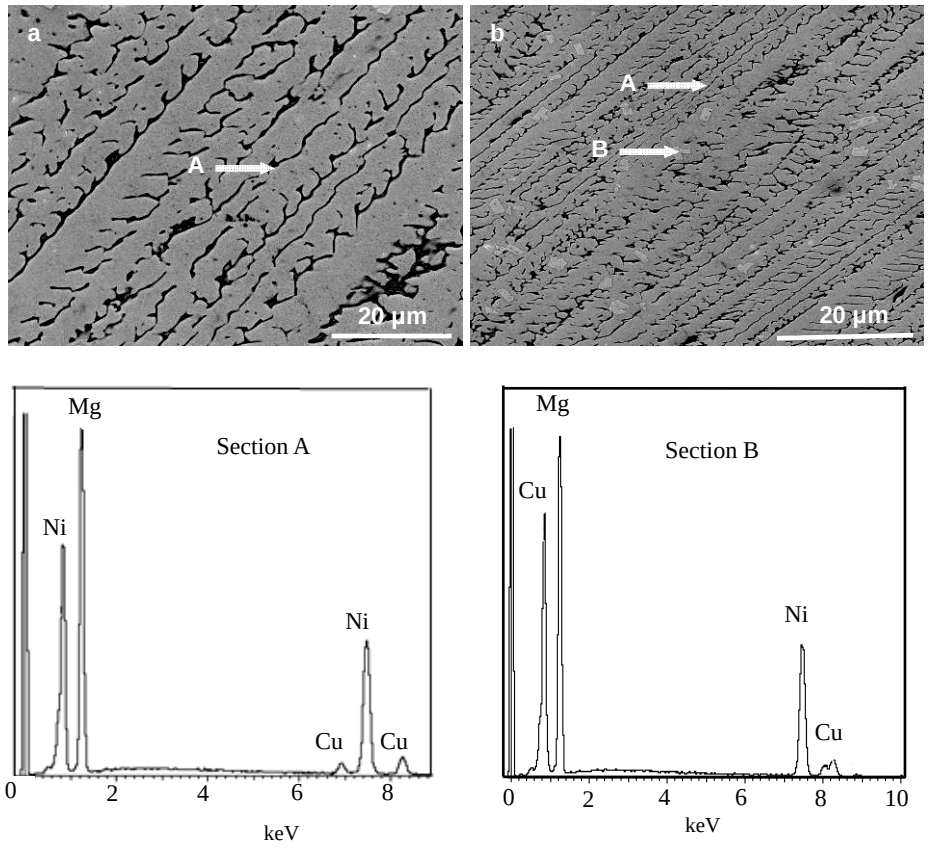

Figure 1. SEM images of the as-cast alloys together with EDS spectra of sections A and B in Figure 1 (b): (a) Cu_0 alloy, (b) Cu_4 alloy.

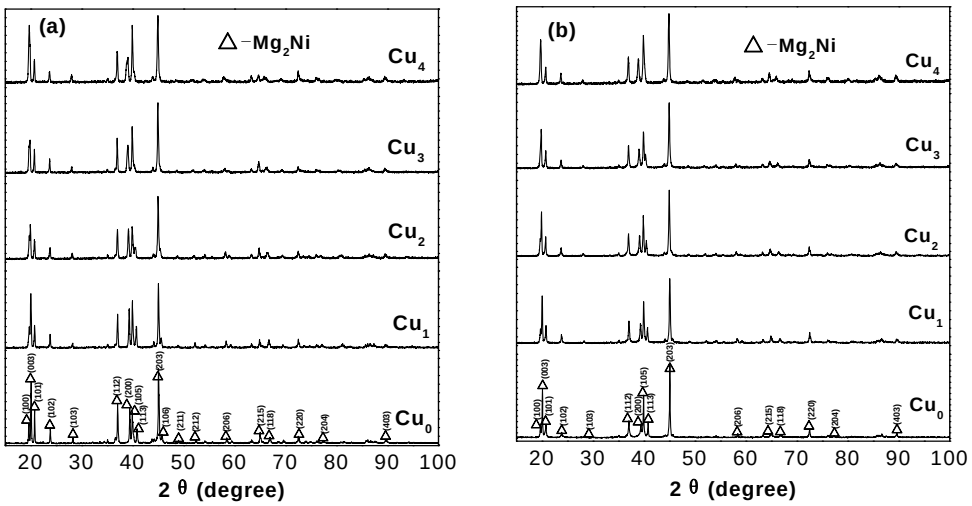

Figure 2. XRD profiles of the as-cast and spun alloys: (a) As-cast, (b) As-spun (20 m/s).

Table 1. The lattice parameters, cell volume and the FWHM values of the major diffraction peaks of the alloys.

Alloys	FWHM values				Lattice parameters and cell volume					
	2θ(20.02°)		2θ(45.14°)		a (Å)		c (Å)		V (Å^3)	
	As-cast	20m/s	As-cast	20m/s	As-cast	20 m/s	As-cast	20 m/s	As-cast	25 m/s
Cu_0	0.122	0.129	0.169	0.173	5.2097	5.2101	13.244	13.258	311.29	311.67
Cu_1	0.133	0.184	0.178	0.218	5.2102	5.2154	13.252	13.262	311.54	312.39
Cu_2	0.148	0.232	0.183	0.223	5.2136	5.2162	13.283	13.307	312.67	313.55
Cu_3	0.151	0.257	0.192	0.232	5.2154	5.2171	13.297	13.313	313.22	313.80
Cu_4	0.165	0.286	0.204	0.252	5.2171	5.2203	13.302	13.317	313.54	314.28

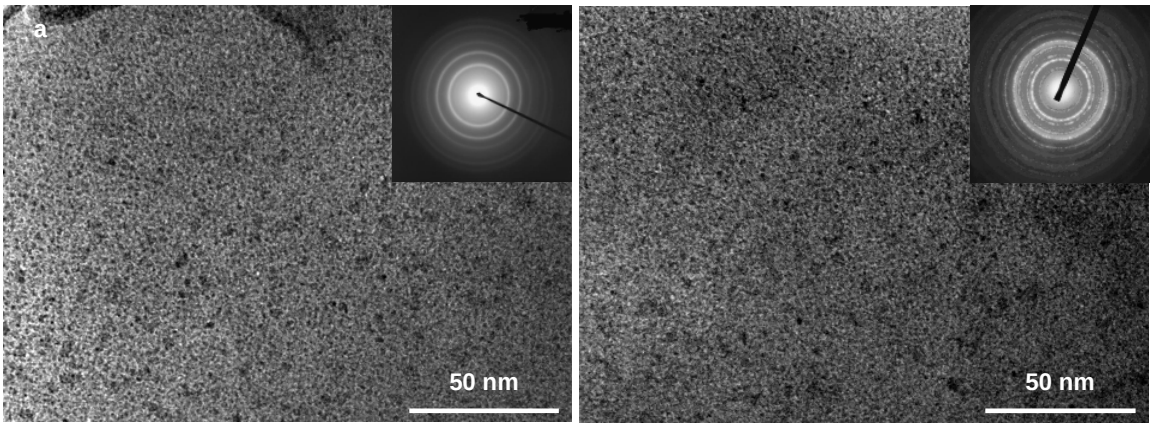

Figure 3. HRTEM micrographs and ED of the as-spun alloys (30 m/s): (a) Cu_1 alloy (b) Cu_3 alloy.

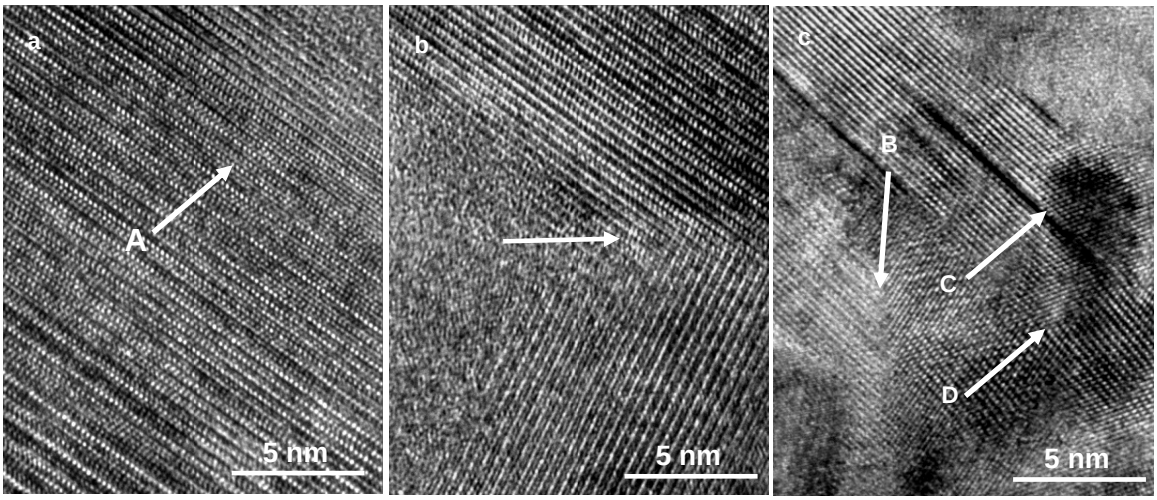

Figure 4. Crystal defects in the as-spun (30 m/s) Cu_3 alloy taken by HRTEM: (a) Stacking fault, (b) Twin grain boundary, (c) Dislocations and sub-grain boundaries.

3.2. Hydriding and Dehydriding Characteristics

Figure 5 shows the hydrogen absorption capacity and kinetics of the as-cast and spun Cu_1 and Cu_3 alloys. It can be seen that all the hydriding kinetic curves of the as-spun alloys show an initial fast hydrogen absorption stage after which the hydrogen content is saturated at longer hydrogenation time, indicating that the melt spinning significantly improves the hydrogen absorption property of the alloys. The hydrogen absorption capacities of the alloys increase with rising spinning rate. When the spinning rate grows from 0 (As-cast is defined as spinning rate of 0 m/s) to 30 m/s, the hydrogen absorption capacity of the Cu_1 alloy in 10 min rises from 1.99 to 3.12 wt.%, and from 1.74 to 2.88 wt.% for the Cu_3 alloy.

The hydrogenation kinetics and storage capacity of all the as-spun nanocrystalline Mg_2Ni-type alloys studied

SciRes Copyright © 2010

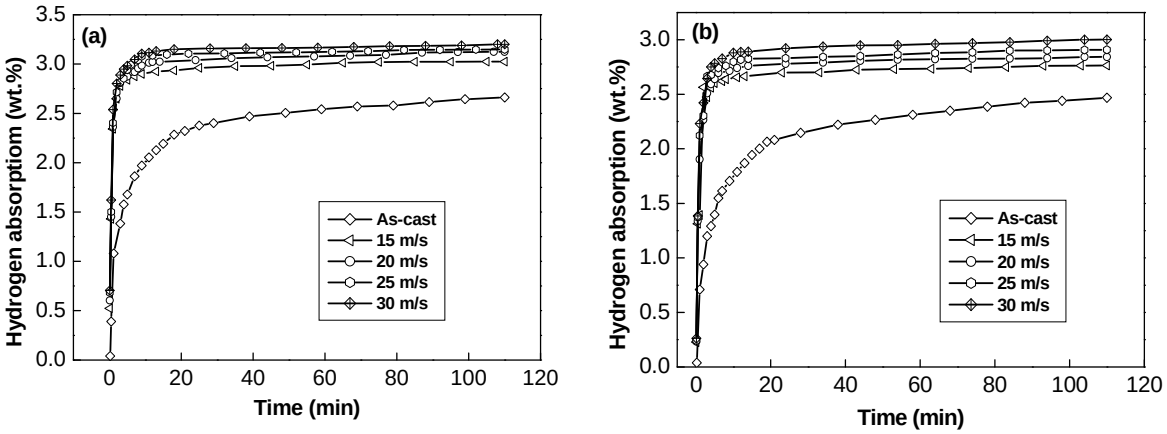

Figure 5. Hydrogen absorption kinetic curves of the as-cast and spun alloys: (a) Cu_1 alloy (b) Cu_3 alloy.

are superior to those of conventional polycrystalline materials with similar composition. The enhanced hydrogenation property by melt spinning is undoubtedly associated with the refinement of the grains produced by melt spinning [24]. By refining the microstructure, a lot of new crystallites and grain boundaries are created which can act as fast diffusion paths for hydrogen absorption. Based on the result reported by Orimo and Fujii [25], the distribution of the maximum hydrogen concentrations in three nanometer-scale regions, i.e. grain region and grain boundary region as well as amorphous region, have been experimentally determined to be 0.3 wt.% H in the grain region of Mg_2Ni, 4.0 wt.% H in the grain boundary and 2.2 wt.% H in the amorphous region. It revealed that the hydrides mainly exist in grain-boundary region and the amorphous phase region. The improved hydrogenation characteristics can be explained with the enhanced hydrogen diffusivity in the nanocrystalline microstructure as the nanocrystalline leads to an easier access of hydrogen to the nanograins, avoiding the long-range diffusion of hydrogen through an already formed hydride, which is often the slowest stage of absorption. It is known that the nanocrystalline microstructures can accommodate higher amounts of hydrogen than polycrystalline ones. The crystalline material, when melt spun, becomes at least partially disordered and its structure changes to nanocrystalline. Consequently, high densities of crystal defects such as dislocations, stacking faults and grain boundaries are introduced. The large number of interfaces and grain boundaries available in the nanocrystalline materials provide easy pathways for hydrogen diffusion and accelerates the hydrogen absorbing/desorbing process.

The hydrogen absorption kinetic curves of the as-spun alloys are plotted in **Figure 6**. It can be seen that the hydrogen absorption capacity of as-spun alloys first increases and then decreases with the variation of Cu content. The Cu_2 alloy shows a maximum hydrogen absorption capacity at 200℃. The kinetics of hydrogenation was extremely fast so that the alloys absorbed more than 95% of their hydrogen capacities within the first 5 min. The excellent hydriding kinetics is ascribed to the nanocrystalline structure because the high surface to volume ratios (high specific surface area) and the presence of large number of grain boundaries in nanocrystalline alloys enhance the kinetics of hydrogen absorption/ desorption. The positive function of Cu substitution on the hydrogen absorption capacity and kinetics of the alloy is attributed to the increased cell volume and the grain refined by Cu substitution. The increase of the cell volume is very helpful to hydrogen absorption capacity, and the grain boundary possesses the largest hydrogen absorption capability [25]. It was well known that the catalytic action of Ni on hydriding is stronger than Cu. Therefore, it is understandable that a superfluous amount of Cu substitution ($x>2$) must lead to a decrease of the hydrogen absorption capacity of the alloys.

Figure 7 shows the hydrogen desorption capacity and kinetics of the as-cast and spun Cu_1 and Cu_3 alloys, indicating that the dehydriding capability of the alloys obviously meliorates with rising spinning rate. When the spinning rate grows from 0 to 30 m/s, the hydrogen desorption capacity of the Cu_1 alloy in 20 min increases from 0.29 to 0.98 wt.%, and from 0.52 to 1.49 wt.% for Cu_3 alloy, respectively. The nanocrystalline Mg_2Ni-based alloys produced by melt spinning exhibit higher H-absorption capacity and faster kinetics of hydriding/ dehydriding than crystalline Mg_2Ni. A similar result was reported by Spassov *et al.* [21]. The specific capacity and hydriding/dehydriding kinetics of hydride materials depend on their chemical composition and crystalline structure [26]. The observed essential differences in the hydriding/dehydriding kinetics of the melt-spun nanocrystalline Mg_2Ni type alloys studied most probably have to be associated with the composition of the alloy as well as with the differences in their microstructure due to the different spinning rates. It was reported that

SciRes Copyright © 2010

the high surface to volume ratios, i.e. high specific surface area, and the presence of large number of grain boundaries in nanocrystalline alloys enhance the kinetics of hydrogen absorption/desorption [21]. Zaluski *et al.* [27] and Orimo *et al.* [28] confirmed that the hydriding/dehydriding characteristics at low temperatures (lower than 200℃) of nanocrystalline Mg_2Ni alloys prepared by mechanical alloying can be improved by reducing the grain size (20-30 nm), due to hydrogen occupation in the disordered interface phase.

The hydrogen desorption kinetic curves of the as-spun alloys are plotted in **Figure 8**. An important feature of the dehydrogenation process in the alloys is very slow initial hydrogen desorption, followed by slack increase in the amount of hydrogen desorbed. **Figure 8** indicates that the Cu substitution significantly improves the hydogen desorption capacity and kinetics of the alloys. When Cu content x increases from 0 to 4, the hydrogen desorption capacity of the as-spun (20 m/s) alloy in 20 min rises from 0.62 to 1.43 wt.%, and from 0.89 to 1.69 wt.% for the as-spun (30 m/s) alloy. Several possibilities can be considered as the reasons why the substitution of Cu for Ni enhances the hydrogen desorption kinetics of Mg_2Ni-type alloys. Firstly, the partial substitution of element Cu for Ni in Mg_2Ni compound decreases the stability of the hydride and makes the desorption reaction easier [29]. Secondly, the presence of Mg_2Cu phase apparently has catalytic effects for the hydriding and dehydriding reactions of Mg and Mg-based alloys [19]. Additionally, the addition of the third element Cu probably stabilizes the nanostructure of the alloy obtained by melt spinning, which could be very important for practical H-storage materials on the base of Mg_2Ni. In multicomponent Mg-based hydrogen storage alloys surface segregation and formation of microcrack passages for H-diffusion improve the kinetics of hydriding/dehydriding.

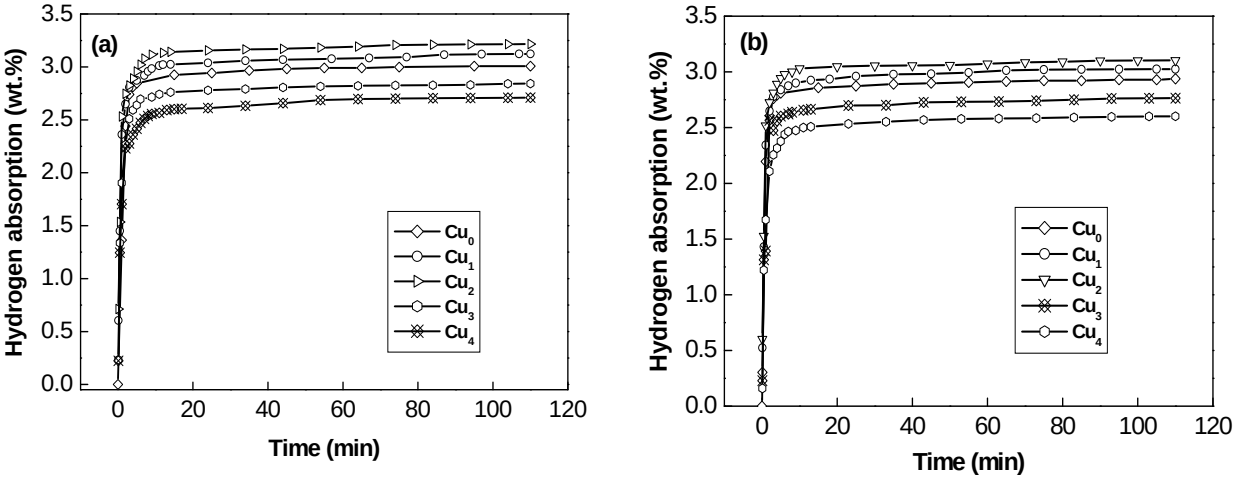

Figure 6. Hydrogen absorption kinetic curves of the as-spun alloys: (a) 20 m/s, (b) 30 m/s.

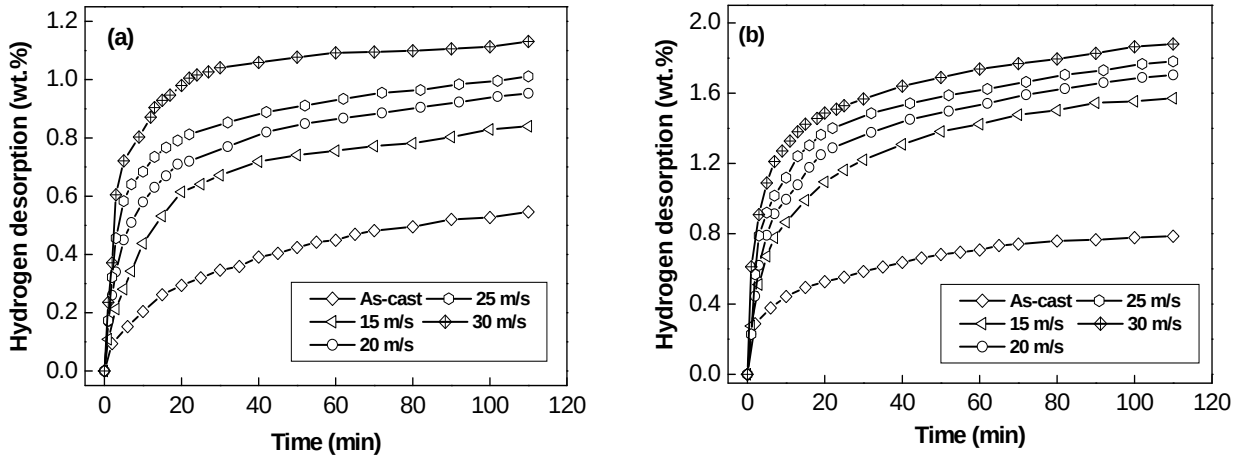

Figure 7. Hydrogen desorption kinetic curves of the as-cast and spun alloys: (a) Cu_1 alloy (b) Cu_3 alloy.

SciRes Copyright © 2010

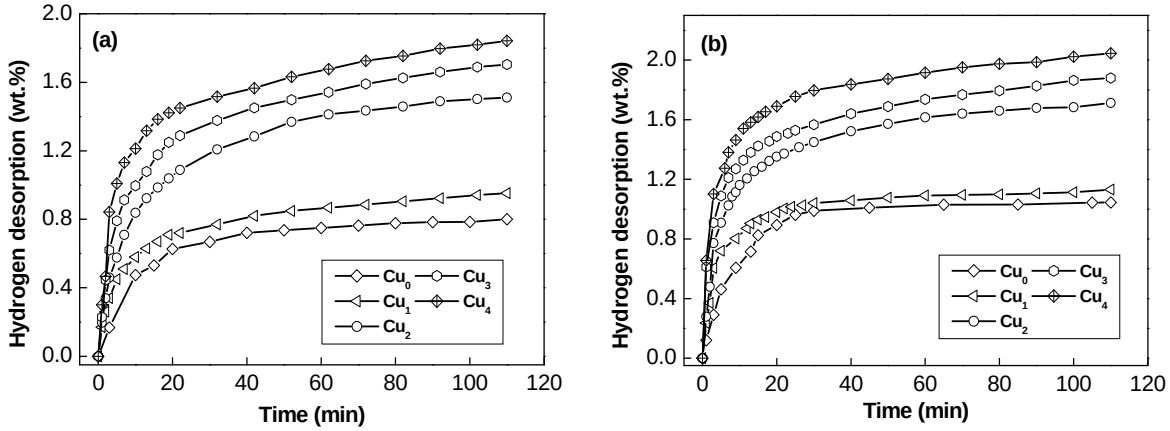

Figure 8. Hydrogen desorption kinetic curves of the as-spun alloys: (a) 20 m/s, (b) 30 m/s.

4. CONCLUSIONS

1) All the as-spun $Mg_{20}Ni_{10-x}Cu_x$ (x = 0, 1, 2, 3, 4) alloys hold nanocrystalline structures and are free of amorphous phase. The substitution of Cu for Ni does not change the major phase of the alloy, but it leads to a significant refinement of the grains and the formation of secondary phase Mg_2Cu in the as-cast alloys.

2) Melt spinning significantly improves the hydriding and dehydriding properties of the alloys. Hydriding and dehydriding capacities and rates of the alloy markedly rise with increasing spinning rate, which is mainly attributed to the formation of the nanocrystalline structure caused by melt spinning.

3) With the substitution of Cu for Ni, the hydrogen absorption capacity of the alloys first increases and then decreases. But it clearly improves the hydrogen desorption capacity and dehydriding rate of the alloys, for which the decreased stability of the hydride by Cu substitution is mainly responsible.

5. ACKNOWLEDGEMENTS

This work is supported by Hi-Tech Research and Development Program of China (2007AA03Z227), National Natural Science Foundations of China (50871050 and 50701011), Natural Science Foundation of Inner Mongolia, China (200711020703) and Higher Education Science Research Project of Inner Mongolia, China (NJzy08071).

REFERENCES

[1] Schlapbach, L. and Züttel, A. (2001) Hydrogen-storage materials for mobile applications [J]. *Nature*, **414**, 353-358.

[2] Simičić, M.V., Zdujić, M., Dimitrijević, R., *et al.* (2006) Hydrogen absorption and electrochemical properties of Mg_2Ni-type alloys synthesized by mechanical alloying [J]. *Journal of Power Sources*, **158**, 730-734.

[3] Schlapbach, L. (2002) Hydrogen as a fuel and its storage for mobility and transport [J]. *MRS Bulletin*, **27**, 675-676.

[4] Ebrahimi-Purkani, A. and Kashani-Bozorg, S.F. (2008) Nanocrystalline Mg_2Ni-based powders produced by high-energy ball milling and subsequent annealing [J]. *Journal of Alloys and Compounds*, **456**, 211-215.

[5] Kyoi, D., Sakai, T., Kitamura, N., *et al.* (2008) Synthesis of FCC Mg-Ta hydrides using GPa hydrogen pressure method and their hydrogen-desorption properties [J]. *Journal of Alloys and Compounds*, **463**, 306-310.

[6] Palade, P., Sartori, S., Maddalena, A., *et al.* (2006) Hydrogen storage in Mg-Ni-Fe compounds prepared by melt spinning and ball milling [J]. *Journal of Alloys and Compounds*, **415**, 170-176.

[7] Song, M.Y., Yim, C.D., Bae, J.S, *et al.* (2008) Preparation by gravity casting and hydrogen-storage properties of Mg-23.5 wt.%Ni-(5, 10 and 15 wt.%)La [J]. *Journal of Alloys and Compounds*, **463**, 143-147.

[8] Hima Kumar, L., Viswanathan, B. and Srinivasa Murthy S. (2008) Hydrogen absorption by Mg_2Ni prepared by polyol reduction [J]. *Journal of Alloys and Compounds*, **461**, 72-76.

[9] Liu, X.F., Zhu, Y.F. and Li, L.Q. (2008) Structure and hydrogenation properties of nanocrystalline Mg_2Ni prepared by hydriding combustion synthesis and mechanical milling [J]. *Journal of Alloys Compounds*, **455**, 197-202.

[10] Liu, F.J. and Suda, S. (1995) A method for improving the long-term storability of hydriding alloys by air water exposure [J]. *Journal of Alloys Compounds*, **231**, 742-750.

[11] Czujko, T., Varin, R.A., Chiu, C., *et al.* (2006) Investigation of the hydrogen desorption properties of Mg+10 wt.% X (X = V, Y, Zr) submicrocrystalline composites [J]. *Journal of Alloys Compounds*, **414**, 240-247.

[12] Gasiorowski, A., Iwasieczko, W., Skoryna., *et al.* (2004) Hydriding properties of nanocrystalline $Mg_{2-x}M_xNi$ alloys synthesized by mechanical alloying (M = Mn, Al) [J]. *Journal of Alloys Compounds*, **364**, 283-288.

[13] Sakintuna, B., Lamari-Darkrim, F. and Hirscher, M. (2007) Metal hydride materials for solid hydrogen storage: A review [J]. *International Journal of Hydrogen Energy*, **32**, 1121-1140.

[14] Gennari, F.C. and Esquivel, M.R. (2008) Structural characterization and hydrogen sorption properties of nanocrystalline Mg_2Ni [J]. *Journal of Alloys Compounds*, **459**, 425-432.

[15] Muthukumar, P., Prakash Maiya, M., Srinivasa Murthy,

SciRes Copyright © 2010

S., *et al.* (2008) Tests on mechanically alloyed Mg_2Ni for hydrogen storage [J]. *Journal of Alloys Compounds*, **452**, 456-461.

[16] Recham, N., Bhat, V.V., Kandavel, M., *et al*. (2008) Reduction of hydrogen desorption temperature of ball-illed MgH_2 by NbF_5 addition [J]. *Journal of Alloys Compounds*, **464**, 377-382.

[17] Dobrovolsky, V.D., Ershova, O.G., Solonin, Yu. M., *et al*. (2008) Influence of TiB_2 addition upon thermal stability and decomposition temperature of the MgH_2 hydride of a Mg-based mechanical alloy [J]. *Journal of Alloys Compounds*, **465**, 177-182.

[18] Liang, G. (2004) Synthesis and hydrogen storage properties of Mg-based alloys [J]. *Journal of Alloys Compounds*, **370**, 123-128.

[19] Song, M.Y., Kwon, S.N., Bae, J.S., *et al.* (2008) Hydrogen-storage properties of Mg-23.5Ni-(0 and 5)Cu prepared by melt spinning and crystallization heat treatment [J]. *International Journal of Hydrogen Energy*, **33**, 1711-1718.

[20] Savyak, M., Hirnyj, S., Bauer, H.D., *et al.* (2004) Electrochemical hydrogenation of $Mg_{65}Cu_{25}Y_{10}$ metallic glass [J]. *Journal of Alloys Compounds*, **364**, 229-237.

[21] Spassov, T. and Köster, U. (1998) Thermal stability and hydriding properties of nanocrystalline melt-spun $Mg_{63}Ni_{30}Y_7$ alloy [J]. *Journal of Alloys Compounds*, **279**, 279-286.

[22] Zhang,Y.H., Li, B.W., Ren, H.P., *et al.* (2009) Hydriding and dehydriding characteristics of nanocrystalline and amorphous $Mg_{20}Ni_{10-x}Co_x$ (x=0–4) alloys prepared by melt-spinning [J]. *International Journal of Hydrogen Energy*, **34**, 2684-2691.

[23] Friedlmeier, G., Arakawa, M., Hiraia, T., *et al.* (1999) Preparation and structural, thermal and hydriding characteristics of melt-spun Mg-Ni alloys [J]. *Journal of Alloys Compounds*, **292**, 107-117.

[24] Tanaka, K., Kanda, Y., Furuhashi, M., *et al.* (1999) Improvement of hydrogen storage properties of melt-spun Mg-Ni-RE alloys by nanocrystallization [J]. *Journal of Alloys Compounds*, **293-295**, 521-525.

[25] Orimo, S. and Fujii, H. (2001) Materials science of Mg-Ni-based new hydrides [J]. *Applied Physics A*, **72**, 167-186.

[26] Mulas, G., Schiffini, L. and Cocco, G. (2004) Mechanochemical study of the hydriding properties of nanostructured Mg_2Ni–Ni composites [J]. *Journal of Materials Research*, **19**, 3279-3289.

[27] Zaluski, L., Zaluska, A.J. and Ström-Olsen, O. (1997) Nanocrystalline metal hydrides [J]. *Journal of Alloys Compounds*, **253-254**, 70-79.

[28] Orimo, S., Fujii, H. and Ikeda, K. (1997) Notable hydriding properties of a nanostructured composite material of the Mg_2Ni-H system synthesized by reactive mechanical grinding [J]. *Acta Materialia*, **45**, 331-341.

[29] Woo, J.H. and Lee, K.S. (1999) Electrode characteristics of nanostructured MgNi-type alloys prepared by mechanical alloying [J]. *Journal of The Electrochemical Society*, **146**, 819-823.

SciRes Copyright © 2010

Vol.2, No.1, 26-32 (2010)
doi:10.4236/ns.2010.21004

Natural Science

Study of some Indian medicinal plants by application of INAA and AAS techniques

Ram Lokhande[1], Pravin Singare[2*], Mahadeo Andhele[1], Raghunath Acharya[3]

[1]Department of Chemistry, University of Mumbai, Mumbai, India
[2]Department of Chemistry, Bhavan's College, Mumbai, India; pravinsingare@vsnl.net
[3]Radiochemistry Division, Bhabha Atomic Research Centre, Mumbai, India

Received 15 September 2009; revised 18 October 2009; accepted 20 October 2009.

ABSTRACT

Instrumental neutron activation analysis (INAA) and atomic absorption spectroscopy (AAS) techniques were used to analyze 18 elements (K, Mn, Na, Fe, Zn, Cu, Co, Br, Sm, Cl, La, Al, Cr, Ca Cd, Ni, Pb and Hg) in different medicinal plants often used in Indian Ayurvedic system. The samples were irradiated with thermal neutrons in a nuclear reactor and the induced activities were counted by γ-ray spectrometry using efficiency calibrated high resolution High Purity Germanium (HPGe) detector. Most of the medicinal plants were found to be rich in one or more of the elements under study. The elemental concentration in different part of medicinal plants and their biological effects on human beings are discussed.

Keywords: Instrumental Neutron Activation Analyses; Atomic Absorption Spectroscopy; Medicinal Plants; Trace Elemental Analysis; Inter-Elemental Correlations

1. INTRODUCTION

There are many references to the curative properties of several herbs in the ancient Indian literature, *Rigveda*, though a more detailed account is found in the *Atharvaveda* from where *Ayurveda*, the Indian traditional health care system (*ayus*=life, *veda*=knowledge, meaning science of life) originated. Fairly comprehensive information about herbs has been recorded in two treatises *Charak Samhita* and *Shusruta Samhita*-a base for Ayurvedic system of medicine [1,2]. These herbs are now being increasingly used in cosmetics, food as well as alternative medicine [3]. Some of the ingredients of allopathic and most of the Ayurvedic and Homeopathy medicines are derived from plants. Traditional Indian medical herbs used for strengthening the body immune system are known to have many essential and nutritional elements. Their excess or deficiency may disturb normal biochemical functions of the body [4]. Some western scholars have pursued the analysis of various Indian plants and herbs for their medicinal properties [5]. Most studies on such medicinal plants pertain to their organic contents, viz. essential oils, glycosides, vitamins, alkaloids and other active components and their pharmacological/therapeutic effects. Besides, several organic compounds, it is now well established that many trace elements play a vital role in general well-being as well as in the cure of diseases [6,7]. Several studies have reported elemental contents in plant extracts, which are consumed by us either as an herbal health drink or medicine [8-10]. These elements are presented at varying concentrations in different parts of the plants, especially in roots, seeds and leaves which are used as a dietary item as well as ingredient in the Ayurvedic medicinal preparation. The leaves of the plants are still used in some countries, as for instance, in Malaysia [11], Greece [12] and India [13] particularly for their therapeutic effects. Since these trace elements constitute a minute fraction in different parts of the medicinal plants, a sensitive and reliable analytical technique is a prerequisite for obtaining precise and accurate data.

Considering the importance of trace elements in various human metabolic processes and also considering their curative properties, in the present investigation we have applied one of the sensitive analytical techniques like INAA to study the essential elemental content in different parts of Indian medicinal plants and herbs. The overall impact of these essential trace elements on human health is also discussed. Due to increasing industrialization and environmental pollution, the study was also extended to estimate the level of toxic elements present in these medicinal plant samples. Even though the direct link between the essential elemental content and their curative capacity is not yet established, the experimental data of the present work will be of im-

SciRes Copyright © 2010

mense importance in the synthesis of new Ayurvedic formulations. Also, it will help in deciding the proportion of various active constituents and managing dose of a particular formulation.

2. EXPERIMENTAL

2.1. Sampling

The various medicinal plants (**Table 1**) in the form of leaves and roots were collected from and around the Keshav Shrushti, Bhayander and Narsing K. Dube College, Nalasopara, Maharashtra, India. Surface contaminants of the plant samples were removed by washing with deionized water twice and then with deionized double distilled water. The leaves were air dried in a clean drying chamber and then dried at 80^{o}C for overnight in an oven. The samples were powdered in agate mortar and passed through 100-mesh sieve. Sampling was done from this powder.

2.2. Irradiation and Counting

About 50-80 mg of each sample was sealed in a polyethylene cover. Samples, reference standard and control sample were packed together and irradiated in the E8 position of the Apsara reactor, BARC. Irradiation time was varied between 30 min and 7 h depending on the half lives of the activation products. The sub-cadmium neutron flux in this position is in the order of $1x10^{12}cm^{-2}$ s^{-1}. The samples were also irradiated at Dhruva reactor for 1 d in order to determine the elemental concentration of the long-lived radionuclides, such as Fe. The short irradiation and counting were conducted at the reactor site followed by spectra unfolding at the Radiochemistry Division of BARC, Mumbai. The radionuclides used for the analysis and their γ energies are given in **Table 2**. All the samples and SRMs were counted at a calibrated sample-detector distance from a HPGe detector (Ortec) with 25% relative efficiency and 2.1 keV resolution at 1332.5 keV of ^{60}Co line, which was connected, to an IBM PC XT computer system. Most of the short lived isotopes contributing to the dead time belong to the elements present in major Ca and minor Al levels. The presence of different elements analyzed in various medicinal plants was confirmed by measuring their characteristic γ-ray energy as well as half lives which are in

Table 1. Medicinal plant samples selected for the study.

Sample Number	Local Name	Botanical Name	Parts of plants: Medicinal use
1	Karranj Beej	Pongamia pinnata	Seed: Cough, skin diseases, flatulence, diarrhoea, cough, arthritis, ulcers, wounds, diabetes, inflammation, low back pain, fever, hemorrhoids, and anemia. Seed oil is also used as insecticidal, nematicidal and bactericidal
2	Kutaja	Holarrhena antidysenterica	Seed: Constipation, Piles, acidity**,** diarrhoea, dysentery, hemorrhage, hemorrhoids, amoebiasis, hepatitis and skin diseases.
3	Jaiphal	Myristica fragrans	Seed: Constipation, in treating dehydration caused by vomiting and diarrhoea, particularly in cholera. It is used as an excellent sex tonic. It is used in treatment of insomnia, irritability, depression, skin diseases like ringworm and eczema. It is aromatic, carminative, digestive, anti-inflammatory, diuretic, lactagogue, aphrodisiac, hypnotic, hallucinogenic, antispasmodic and stimulant agent. Helps relieving flatulency, useful in nausea, stomachache, vomiting, diarrhoea associated with cholera. Also useful in diseases of the liver, spleen, headaches, palsy and eye troubles. Nutmeg oil stimulates the heart and circulation, activates the mind and relives people from fainting spells. The oil has good anti-inflammatory action, and is also successful in relieving pain, especially muscular aches and pain, as well as rheumatism.
4	Krishna Jiraka	Carum bulbocastanum	Seed: Appetizer, in dyspeptic problems, such as mild, sapstic conditions of the gastrointestinal tract, The Ayurvedic Pharmacopoeia of India recommended the seed in chronic fevers. Seed oil shows moderate antibacterial and antifungal activity against several bacteria and fungi. Mixed with alcohol and castor oil, it is used for scabies.
5	Babbul	Acacia arabica	Fruit: Epilepsy, Insomnia, Diarrhoea, teeth disorders, eczema, tonsillitis, conjunctivitis, epiphora, leucorrhoea, used in toothpastes and gargles.

SciRes Copyright © 2010

Table 2. Radionuclides used for the analysis and their γ-energies.

Nuclide	γ- ray energy in keV
^{42}K	1524.0
^{56}Mn	847.0
^{24}Na	1368.0
^{59}Fe	1099.0
^{65}Zn	1115.0
^{64}Cu	1040.0
^{60}Co	1332.0
^{82}Br	776.0
^{153}Sm,	103.0
^{38}Cl	1642.0
^{140}La	1596.0
^{28}Al	1779.0

Thermal neutron flux: 10^{12}-10^{13} n cm^{-2} s^{-1}.

good agreement with the literature values. Radioactivity measuring times were chosen not to exceed 0.2 times the half lives of the radionuclide of interest. Long irradiated samples were brought to Radiochemistry Laboratory at Mumbai University and γ-activity was measured. Counting was followed for 1, 2, 6 and 12 h at different intervals up to 3m. Care was taken to obtain maximum elemental information from more than one counting and the reproducibility of data was checked. Elemental concentrations of various Ayurvedic medicinal plants were calculated by relative method using control and reference multielemental standard as comparators.

2.3. Atomic Absorption Spectrometer (AAS) Measurement

The samples in the powdered form were accurately weighed and digested in (5:1) mixture of nitric acid and perchloric acid [14]. After digestion few drops of concentrated HCl was added. The solution was heated gently and then filtered. The residue was again subjected to digestion and filtrate was collected. The entire filtrate was diluted suitably with distilled deionized water. The dilute filtrate solution was used for analysis of elements of interest (Cr, Ca, Cd, Ni, Pb and Hg) by AAS (Perkin Elmer 3100 model) using suitable hollow cathode lamps. The elements were analyzed by AAS technique by measuring the absorbance of the species at its resonance wavelength. The concentration of various elements was determined by relative method using A.R. grade solutions of elements of interest. The standard conditions for atomic absorption measurement are represented in **Table 3**.

2.4. Quality Control

To provide quality control biological reference material, namely, Polish CRM Virginia Tobacco Leaves (CTA-VTL-2) was used. The concentrations of all the elements investigated in this study are well certified in the reference material. The SRMs of biological origin were analyzed for quality control and method validation. It was observed that most elemental contents are within±10% of the certified values. Standard deviations were also relatively small. The values listed in **Table 4** (which are averages of three independent measurements) are having the precision of ~ ± 2 to 10%.

Table 3. Standard conditions for atomic absorption measurement.

Element	Wavelength nm	Slit width nm	Sensitivity check ppm	Lamp current mA
Cr	357.9	0.2	4.0	7.0
Ca	422.9	0.5	4.0	10.0
Cd	228.8	0.5	1.5	4.0
Ni	232.0	0.5	7.0	4.0
Pb	283.6	0.5	20.0	5.0
Hg	253.7	0.5	200.0	4.0

3. RESULTS AND DISCUSSIONS

An examination of the data from **Table 4** shows that different medicinal plants contain elements like K,Mn, Na,Fe,Zn,Cu,Co,Br,Sm,Cl,La,Al,Cr,Ca,Cd,Ni,Pb and Hg in various proportions. The variation in elemental concentration is mainly attributed to the differences in botanical structure, as well as in the mineral composition of the soil in which the plants are cultivated. Other factors responsible for a variation in elemental content are preferential absorbability of the plant, use of fertilizers, irrigation water and climatological conditions [15].

An examination of the data from **Table 4** indicates that fruits of Babbul contain high K (8.79 mg/g), and low Na (0.08 mg/g) concentration. The K content is low in seeds of Kutaja (1.06mg/g), while Na content is to the maximum of 0.90 mg/g in seeds of Jaiphal. It is important here to note that the regulation of potassium is intimately involved with that of sodium and the two are largely interdependent. Potassium is accumulated within human cells by the action of the Na^+, K^+-ATPase (sodium pump) and it is an activator of some enzymes; in particular co-enzyme for normal growth and muscle function [16].

The calcium content in various medicinal plants analyzed varies from 1.58 mg/g in Karranj Beej to 15.1 mg/g in Kutaja. Calcium is essential for healthy bones, teeth and blood [17,18]. The health of the muscles and nerves depends on calcium. It is required for the absorption of dietary vitamin B, for the synthesis of the neurotransmitter acetylcholine, for the activation of enzymes such as the pancreatic lypase. The recommended daily dietary allowance of Ca for children is between 500 and 1000 mg, and 800 mg for adults. The appreciable high Ca content in fruits of Babbul suggests its possible use in toothpastes and gargles to overcome deficiency of Ca.

SciRes Copyright © 2010

Table 4. Elemental analysis of some medicinal plants by NAA and AAS techniques.

Name of the medicinal plant (Botanical name)	Parts used	Elements																	
		K (mg/g)	Mn (µg/g)	Na (mg/g)	Fe (µg/g)	Zn (µg/g)	Cu (µg/g)	Co (µg/g)	Br (µg/g)	Sm (µg/g)	Cl (mg/g)	La (µg/g)	Al (mg/g)	Cr † (µg/g)	Ca † (mg/g)	Cd † (µg/g)	Ni † (µg/g)	Pb † (µg/g)	Hg † (µg/g)
Karranj Beej (Pongamia pinnata)	Seed	1.75 (±0.10)	28.54 (±1.50)	0.85 (±0.03)	601 (±37)	75.30 (±3.67)	0.64 (±0.04)	83 (±4.7)	8.16 (±0.3)	0.66 (±0.04)	2.27 (±0.14)	0.73 (±0.04)	0.33 (±0.02)	2.11 (±0.13)	1.58 (±0.10)	3.00 (±0.14)	4.90 (±0.21)	1.30 (±0.08)	3.10 (±0.14)
Kutaja (Holarrhena antidysenterica)	Seed	1.06 (±0.08)	49.20 (±2.19)	0.43 (±0.02)	382 (±21)	46.90 (±2.76)	2.44 (±0.13)	6.2 (±0.4)	0.27 (±0.01)	0.33 (±0.02)	2.60 (±0.13)	8.44 (±0.51)	2.45 (±0.14)	1.80 (±0.11)	15.1 (±1.2)	3.10 (±0.19)	3.60 (±0.15)	0.90 (±0.04)	4.32 (±0.21)
Jaiphal (Myristica fragrans)	Seed	1.24 (±0.10)	98.10 (±5.55)	0.90 (±0.06)	261 (±23)	95.0 (±4.7)	4.25 (±0.22)	18.0 (±1.1)	9.14 (±0.27)	0.10 (±0.01)	2.53 (±0.11)	0.84 (±0.06)	3.11 (±0.21)	0.80 (±0.04)	5.46 (±0.41)	4.40 (±0.28)	1.65 (±0.08)	1.30 (±0.07)	ND
Krishna Jiraka (Carum Bulbocastanum)	Seed	1.39 (±0.11)	188.10 (±9.97)	0.22 (±0.01)	274 (±25)	40.2 (±2.1)	2.11 (±0.15)	8.9 (±0.3)	10.2 (±0.8)	0.42 (±0.02)	0.14 (±0.01)	ND	0.77 (±0.03)	ND	2.77 (±0.12)	1.80 (±0.09)	0.66 (±0.03)	1.20 (±0.08)	ND
Babbul (Acacia Arabica)	Fruit	8.79 (±0.30)	89.0 (±4.0)	0.08 (±0.002)	261 (±24)	73.5 (±3.7)	21.4 (±1.6)	2.8 (±0.1)	21.6 (±1.3)	0.31 (±0.02)	6.12 (±0.28)	ND	1.22 (±0.10)	2.71 (±0.13)	12.6 (±1.0)	1.21 (±0.07)	5.04 (±0.21)	1.00 (±0.05)	0.10 (±0.001)
CTA VTL-2 (Virginia Tobacco Leaves)		[10.3] {10.0} (±0.09)	[79.7] {80.2} (±7.5)	[0.312] {0.308} (±0.02)	[1083] {1100} (±104)	[43.3] {44.1} (±2.7)	[18.2] {18.9} (±0.9)	[0.429] {0.445} (±0.02)	[14.3] {15.2} (±1.0)	[0.157] {0.162} (±0.01)	[7.43] {7.25} (±0.31)	[1.01] {1.07} (±0.08)	[1.682] {1.704} (±0.07)	[1.87] {1.79} (±0.09)	[36.0] {35.4} (±1.9)	[1.52] {1.53} (±0.06)	[1.98] {2.01} (±0.10)	[22.1] {22.9} (±1.1)	[0.048] {0.050} (±0.002)

†Elements detected by AAS technique; (±) Standard deviation; [ ] Certified values; { } Measured values; ND=Not detected.

The elements like Zn, Fe and Cr are essential trace elements (micro nutrients) for living organisms. Zinc is relatively non-toxic [19]. Zinc deficiency is characterized by recurrent infections, lack of immunity and poor growth. Growth retardation, male hypogonadism, skin changes, poor appetite and mental lethargy are some of the manifestations of chronically zinc-deficient human subjects [19]. Zinc is necessary for the growth and multiplication of cells (enzymes responsible for DNA and RNA synthesis), for skin integrity, bone metabolism and functioning of taste and eyesight [20]. From the results obtained, it is observed that the concentration of Zn ranges from 95.0 µg/g in Jaiphal to 40.2 µg/g in Krishna Jirak. The high concentration of zinc in seeds of Jaiphal suggests its possible use in sex tonic, treatment of worms, skin disease, and eye trouble. The appreciable high Zn content in Karranj beej and Babbul may also be helpful in treatment of skin disease. Iron occupies a unique role in the metabolic process. The role of iron in the body is clearly associated with hemoglobin and the transfer of oxygen from lungs to the tissue cells [21]. Iron deficiency is the most prevalent nutritional deficiency in humans [22] and is commonly caused by insufficient dietary intake, excessive menstrual flow or multiple births. In this case, it results especially an anemia. In various medicinal plants samples analyzed, the Fe content was observed maximum in seeds of Karranj beej (601µg/g) and minimum in seeds of Jaiphal and Babbul (261µg/g). Hence the use of Karranj beej seeds in general tonic preparation may be advised to compensate for treatment of anemia. Chromium plays an important role in diabetes treatment. It is an important element required for the maintenance of normal glucose metabolism. The function of chromium is directly related to the function of insulin, which plays a very important role in diabetes. Chromium is found in the pancreas, which produces insulin. One usable form of chromium is the Glucose Tolerance Factor (GTF) [23], an inorganic compound containing glutamic acid, cysteine and niacin. The absorption of the trivalent chromium in GTF is about 10 to 25%. It enhances the removal of glucose from the blood. The important constituent of GTF is Cr which helps in the potentiating of insulin [24]. Chromium also acts as an activator of several enzymes. Deficiency of chromium decreases the efficiency of insulin and increases sugar and cholesterol in the blood. Chromium deficiency can cause an insulin resistance, impair in glucose tolerance and may be a risk factor in artherosclerotic disease [25]. From the results obtained, it is observed that Cr content is high in fruits of Babbul (2.71 µg/g) and seeds

SciRes Copyright © 2010

of Karranj beej (2.11 μg/g). Hence the use of this medicinal plant may be advised for the treatment and control of diabetics.

In experiments conducted by Anke *et al.* [26] with growing, gravid and lactating goats, a poor Br-nutrition (<1 mg/g dry matter) led to a significantly reduced growth, a worse conception rate, reduced milk fat production and decreased hemoglobin content. The high concentration of Br along with Fe in Karranj beej, Jaiphal, Babbul and Krishna jiraka suggests there possible use in preparation of drugs for curing natural diuretic, phlegm eliminating and stomach invigorating diseases [27] and purifying breast milk. However, further investigations regarding possible essentiality of Br are necessary due to the fact that Br accumulates well in plants due to the application of agricultural chemicals such as methyl bromide as fumigant.

The higher Mn content was observed in seeds of Krishna jiraka (188.1 μg/g). It is important here to note that Mn is an essential element required for various biochemical processes [28]. Mn is also important for several enzymatic processes. It helps in eliminating fatigue and reduces nervous irritability [7,29,30]. Hence use of Krishna jiraka seeds in medicinal preparations may help to supplement Mn for various body functions.

The Co content was observed to be high in Karranj beej (83.0 μg/g). Cobalt is an essential element for the plants having the capability to fix nitrogen in the root tubercles. Animals are able to synthesize vitamin B12, which is the main source of Co in animal foods. Nevertheless, only a part of Co in food derived from animals is present in the form of cobalamines. The recommended daily intake of vitamin B12 for adults is 3 mg (0.13 mg Co), taking into account that only 50% is absorbed in the intestine [20]. In humans, deficiency of vitamin B12 leads to a megaloblastic anemia. Cobalt also plays an important role in thyroid metabolism in humans. The higher Co and Fe content in Karranj beej suggests there use in medicinal preparation for treatment of anemia.

The elements like Hg, Pd, Cd and Ni are supposed to be toxic in nature and their presence in trace amount in various medicinal plant sample analyzed is due to the pollution arising from automobile and industrial activities.

3.1. Inter-Elemental Correlations

Several literature reports suggest interrelationship of essential elements like K, Na, Fe, Co and Zn [6,10,14]. The regulation of metal ion flows, especially of K^+ and Na^+, is crucial to life and is most clearly exemplified by the ionic movements that occur in nerve cells during excitation and transmission of the action potential. The regulation of potassium is intimately involved with that of sodium and the two are largely interdependent. From the experimental data, it is observed that K/Na ratio varies between minimum of 1.4 in Jaiphal to maximum of 109.9 in Babbul. The result indicates that potassium content is 1.4 times of sodium in Jaiphal, and 110 times in Babbul. The variation of K/Na ratio for different plant samples is graphically represented in **Figure 1**. The transition elements Fe, Zn and Co are well known for their role in biochemical processes [10]. Iron deficiency is common in uremic patients, it causes substantial blood losses. Some reports indicate that dysgeusia, poor food intake, and impaired sexual function, which are common problems of uremic patients, may be improved by zinc supplements [31]. In blood, about 85% of the zinc combines with protein for transport after its absorption, and its turnover is rapid in the pancreas. Deficiency of zinc causes diabetic hyposima, hypogeusia or coma [15]. The availability of Zn in the range of 14.8-8.4 μg/g may be beneficial for diabetic patients as its deficiency has been correlated with acute and chronic mal absorption states [30,32]. Similarly Fe is important because it eliminates phlegm and strengthens the function of stomach. Iron is found in body tissue enzymes and helps with energy metabolism. It facilitates the oxidation of carbohydrates, protein and fat to control body weight, which is very important in diabetes [15]. The requirement of Fe for an adult is 20 mg/day and for a child is 10 mg/day. From the result of medicinal plants analyzed, Fe/Zn ratio varies from 2.7 in Jaiphal to 8.1 in Kutaja (**Figure 2**). Cobalt in the form of Vitamin B-12 is in its physiologically active form. It is very essential to provide 3 μg per day in the form of Vitamin B-12 for a diabetic individual. A plot of Fe versus Co shows linear relationship (**Figure 3**) with r=0.907, which represents somewhat poor relationship. It is possible due to the fact that all parts of the medicinal plants are different i.e. seeds and fruits as reported by Razic *et al.* [33]. In general, it may be mentioned that interrelationship of several elements in medicinal herbs suggest synergistic or antagonistic effects, thus providing various elements to the body in bio-available form in a balanced manner with almost no harmful effects except some environmental contaminants. These, however, should be avoided by collecting herbs grown in a clean and well controlled environment [10].

4. CONCLUSIONS

Although there appears to be little knowledge of the precise molecular mechanisms, many Ayurvedic preparations nevertheless appear to demonstrate significant success in treatment of complex diseases. Presumably Ayurvedic medicines contain trace elements in a bio-available form and their impact on the overall pharmacological action cannot be ruled out. Although the direct link between elemental content and curative capability is yet to be established, such studies are vital to understanding the pharmacological action of herbs. The

SciRes Copyright © 2010

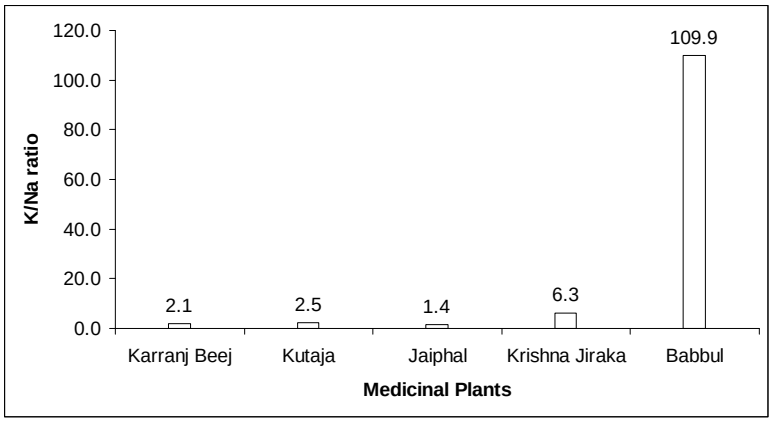

Figure 1. Variation of K/Na ratio in different medicinal plant samples.

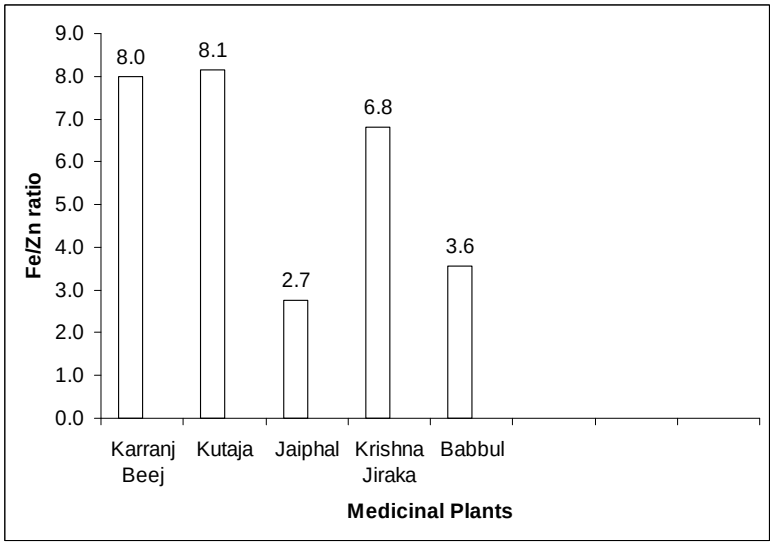

Figure 2. Variation of Fe/Zn ratio in different medicinal plant samples.

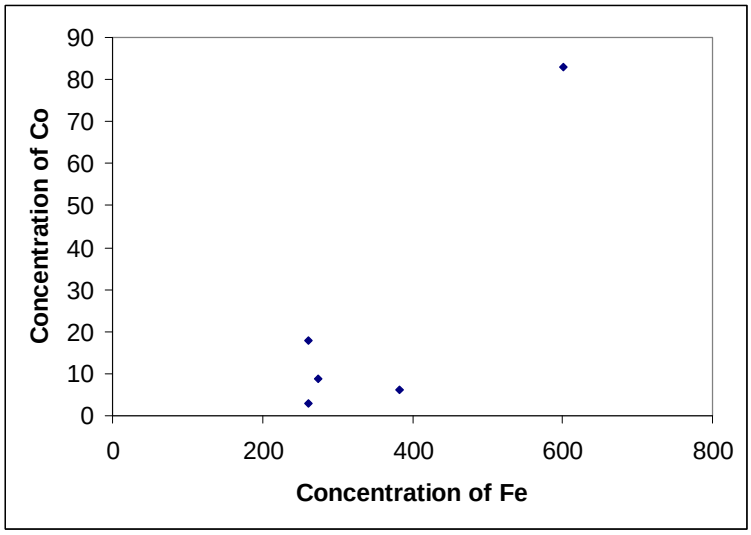

Figure 3. Correlation between Fe and Co concentrations in different medicinal plant samples. Correlation coefficient (r)=0.907.

SciRes Copyright © 2010

data obtained in the present work will be helpful in the synthesis of new Ayurvedic drugs which can be used for the control and cure of various diseases. In order to develop a stronger basis for appreciating the curative effects of medicinal plants, there is a need to investigate, their elemental composition. It has been demonstrated that INAA, with multi-elemental characterization over a wide range of concentration, its blank free-nature and minimum sample preparation is ideal for such studies.

REFERENCES

[1] Parchure, S.N. (1983) *Charak Samhita*, Sagar Publications, Pune, **1-3**.

[2] Sharma, P.V. (1993) *Dravya Guna Vigyan*, Chaukhamba Bharati Academy, Varanasi.

[3] Bakhru, H.K. (1998) Herbs that heal natural remedies for good health. *Orient Paperbacks*, Division of Vision Book Pvt. Ltd, New Delhi.

[4] Lyengar, G.V. (1989) *Elemental Analysis of Biological Systems: Biomedical Environmental, Compositional and Methodological Aspects of Trace Elements*, Boca Raton, CRC Press, Florida, **1,** pp. 242.

[5] Ambasta, S.P. Ed. (1986) *The Useful Plants of India*, CSIR, New Delhi, pp. 918.

[6] Underwood, E.J. (1977) *Trace Elements in Human and Animal Nutrition*, 4th Ed, Academic Press, New York, pp. 543.

[7] Prasad, A.S. (1993) *Essential and Toxic Elements in Human Health and Disease: An Update*, Wiley-Liss, New York.

[8] Powel, J.J., Burden, T.J. and Thompson, R.P.H. (1998) In vitro mineral availability from digested tea: A rich dietary source of manganese. *Analyst*, **123,** pp. 1721.

[9] Abou Arab A.A.K. and Donia, M.A.A. (2000) Heavy metals in Egyptian spices and medicinal plants and the effect of processing on their levels. *J. Agri. Food Chem.*, **48,** pp. 2300.

[10] Kumar, A., Nair, A.G.C., Reddy, A.V.R. and Garg, A.N. (2005) Analysis of essential elements in Pragya-peya-a herbal drink and its constituents by neutron activation. *J. Pharma. Biomed. Anal.*, **37,** pp. 631.

[11] Majid, A.A.B., Sarmani, S., Yusoe, N.I., Wie, Y.K. and Hamzah, F. (1995) Trace elements in Malaysian medicinal plants. *J. Radioanal. Nucl. Chem.*, **195,** pp. 173.

[12] Kanias, G.D., Kilikoglou, V., Tsitsa, E. and Loukis, A. (1993) Determination and statistical analysis of trace element and active constituent concentrations in the medicinal plant Eucalyptus Camaldulensis Dehnh (E. Rostratus schlecht). *J. Radioanal. Nucl.Chem.*, **169,** pp. 483.

[13] Patel, N.G. (1986) India's traditional medicine: Ayurveda. In: Steiner, R.P. Ed., *Folk Medicine: The Art and the Science*, American Chemical Society, Washington D.C.

[14] Herber, R.F.M. and Stoeppler, M. Eds. (1994) *Trace Element Analysis in Biological Specimens*, Elsevier, New York.

[15] Rajurkar, N.S. and Pardeshi, B.M. (1997) Analysis of some herbal plants from India used in the control of diabetes mellitus by NAA and AAS techniques. *Appl. Radiat. Isot.*, **48,** pp. 1059.

[16] Birch, N.J. and. Padgham, C (1994) Potassium. In: Seiler, H. G., Sigel, A. and Sigel, H. Eds., *Handbook on Metals in Clinical and Analytical Chemistry*, Marcel Dekker, New York.

[17] Charles, P. (1992) Calcium absorption and calcium bioavailability. *J. Int. Med.*, **231,** pp. 161.

[18] Hughes, M.N. (1972) *The Inorganic Chemistry of Biological Processes*, Wiley, London.

[19] Prasad, A.S. (1982) Clinical and biochemical spectrum of zinc deficiency in human subjects. In: Prasad, A.S. Ed., *Clinical, Biochemical and Nutritional Aspects of Trace Elements*, Alan R. Liss, Inc, New York.

[20] Thunus, L. and Lejeune, R. (1994) Cobalt, Zinc. In: Seiler, H.G., Sigel, A. and Sigel, H. Eds., *Handbook on Metals in Clinical and Analytical Chemistry*, Marcel Dekker, New York.

[21] Sigel, H. Ed. (1978) Iron in model and natural compounds. *Metals in Biological Systems*, Marcel Dekker, New York, **7**.

[22] Reddy, M.B., Chidambaram, M.V. and Bates, G.W. (1987) In: Winkelmann, G., Helm, Van der D. and Neilands, J.B. Eds., *Iron Transport in Microbes, Plants and Animals*, VCH, New York.

[23] Zetic, V.G. Tomas, V.S. Grba, S. Lutilsky, L. and Kozlek, D. (2001) Chromium uptake by Saccharomyces cerevisiae and isolation of glucose tolerance factor from yeast biomass. *J. Biosci.*, **26,** pp. 217.

[24] Anderson, R.A. (1989) Essentiality of chromium to humans. *Sci. Total Environ.*, **86,** pp. 75.

[25] Mertz, W. (1982.) Clinical and public health significance of chromium. In: Prasad, A.S. Ed., *Clinical, Biochemical and Nutritional Aspects of Trace Elements*, Alan R. Liss, Inc, New York.

[26] Anke, M., Groppel, B., Arnhold W., and Larger, M. (1988) Essentiality of the trace element Bromine. In: Briitter, P. and Schramel, P. Eds., *Trace Element Analytical Chemistry in Medicine and Biology*, Walter de Gruyter, Berlin, New York, **5**.

[27] Chen, K.S., Tseng, C.L. and Lin, T.H. (1993) Trace elements in natural drugs determined by INAA. *J. Radioanal. Nucl. Chem.*, **170,** pp. 265.

[28] Guenther, W. and Konieczynski, P. (2003) Speciation of Mg, Mn, and Zn in extracts of medicinal plants. *Anal. Bioanal. Chem.*, **375,** pp. 1067.

[29] Hamilton, E.M.N., Whitney, E.N. and Sizer, F.S. (1994) *Nutrition: Concepts and Controversies*, 4th Ed., St. Paul, West Publishing Co, MN, USA.

[30] O'Dell, B.L. and Sunde, R.A. Eds. (1997) *Handbook of Nutritionally Essential Mineral Elements*, Marcell Dekker Inc, New York.

[31] Shils, M.E. and Young, V.R. (1988) *Modern Nutrition in Health and Diseases*, 7th Ed, K. M. Verghese Co.

[32] Garg, A.N., Kumar, A., Maheshwari, G. and Sharma, S. (2005) Isotope dilution analysis for the determination of Zinc in blood samples of diabetic patients. *J. Radioanal. Nucl.Chem.*, **263,** pp. 39.

[33] Razic, S., Onjia, A. and Potkonjak, B. (2003) Trace elements analysis of Echinacea purpurea-herbal medicinal. *J. Pharm. Biomed. Anal.*, **33,** pp. 845.

SciRes Copyright © 2010

Vol.2, No.1, 33-40 (2010)
doi:10.4236/ns.2010.21005

Natural Science

Toxicity evaluation of produced formation waters after filtration treatment

Loredana Manfra, Chiara Maggi, Jessica Bianchi, Michela Mannozzi, Olga Faraponova, Livia Mariani, Fulvio Onorati, Andrea Tornambè, Claudia Virno Lamberti, Erika Magaletti

ISPRA, Advanced Institute for Environmental Protection and Research, Rome, Italy; loredana.manfra@isprambiente.it

Received 19 June 2009; revised 24 July 2009; accepted 28 July 2009.

ABSTRACT

During the last years many authors have characterized the produced formation waters (PFW_s) with respect to chemical compounds and toxicity. Most of data are related to PFW_s collected on offshore platform after treatment process. The available results showed that the particulate phase had an influence on PFW toxicity. Assuming the toxicity of PFW_s treated on platform, the aim of this paper is to study the toxicity of these PFW_s after a further filtration treatment carried out in laboratory. For this purpose PFW_s were sampled from three natural gas platforms located in the Adriatic Sea (Italy) below treatment system. The eco-toxicological bioassays have been conducted on test-organisms belonging to different trophic levels such as bacteria, algae, crustaceans and fishes. The PFW_s resulted toxic according to an overall assessment obtained through the bioassays. Furthermore, it has been possible to identify the species that were more sensitive to the tested PFW_s, namely Tigriopus fulvus, Dicentrarchus labrax and Vibrio fischeri. Besides, a chemical characterization was reported related to the contaminants present in the PFW_s to go with eco-toxicological assessment. Barium, zinc and manganese showed the most concentrations among the metals and the lower molecular weight components were common among the organic compounds. Some differences among PFW_s were observed both for toxicity and chemical composition. The highest toxicity was recorded in PFW_s (PFW1 and PFW2) containing the highest concentrations of some metals (Ba, Mn and Zn) and/or BTEX.

Keywords: Adriatic Sea (Italy); Offshore Platforms; Natural Gas Production Fields; Produced Formation Waters; Toxicity Assessment; Bacterium (Vibrio Fischeri); Algae (Dunaliella Tertiolecta and Phaeodactylum Tricornutum); Crustaceans (Artemia Franciscana and Tigriopus Fulvus); Fish (Dicentrarchus Labrax); Chemical Characterization

1. INTRODUCTION

Produced formation water (PFW) is water naturally present in sedimentary formations from which oil and gas are mined. It is piped to the surface during the production process and may be discharged into the sea when the rejection is not possible. Before discharge, PFW_s are treated directly on platform to reduce oil and solid suspended content [1]. In spite of this treatment, PFW_s still include oil and particles.

In Italy, like in other Countries, the legislation binds to control the oil content in the PFW when they are discharged into the sea [2]; for this reason, the PFW characterization has been limited for several years to measurement of "oil in water", which means analysis of non polar aliphatic hydrocarbons. However, PFW contains a variety of compounds such as metals (i.e. barium, copper, zinc, and iron), volatile aromatic compounds (benzene, toluene, ethylbenzene, xylenes, called BTEX), semi-volatile compounds (naphthalene, phenanthrene, dibenzothiophene and their C1-C3 alkyl homologues), phenols alkylated up to C7, organic acids (C1-C6 compounds) and some additives of possible employment (i.e. diethylene glycol, called DEG) [3].

For this reason, during the last years many authors have characterized PFW_s with respect to these compounds (metals, aromatic and aliphatic hydrocarbons, phenols and additives) and to the toxicity of PFW_s.

The most data-gathering is related to PFW_s collected on platform after treatment process and untreated in laboratory later on [4-8]. Few data are referred to PFW_s collected on oil platforms below treatment system and filtered in laboratory subsequently [3,9].

There are scattered data about PFW_s originated from Italian offshore gas installations (Adriatic Sea): some

SciRes Copyright © 2010

chemical analyses were made on seawaters and mussels near Adriatic platforms [10]; a methodological approach was proposed to study the environmental impact of oil and gas offshore platforms [11]; preliminary results were published on metal content and toxicity of PFW_s coming from gas Adriatic platforms [12-15].

In these studies, the PFW_s generally showed to be toxic and their toxicity was higher for samples unfiltered in laboratory. This effect was observed probably because of particulate phase influence. The effects of particulate could be to mechanic level (oral ingestion and digestion) and/or a chemical process (adsorption) [7,12].

The aim of this paper was to investigate the toxicity of PFW_s originated from three natural gas platforms in the Adriatic Sea (Italy). These PFW_s were collected below treatment system occurred on platforms and then filtered in laboratory. Their toxicity was evaluated using the integrated response of many species. The eco-toxicological battery included six species belonging to different trophic levels: a bacterium (*Vibrio fischeri)* representative of the debris chain, two algae species (*Dunaliella tertiolecta* and *Phaeodactylum tricornutum*) as primary producers, two crustaceans (*Artemia franciscana* and *Tigriopus fulvus*) as primary consumers and a fish (*Dicentrarchus labrax*) as representative of the highest trophic level (secondary consumer).

Besides, a chemical characterization of PFW_s was reported to go with eco-toxicological assessment. We investigated the metals, BTEX, PAHs and DEG. Metals and PAHs were analyzed both in filtered and particulate PFW_s, because these compounds are present above all as particles [7,16]. BTEX and DEG were recorded directly in the whole sample of PFW_s. This choice was necessary because BTEX are partitioned between gas and liquid phases, therefore the particulate matter does not influence their concentration; moreover they are volatile compounds and the filtration procedure causes loss of analytes. DEG was also analyzed in unfiltered sample because it is highly soluble in water, not much volatile and it does not tend toward absorption on particles [17].

Analytical methods by themselves were not able to give information on what happens when organisms are exposed to PFW_s, which concentrations are toxic and which is ecological impact of a PFW discharge. The use of bioassays, together with the classic chemical analyses, can contribute to the understanding of these aspects.

2. MATERIALS AND METHODS

2.1. Sampling and Sample Treatment of Produced Formation Water (PFW)

PFW samples were collected from three different gas platforms situated at about 20 km off the Adriatic coast (Pescara and Rimini, Italy): one of these (PFW1) was collected in October 2005 and the other two (PFW3 and PFW2) in June 2006.

On offshore platforms PFW is stored in a tank which empties when it is full load. All PFW_s were sampled from a tap located on the platform, which receives the PFW after this has had a physical-chemical treatment (depressurization, gravity separation techniques, activated carbon filtration). The physical-chemical parameters of PFW_s (salinity, pH, conductibility, ORP and oxygen dissolved) were measured in laboratory by multi-parameter probe (YSI, mod. 556MPS) (**Table 1**).

For the bioassays, about ten litres of PFW were immediately filtered (Millipore®, 0.45 μm) and refrigerated in polystyrene vessels at 4°C until their execution. The bioassays were carried out in 72 hours.

The PFW_s were stored in different containers according to type of chemical analyses. For the metals two litres were filtered (Millipore®, 0.45 μm), acidified with high purity nitric acid and refrigerated at 4°C until analysis; the filters were stored at -20°C. For BTEX 10 mL of PFW were stored in SPME dark vials (Varian S. p. A); a magnetic stirrer bar was inserted in each vial prior to sealing the vial by magnetic steel closures equipped with Teflon septa. The vials were refrigerated at 4°C and the samples were acidified at pH=2 with HCl and saturated with NaCl. For the PAHs analysis, one litre of PFW was immediately filtered (Millipore®, 0.45 μm) and, together with the filters, stored at 4°C. For the DEG analysis one litre of sample was collected in dark glass bottles, saturated with mercury chloride and refrigerated at 4°C to avoid photochemical and bacterial activity.

2.2. Bioassays

The bioassays were carried out on filtered samples, according to the methods reported in **Table 2** and summarized for each taxon as follows:

Bacteria: Controls and different concentrations for each PFW sampled (dilution ratio 1:2) were tested according to the Basic Protocol [18] and the method ISO [19] with

Table 1. Physical-chemical parameters of production formation water and information on platforms.

PFW	Salinity (PSU)	pH	Conductibility (mS/cm^2)	ORP	Oxygen dissolved (%)	Volume flux of PFW (mc/year)	Platform Installation (year)	Platform distance from coast (Km)	Water depth (m)
PFW1	34	7	51	-100	93	6000	1991	36	116
PFW2	37	7	56	-105	96	3000	1972	15	18
PFW3	37	8	55	-70	86	3000	1991	21	23

SciRes Copyright © 2010

bacteria coming from freeze-dried SDI. PFW salinity was not adjusted prior to testing. The Software Microtox Omni™ v. 1.16 was utilized to calculate the EC_{50} and EC_{20} values (effect concentration of 50% and 20% respectively) and the Dunnett test was used to calculate the NOEC value (no observed effect concentration).

Algae: One control and some concentrations for each PFW sampled were tested according to the ISO method [20] with *Phaeodactylum tricornutum* strain 1090-1° and *Dunaliella tertiolecta* strain 13.86, obtained from the Plant Physiology Institute of Gottingen University (Germany). Algal growth medium was prepared with artificial seawater [20]; for *D. tertiolecta* nutrients, according to the IRSA-CNR method [21] and vitamins according to the ISO method [20] were added. The algal inoculum had an initial density of 10000 cells mL^{-1} ± 10% for *P. tricornutum* and 2000 cells mL^{-1}± 10% for *D. tertiolecta*. Regression analysis technique was performed for the determination of EC_{50} and EC_{20}; the Dunnett test was used to calculate the NOEC value.

Crustaceans: A control and some concentrations for each PFW sampled were tested with nauplii of *Artemia franciscana*, according to the APAT IRSA-CNR method [22], and with nauplii of *Tigriopus fulvus*, according to the ISO/FDIS method [23] as modified by Faraponova *et al.* [24,25]. Reference cysts of *A. franciscana* were obtained from the Quality Assurance Research Division U. S. Environmental Protection Agency (Cincinnati OH 45268, USA) or from the Laboratory for Biological Research in Aquatic Pollution, University of Ghent (Belgium). The eggs of *A. franciscana* were hatched in synthetic seawater and the nauplii were used within 48 hours of hatching [22]. Synchronized nauplii (24-48h) of *T. fulvus* were collected from a culture of two hundred females taken from a mass laboratory culture originated from the Italian coast (Calafuria, Livorno) and supplied with an algal mixture (*Tetroselmis suecica* and *Isochrysis galbana*, ratio 1:2). Probit analysis was performed for the determination of EC_{50} and EC_{15}, the Dunnett test was used to calculate the NOEC value.

Fish: One control and some concentrations for each PFW sampled were tested with juveniles of *Dicentrarchus labrax* (80 days old, length of 3.74±0.28 cm and weight of 0.48±0.08 g), according to the EPA [26] and OECD [27] methods. Organisms were supplied by the hatchery production plant ASA (Rome), stabled in synthetic seawater with salinity of 20±1 PSU for 15 days and fed with granulated food until 24 hours before the test. Probit analysis was performed for the determination of EC_{50} and EC_{15}, the Dunnett test was used to calculate the NOEC value.

The results were compared to a toxicity scale reported in **Table 3**. On the basis of this toxicity scale, the samples were classified as follows: 1) toxic $10 \leq EC_{50} < 100$, $20 \leq EC_{20} < 50$, effect percentage ≥50; 2) weakly toxic $EC_{50} > 100$, $EC_{20} > 50$, 20≤effect percentage<50; 3) no toxic EC_{50} no calculable, $EC_{20} > 100$, effect percentage 20.

2.3. Analysis of Metals

Determination of iron (Fe), copper (Cu), zinc (Zn), lead (Pb), chromium (Cr), manganese (Mn), nickel (Ni), barium (Ba), arsenic (As), cadmium (Cd) and mercury (Hg) was carried on both filtered and particulate samples. The filtered sample was directly analyzed. The metal dissolution of particulate fraction collected on the filters was conducted using microwave-assisted digestion (Milestone MLS Ethos TC) with 3 mL of HNO_3 and 9 mL of HCl. The metal concentrations were determined by a graphite furnace atomic absorption with Zeeman background correction technique (SpectrAA-220Z, Varian) and by coupled emission plasma ICP-OES (Liberty AX, Varian). For Hg analysis a Direct Mercury Analyzer (DMA-80, FKV) instrument was used (EPA Method [28]). All samples were run in triplicate. The quantification limits (LOQ) were: 0.0005 mg/l for Hg and Cd, 0.01 mg/L for the other metals.

2.4. Analysis of Organic Compounds

BTEX: The analyses were extracted and pre-concentrated by means Solid Phase Micro Extraction (SPME) using a stable flex fiber of divinilbenzene-carboxen-poly-dimethylsiloxane (film thickness: 55/30 μm) (Supelco®) by head space sampling. The analytical determinations of BTEX were carried out in unfiltered samples using a modified EPA method [29]. A gas chromatography coupled with mass spectrometry (GC HP 5790 Agilent Technologies® and MS 5973 Network Agilent Technologies®) were used. The method detection limits were 1 μg/L for benzene and 0.1 μg/L for toluene, ethyl benzene and xylenes.

PAHs: The analyses were investigated in filtered samples and on the particulate matter retained by the filter (Millipore®, 0.45 μm). The analyses were extracted by the filtered samples by means Solid Phase Extraction technique. The treatment of filters was carried out by ultrasonic extraction for 20 minutes with 10 mL of dichloromethane. Then, both the extraction phases were evaporated at 1-2 mL with a gentle nitrogen flow. Afterward, 1 mL of toluene was added and the residual dichloromethane was completely removed. All solvents were capillary GC grade supplied by Sigma-Aldrich. The analyses of PAHs were carried out in gas chromatography coupled with mass spectrometry (GC HP 5790® and MS 5973 Network Agilent Technologies). The LOQ was 1 μg/L for each analysis.

DEG: An extraction procedure of DEG was carried out with 2 mL SPE cartridges packed with 200 mg of EN V+stationary phase (International Sorbent Technology,

SciRes Copyright © 2010

Table 2. Experimental conditions of bioassays (*for PFW1 were tested the concentrations: 10-20-40-80%).

	Vibrio fischeri	Phaeodactylum tricornutum	Dunaliella tertiolecta	Artemia franciscana	Tigriopus fulvus	Dicentrarchus labrax
Organisms/ Life stage	cells	unialgal culture	unialgal culture	nauplii 48h	nauplii 48h	juveniles
Strain/origin	commercially available	culture	culture	commercially available	culture	hatchery
Type of test	static	static	static	static	static	static
Time exposure	5-10-15min.	72h	72h	96h	96h	96h
Intensity of lux	Not required	7000	7000	3000-4000	500-1200	500-800
Photoperiod (L:D)	Not required	24:0	24:0	14:10	16:8	16:8
Dilution water/ control	synthetic seawater	synthetic seawater	synthetic seawater	synthetic seawater	synthetic sea-water	synthetic seawater
Salinity (PSU)	35	32	32	35	38	20
Temperature (°C)	15±1	20 ± 2	20 ± 2	25 ± 2	18 ± 2	20 ± 1
pH	8.0 – 8.2	8 ± 0.5	8 ± 0.5	6.5 – 8.5	8.0 ± 0.3	7.5 ± 0.5
Vessel	5mL	100mL	100mL	50 mL	culture plates 12 wells	2000 mL
Volume/well	1mL	25mL	25mL	40mL	3mL	1800mL
N°organisms/well	-	10000/mL	2000/mL	10	10	5
N°of concentrations (Range)	5 (6-11-22-45-90%)	5 (6-12-25-50-100%)*	5 (6-12-25-50-100%)	5 (6-12-25-50-100%)	5 (5-10-20-40-80%)	5 (6-12-25-50-100%)
N°of replicates	3	3	3	3	3-4	3
Feeding during the test	absent	absent	absent	*D. tertiolecta*	absent	absent
Endpoint/Effect	bioluminescence inhibition rate	growth inhibition rate	growth inhibition rate	immobilization rate	mortality rate; moult release rate	mortality rate
Expression of endpoint	EC_{50};EC_{20} NOEC	EC_{50};EC_{20} NOEC	EC_{50};EC_{20} NOEC	EC_{50};EC_{15} NOEC	EC_{50};EC_{15} NOEC	EC_{50};EC_{15} NOEC
Acceptability (effect control)	≤10%	>0.04/h	>0.04/h	≤10%	≤10% (mortality) ≤20% (moult release)	≤10%

Glamorgan, UK). The off-line solid-phase extraction/ pre-concentration technique was followed by a nano-scale flow injection/direct-electron ionization (EI) mass spectrometric analysis. A quadrupole mass spectrometer (Palo Alto, CA) was coupled with a Direct-Electron Ionization (EI) [30-32]. Using this approach, DEG was detected within a concentration of 31 μg/L [33].

Table 3. Toxicity scale used in this paper to classify the toxicity of Production Formation Water (PFW).

Effect (%)	EC50 (%)	EC20 or EC15 (%)	TOXICITY ASSESSMENT
%<20	n.c.	>100	no toxic
20≤%<50	>100	>50	weakly toxic
≥50	10≤%<100	20<%<50	toxic

3. RESULTS

3.1. Bioassays

The results of the eco-toxicological battery are reported in **Table 4**. The three filtered PFW_s resulted toxic according to the overall assessment related to bioassays. The species showed different sensitivity to PFW: the two microalgae and *Artemia franciscana* showed higher values of EC_{50} and EC_{20} (EC_{15}) than the other organisms, indicating weak toxicity. In particular, *Artemia* did not record toxicity for PFW1 (no efficient concentration was calculable). The other crustacean *T. fulvus* showed toxic effects for all PFW_s (PFW2>PFW1≥PFW3) related to both mortality and moult release. The sub-lethal effect was already observed at PFW concentrations that were not causing mortality of nauplii (20-80) %. The fish species *D. labrax* showed a toxic response similar to the one of *T. fulvus*, with a minimum value of EC_{50} equal to 15% and maximum value of 47% as follows: PFW2>PFW1≥

SciRes Copyright © 2010

PFW3. The bacterium *V. fischeri* recorded lower toxicity than *T. fulvus* and *D. labrax* but yet a toxic effect was observed for all PFW_s (PFW1>PFW3≥PFW2).

3.2. Analysis of Metals

In filtered sample, Ba, Mn and Zn showed detectable concentrations. There were not significant differences between PFW2 and PFW3 exclusive of Ba and Mn. These two metals showed higher concentrations of one order in PFW2 than PFW3. In particulate sample, all metals were detectable except Pb and Hg. Ni, Cd and As registered detectable concentrations only in PFW3. Ba, Zn and Fe showed highest concentrations and some significant differences among the PFW_s analyzed. Ba concentration was higher of one order in PFW1 and PFW2 than PFW3; Zn was higher of two orders in PFW2 and PFW3 than PFW1; Fe was higher of one order in PFW3 than PFW1 and PFW2.

3.3. Analysis of Organic Compounds

As reported in introduction section, BTEX and DEG were analysed on unfiltered PFW_s. The analyses of the three platforms pointed out that the volatile organic compounds (BTEX) were detected at very high concentrations by the following ranking: PFW1 (1281.8 μg/L) >PFW3 (66.5 μg/L)>PFW2 (48.0 μg/L) (**Table 6**), showing for PFW1 values almost twenty times higher than ones of PFW2 and PFW3. The DEG showed concentrations ranging from 2400 to 13000 μg/L by the following ranking of the fields: PFW3>PFW2>PFW1 (**Table 6**). PAHs were investigated both in filtered and particulate sample but they were lower than LOQ (1 μg/L) in filtered PFW_s. In particulate sample PAHs showed the trend as follows: PFW1 (150.0 μg/L)>PFW3 (126.0 μg/L)>PFW2 (100.0 μg/L), with values about of the same magnitude order. The congeners with two and three rings recorded the following concentrations: 87 μg/L in PFW1 compared to 150 μg/L of the total PAHs content; 54 μg/L in PFW2 compared to 100 μg/L of total PAHs concentration, and 66 μg/L in PFW3 compared to 126 μg/L of total PAHs. The detected concentrations were of the same order of magnitude for all three PFW investigated.

4. DISCUSSIONS

The bioassays showed that the PFW_s were toxic even if filtered. EC_{50} values ranged between the minimum of 14.8 % and values higher than 100 %. Some of the samples did record no toxicity at the EC_{50} level observed

Table 4. Bioassay results related to three Italian Production Formation Waters and toxicity evaluation according to toxicity scale (n.c. not calculable; n.d. not determined).

Species (time of exposure, end point)	%	PFW1	PFW2	PFW3	PFW1	PFW2	PFW3
Vibrio fischeri (15 min. bioluminescence)	EC_{50}	67 (59-75)	> 90	> 90	toxic	toxic	toxic
	EC_{20}	20(18-23)	29(27-31)	28(25-31)			
	NOEC	-	-	-			
Phaeodactylum tricornutum (72h growth)	EC_{50}	> 80	> 100	> 100	weakly toxic	weakly toxic	weakly toxic
	EC_{20}	> 80	52 (46-58)	68 (24-111)			
	NOEC	40	25	25			
Dunaliella tertiolecta (72h growth)	EC_{50}	> 80	n.d.	n.d	weakly toxic	n. d	n. d.
	EC_{20}	> 80	n.d	n.d			
	NOEC	40	n.d	n.d			
Artemia franciscana (96h immobilization)	EC_{50}	> 100	> 100	> 100	no toxic	weakly toxic	weakly toxic
	EC_{15}	> 100	86 (55-259)	77 (42-462)			
	NOEC	n.c.	50	25			
Tigriopus fulvus (96h mortality)	EC_{50}	29	15	44	toxic	toxic	toxic
	EC_{15}	19	8	29			
	NOEC	10	5	20			
Tigriopus fulvus (96h moult release)	EC_{50}	23	25	77	toxic	toxic	toxic
	EC_{15}	n.c.	n.c.	n.c.			
	NOEC	10	5	10			
Dicentrarchus labrax (96h mortality)	EC_{50}	32 (27-39)	15 (n.c)	47 (n.c)	toxic	toxic	toxic
	EC_{15}	23 (15-28)	11 (n.c)	15 (n.c)			
	NOEC	13	6	6			

SciRes Copyright © 2010

Table 5. Metal concentrations in filtered samples of two Produced Formation Waters, total suspended solids and metal concentrations in particulate samples of Produced Formation Water from three offshore gas platforms in the Adriatic Sea (Italy).

Parameters	Unit	PFW2	PFW3	PFW1	PFW2	PFW3
		FILTERED			PARTICULATE	
Total suspended solid	mg			177.42	367.05	398.10
Ba	mg/L	1.63	0.13	309.65	237.75	13.50
Cr	mg/L	<0.01	<0.01	0.12	1.34	0.45
Cu	mg/L	<0.01	<0.01	0.05	0.55	0.42
Mn	mg/L	0.34	0.04	0.84	1.05	0.77
Ni	mg/L	<0.01	<0.01	0.07	<0.01	0.35
Pb	mg/L	<0.01	<0.01	<0.01	<0.01	<0.01
Zn	mg/L	0.18	0.37	0.14	61.92	59.77
Cd	mg/L	<0.0005	<0.0005	<0.0005	<0.0005	0.62
Fe	mg/L	<0.10	<0.10	242.40	775.70	1335.00
As	mg/L	<0.01	<0.01	0.01	<0.01	9.25
Hg	mg/L	<0.0005	<0.0005	<0.0005	<0.0005	<0.0005

Table 6. Organic compound concentrations in Produced Formation Water (PFW) samples from three offshore gas platforms in the Adriatic Sea (Italy).

Analytes		PFW1 (µg/L)	PFW2 (µg/L)	PFW3 (µg/L)
BTEX (unfiltered sample)	Benzene	256.0	10.4	20.4
	Toluene	50.6	14.1	12.1
	Ethyllbenzene	115.2	7.7	13.8
	Xilenes (o,m,p-xylene)	860.0	14.8	20.2
	BTEX	1281.8	47.0	66.5
DEG (unfiltered sample)	Diethylene glycol	2400	9600	13000
PAHs (particulate sample)	Naphtalene	14	8	11
	Acenaphtylene	21	15	17
	Acenaphthene	19	15	15
	Fluorene	16	4	6
	Phenanthrene	13	8	10
	Anthracene	4	4	7
	Fluorantrene	12	10	12
	Pyrene	10	7	10
	Benzo(a)anthracene	8	4	7
	Crysene	5	6	7
	Benzo(b)fluorantene	6	4	4
	Benzo(k)fluorantene	6	5	6
	Benzo(a)pyrene	5	3	3
	Dibenzo(a,h)anthracene	4	4	4
	Benzo(g,h,i)perylene	4	3	4
	Indenopyrene	3	< 1	3
	PAHs 2- 3 ring congeners	87	54	66
	PAHs	150	100	126

butdid show evidence of a toxic response at the EC_{20} level. The EC_{50} data lied within or were higher than the range (5.54-20.73%) previously reported for another filtered PFW originated from an Italian gas platform and assayed by bacteria and sea urchins [14]. Ours EC_{50} data also were higher than values related to unfiltered PFW_s coming from the North Sea platforms [4-8]. This shows that the filtered samples have generally lower toxicity than the untreated samples.

The difference of sensitivity among the species has been quite remarkable: *T. fulvus* and *D. labrax* showed the highest toxicity (EC_{50}<50%), followed by *V. fischeri* (EC_{20}<30%). *Artemia* and the two algae did not record significant toxic effect (EC_{20}>50%).

SciRes Copyright © 2010

In addition to the toxicity assessment, we analyzed chemically PFW (metals, BTEX, PAHs and DEG). Appreciable concentrations of Ba, Mn and Zn were recorded in filtered samples while also high quantities of Fe were registered in particulate samples. Ba is probably related to drilling fluid residuals of PFW [7], Zn may be derived from corrosion or chipping of galvanized structures on the platform or in the oil/water separator system [34] and Fe could have natural origin or derive from corrosive events. The lower weight aromatic hydrocarbons (BTEX) were found by significant concentrations in liquid phase, while the PAHs were recorded only on particulate samples. DEG concentrations also were of milligram order in liquid phase but very low compared to the threshold of 3500 mg/L imposed by the PFW discharge authorization decrees issued by the Italian Ministry of the Environment.

An integrated evaluation of the eco-toxicological and chemical results showed that test-organisms were especially sensitive when exposed to PFW_s containing Ba, Mn, Zn and BTEX. *T. fulvus* and *D. labrax* showed the highest toxicity in PFW2 containing high concentrations of Ba, Mn and Zn. *V. fischeri* showed the highest toxic effect in PFW1 that recorded the highest quantities of BTEX. Nobody among the test-organisms indicated a preference for PFW3 containing the highest value of DEG. Moreover, DEG is not toxic alone but could determine co-solvent effects with other chemical compounds [35].

5. CONCLUSIONS

Our results indicate that a filtration treatment might diminish PFW toxicity. If a similar treatment was carried out on the platform before the PFW discharge, the ecological risk associated to the discharge would be probably reduced.

Besides, the results confirm the different sensitivity of test-organisms belonging to different trophic levels. Because PFW chemical composition is so variable for type and concentration of contaminants, test-organisms that are tolerant to a type of PFW could be sensitive to others. For this reason, we think that it is not correct to establish a single species to investigate the PFW_s but a battery of species should always be applied in order to have integrated responses.

6. ACKNOWLEDGEMENTS

The present work was funded by the Italian Ministry of Environment, Land and Sea. We thank Lucio Lattanzi for analysis of BTEX and PAHs, Achille Cappiello and Giorgio Famiglini for DEG analysis, Manuela Dattolo, Silvia Mariotti and Antonella Cozzolino for metal analysis. The authors acknowledge B. Trabucco for constructive comments. We thank the Aquaculture Plant Nuovo Azzurro (Civitavecchia, Roma-Italy) for providing the larvae of *Dicentrarchus labrax*.

REFERENCES

[1] Trefry, J.H., Naito, K.L., Trocine, R.P. and Metz, S. (1995) Distribution and bioaccumulation of heavy metals from produced water discharges to the Gulf of Mexico. *Water Science Technology*, **32,** 2, 31-36.

[2] Decree of Environmental Ministry 190 of July 28 (1994) G. U. n. 190 16/08/1994.

[3] Brendehaugh, J., Johnsen, S., Bryne, K.H., Gjose, A.L., Eide, T.H. and Aamot, E. (1992) Toxicity testing and chemical characterization of produced water: A preliminary study. In: Ray, J.P. and Engelhart, F.R. Eds, *Produced Water Technological/Environmental Issues and Solutions*, Plenum Press, New York, 245-256.

[4] Schiff, K.C., Reish, D.J., Anderson, J.W. and Bay, S.M. (1992) A comparative evaluation of produced water toxicity. In: Ray, J.P. and Engelhart, F.R. Eds, *Produced Water Technological/Environmental Issues and Solutions*, Plenum Press, New York, 199-208.

[5] Sommerville, H.J., Bennett, D., Davenport, J.N., Holt, M.S., Lynes, A. and Mahieau, A. (1987) Environmental effect of produced water from North Sea oil operations. *Marine Pollution Bulletin*, **18,** 549-558.

[6] Stephenson, M.T. (1992) A survey of produced water studies. In: Reed, M. and Johnsen, S. Eds. *Produced Water* 2 *Environmental Issues and Mitigation Technologies*, Plenum Press, New York, 1-11.

[7] Stromgren, T., Sorstrom, S.E., Schou, L., Kaarstad, I., Aunaas, T. and Brakstad, O.G. (1995) Acute toxic effects of produced water in relation to chemical composition and dispersion. *Marine Environmental Research*, **40,** 147-169.

[8] Utvik, T.I.R. (1999) Chemical characterization of produced water from four offshore oil production platforms in the North Sea. *Chemosphere*, **39,** 15, 2593-2606.

[9] Scott, K.A., Yeats, P., Wohlgeschaffen, G., Dalziel, J., Niven, S. and Lee, K. (2007) Precipitation of heavy metals in produced water: Influence on contaminant transport and toxicity. *Marine Environmental Research*, **63,** 146-167.

[10] Cicero, A.M., Di Mento, R., Gabellini, M., Maggi, C., Trabucco, B., Astorri, M. and Ferraro, M. (2003) Monitoring of environmental impact resulting from offshore oil and gas installations in the Adriatic Sea: Preliminary evaluations. *Annali di Chimica*, **93,** 701-705.

[11] Maggi, C., Trabucco, B., Mannozzi, M., Di Mento, R., Gabellino, M., Manfra, L., Nonnis, O., Virno Lamberti, C. and Cicero, A.M. (2007) A methodological approach to study the environmental impact of oil and gas offshore platforms. *Rapp. Comm. Int. Mer Médit.*, **38**.

[12] Mariani, L., Manfra, L., Maggi, C., Savorelli, F., Di Mento, R. and Cicero, A.M. (2004) Produced formation waters: A preliminary study on chemical characterization and acute toxicity by using fish larve Dicentrarcus labrax L., 1758. *Fresenius Environmental Bulletin*, **13,** 1427-1432.

[13] Faraponova, O., Onorati, F., Magaletti, E. and Virno Lamberti, C. (2007a) Sensitivity of Tigriopus fulvus (Copepoda, Harpacticoida) towards diethilene glycol (DEG) and produced formation water (PFW). *International Meiofauna Conference-Recife*, Brazil, **89**.

[14] Manfra, L., Moltedo, G., Virno Lamberti, C., Maggi, C., Finora, M.G., Gabellino, M., Giuliani, S., Onorati, F., Di

SciRes Copyright © 2010

Mento, R. and Cicero A.M. (2007) Metal content and toxicity of produced formation water (PFW): Study of the possible effects of the discharge on marine environment. *Archives of Environmental Contamination and Toxicology*, **53,** 183-190.

[15] Manfra, L., De Nicola, E., Maggi, C., Zambianchi, E., Caramello, D., Toscano, A., Cianelli, D. and Cicero, A.M. Submitted Exposure of rotifers, crustaceans and sea urchins to produced formation water and seawaters collected in a gas platform area. *Journal of the Marine Biological Association*.

[16] Prego, R., Cottè, M.H., Cobelo Garcìa, A. and Martin, J.M. (2006) Trace metals in the water column of the Vigo Ria: Offshore exchange in mid-winter conditions. *Estuarine Costal and Shelf Science*, **68,** 289-296.

[17] Weyerhaeuser (2005) Material safety data sheet MSDS WC 379-01 Rev. 8/26/2005, 1-7.

[18] Azur Environmental (1995) Microtox® acute toxicity basic test procedures, **63**.

[19] ISO (2004) Water quality: Determination of the inhibitory effect of water samples on the light emission of Vibrio fischeri (luminescent bacteria test)-Part 3: Method using freeze-dried bacteria. ISO/CD, 11348-3.

[20] ISO (2006) Water quality: Marine algal growth inhibition test with Skeletonema costatum and Phaeodactylum tricornutum. Reference number ISO 10253:2006, **12**.

[21] IRSA (1978) Metodologia di saggio algale per lo studio di acque marine. *Quaderni dell'Istituto di Ricerca sulle Acque*, IRSA-CNR, Milano, **39**.

[22] APAT-IRSA-CNR (2003) Metodo 8060. Metodo di valutazione della tossicità acuta con Artemia sp. In: APAT-IRSA-CNR, Metodi analitici per le acque, Manuali e Linee Guida 29/2003, Volume Terzo, 1043-1049.

[23] ISO/FDIS (1998) Water quality: Determination of acute lethal toxicity to marine copepods (Copepoda, Crustacea). ISO/FDIS, **16,** 14669.

[24] Faraponova, O., De Pascale, D., Onorati, F. and Finoia, M.G. (2005) Tigriopus fulvus (Copepoda, Harpacticoda) as a target species in biological assays. *Meiofauna Marina*, **14,** 91-95.

[25] Faraponova, O., Virno Lamberti, C. and Onorati, F. (2007b) Study intensification of Tigriopus fulvus (Copepoda, Harpacticoida) as a target species in bioassays. *International Meiofauna Conference-ecife*, Brazil, **90**.

[26] EPA (1993) Methods for measuring the acute toxicity of effluents and receiving waters to freshwaters and marine organisms. EPA/600/4-90/027F, *Environmental Protection Agency*, Cincinnati, Ohio, 71-91.

[27] OECD (1992) Guideline for testing of chemicals n° 203. *Fish, Acute Toxicity Test*, 1-9.

[28] EPA (1998) Mercury in solids and solutions by thermal decomposition, amalgamation, and atomic absorption spectrophotometry Method 7473. *Environmental Protection Agency*, Cincinnati, Ohio.

[29] EPA (1996) Volatile organic compounds by gas chromatography/mass spectrometry (GC/MS) Method 8260B (Revision 2). *Environmental Protection Agency*, Cincinnati, Ohio.

[30] Cappiello, A., Famiglini, G., Mangani, F. and Palma, P. (2001) New trends in the application of electron ionization to liquid chromatography-mass spectrometry interfacing. *Mass Spectrom. Rev.*, **20,** 88-104.

[31] Cappiello, A., Famiglini, G., Mangani, F. and Palma, P. (2002) A simple approach for coupling liquid chromatography and electron ionization mass spectrometry. *J. Am. Soc. Mass. Spectrom.*, **13,** 265-273.

[32] Cappiello, A., Famiglini, G. and Palma, P. (2003) Electron ionization for LC/MS. *Analytical Chemistry*, 75, 497A-503A.

[33] Cappiello, A., Famiglini, G., Palma, P., Pierini, E., Trufelli, H., Maggi, C., Manfra, L. and Mannozzi, M. (2007) Application of nano-FIA-Direct-EI-MS to determine diethylene glycol in produced formation water discharges and seawater samples. *Chemosphere*, **69,** 554-560.

[34] Neff, J.M., Sauer, T.C. and Maciolek, N. (1992) Composition, fate and effects of produced water discharges to nearshore marine waters. In: Ray J.P. and Engelhart F.R. Eds, *Produced Water Technological/Environmental Issues and Solutions*, Plenum Press, New York, 371-385.

[35] Sorensen, J.A., Gallagher, J.R., Hawthorne, S.B. and Aulich, T.R. (2000) *Gas Industry Groundwater Research Program*, Final Report for U.S. Department of Energy National Energy Technology Laboratory Cooperative Agreement No. DE-FC26-98FT40321; Energy & Environmental Research Center Publication 2004-EERC-07-01, Grand Forks, ND.

SciRes Copyright © 2010

Vol.2, No.1, 41-48 (2010)
doi:10.4236/ns.2010.21006

Natural Science

Review on nano-drugs

Yong Liu[1,3], Tian-Shui Niu[2], Long Zhang[1], Jian-She Yang[1,2]

[1]Key Laboratory for Natural Medicine, Lanzhou Institute of Chemical Physics, Chinese Academy of Sciences, Lanzhou, China
[2]China Life Science College of Northwest Normal University, Lanzhou, China
[3]Graduate School of Chinese Academy of Sciences, Beijing, China

Received 25 September 2009; revised 20 October 2009; accepted 22 October 2009.

ABSTRACT

Nano materials is a new type of drug carriers with very promising application. In recent years, great progress was achieved in making drugs own the characteristics of targeted and controlled release via nanotechnologies. This paper addressed the capability of nano drugs on targeting to cells, penetrating through epicyte, controlled release and the security issues resulting from its using. We gave the prospect of nano drugs in biology and medicine applying.

Keywords: Nano Drug; Targeting; Cell Penetration; Controlled Release

1. INTRODUCTION

Nano drug is an important product of the rapidly developing nanotechnologies in biology and medicine field [1]. Drug is wraped in or adsorbed on surface of nanoparticles, when the specific targeting molecules combining with the receptor of cell surface, nano-drug is taken into cells, to achieve the safe and effective targeted drug delivery and gene therapy. Because Nano-drug carriers have high targeting, favorable sustained, controlled release capability and superior cell penetration ability, it can improve efficacy of drugs and reduce side effects. It is the production of nano-technology combining with modern medicine [2-3].

There are three main types of drug-loaded nanoparticles at the present time. First, the common drug-loaded particles: according to pharmacy technology bind with nanotechnology, with special methods to make the drug that physical-chemical property are unsteady and easy to be degradated or has considerable bad reaction to impact on the use highly dispersed in the drug carrier. Second, the controlled-release drug-loaded particles: be different from routine drug-loaded particles, this kind of drug's release process of nano-particles have a specific law. The dissolution of sac wall and the role of micro-organisms could make the drug in the heart of sac spread out. According to different purposes, choose a suitable timber and technology to make particles gather on the local tissue and attaine effective concentration, without causing general toxicity reaction. Third, the targeting drug-loaded particles: according to the needs of clinical, choose different carriers that have different affinity to different organizations or diseased region to make different carrier particles, or combine monoclonal antibody with the carrier, or under the effect of external magnetic field so that the drug can be transported to the particular site that we expected. Because nano-technology has changed the physical space of the drug, physical-chemical and biological property of drugs has surprising change. The changes mainly include the following aspects [2-7]: 1) Nanoscale drug carriers can enter into the capillaries, and freely flow in the blood circulation. It also can go through cells, be absorbed though pinocytosis by histiocyte and enhance bio-availability of drug; 2) Because the specific surface area of nano-drug carriers is very high, solubility of poor water-soluble drugs in the nano-carrier is relative enhanced and overcome the problems preparation with conventional methods; 3) Nano-carriers can be made to targeted position system, decrease the dose of drug and reduce the side effects with special processing. 4) By controlling the degradable speed of polymers in vivo, Nano-carriers can extend biological half-life of drug, improve the efficacy of the short-half-life drugs and reduce side effects of medication. 5) Because of Eliminateing the limit of specifial barriers such as blood-brain barrier, blood-ocular barrier and cell membrane barrier to the drug, nano-particulate drug carriers can pass through these barriers to treat scathing sites.

The central principle of nano-drug carrier is to realize drugs delivery "effective, safe and controllable". Therefore, targeting, controlled release and safety of drugs is an important and topical issues in pharmacy researchful area. The emergence of nano-delivery system make feasible to realize targeting and controlling release of drug. This paper expounds nano-drug delivery research in the field of medicine around the core.

2. THE TARGETING OF NANO-DRUG

Nano-drugs can selective distribute the object, to en-

SciRes Copyright © 2010

hance efficacy and reduce side effects. The role of the object from the target organ, target cell to the most advanced structure in the target cells. The three levels method of targeted therapy all could complete with nanotechnology. Nano-targeting drugs can be divided into passive targeting and active targeting.

2.1. Passive Targeting

Studies found that small particle size passive targeting drugs can spontaneously gather the diseased region making use of EPR (Enhanced Permeability and Retention) to achieve the purpose of passive targeting [8]. Because the blood capillary's permeability of the damage spot which caused by tumor, inflammation, hypertension and so on is higher than that of the normal blood vessel, simultaneous discharge capacity of lymph blood vessel is weaken. So in vivo long circulation the biological compatible macro-molecule, the medicine carrier, the molecular assembly are easier through blood vessel that injuries portion into the organization and assemble. The EPR is special useful to treat the tumor and blocks [9]. One of the ways to enhance EPR is strengthening the stability of drug to lengthen circulation time of drug in vivo. So the drug carriers have more opportunities to go through the target position and get together [10]. The passive targeting preparation include of micro-capsule, microsphere, nanopartiele，liposome and so on. The liquid crystal, fluid film, lipin, lipoid, protein and biodegradation high polymer material is often used as carrier material.

Mitra [11] studied the tumor targeting using dextran-doxorubicin-chitosan nanoparticles and showed that nanoparticles was not only reducing peripheral side effects, but also greatly improving the treatment of solid tumors. Du, *et al*. [12] made the carrier complex system with cyclic arginine-glycine-aspartic acid and lipid and combined interferon-α1b to treat liver fibrosis in rats, showed that according to combine with carrier， the concentration of interferon-α1b in the liver of rats was up to 10 times and the degree of liver fibrosis was significantly reduced comparing with non-carrier group. This illustrated the complex vector had a clear targeting to the liver. Briz [13-15] made two kinds of chelate compound with bile acid glycine-cisplatin and ursodeoxycholic acid-cisplatin, through the result of in vivo experiments showed that two complexes had a good affinity to the tumor cells of liver, and the absorbed dose was obvious higher than the original drug. Because of lower toxicity, these chelate compounds can extend more survival time of mice tumor transplant than the original drug. They also had effect to the chemical sproof tumor cells, and partly decrease physiological tolerance of tumor to the cisplatin.

2.2. Active Targeting

Active targeting is that drug carriers through the surface of nano-ligand binding specificity of targeting delivers drugs to specific organizations or release drugs in vivo under the certain physical conditions. The conventional active targeting mechanisms include three kinds. First, thermal-sensitive and pH-sensitive targeting, that is, sufficiently use the changes of temperature and acidity that different body tissues and organs in the pathological process. Choose the polymer containing thermo-sensitive or pH-sensitive (such as N-isopropylacrylamide, etc.) component to form the polymer micelle. Drug-loaded micelles in the specific temperature or acidity can be easily depolymerized and released the drugs [16-18]. Thomas [19] reported a new type of temperature-sensitive nanoparticles. The critical solution temperature is 30℃. The drug was wraped in the nanoparticles and the slow releaseing could last one month in vitro. When the temperature was more than 37℃, the nanoparticles could priority be uptaken by the MDA2MB2231 breast cancer cells. This temperature-sensitive nanoparticles has great potential in the the treatment of thermal sensitivity targeting to the solid tumors.

Na [20] made PA-SDM nanoparticle with the amylopectin acetate (PA) and sulfanilamidesulfamidyl (SDM) that loadding adriamycin (ADR). The nanoparticles could change the rate of ADR release along with the alkalinity acidity change. As the pH value of the tumor spot was different from that of normal tissue, PA-SDM nanoparticles could selectively accumulate on the breast cancer cells MCF-7 and speed up the release, enhanced cytotoxicity to the tumour.

Yoo [21] got the pH-sensitive polymer micelles complex by linking ADR with acid-sensitive. Taking advantage of meta-acid physiological characteristic of the tumor organization partial micro environment, adriamycin hydrolysis from the polymer micelles down when the drugs reached to the tumor site. Thereby enhanced the concentration of ADR in the tumor cells and increased efficacy of the drug.

These belong to the studies of the targeted drug delivery that in response to the environment, when the drug carriers meet with environmental stimulative, they are depolymerized to the monomers and drugs releases out of the vector. When combine EPR effect, nano-drug carriers that environment respond can further enhance the efficacy of antineoplastic.

Secondly, drug carriers can be modifed by combining with special targeting ligand (antibodies, lectins, sugars, hormones, etc.). Thereafter, this carrier-ligand complexity can be specifically identified by the epicyte receptors and accurately transmitted to the target spot.

Xiao [22] made the starch nanoparticles (StNP) charged negative electricity with reverse microemulsion and cross-linking methods, after StNP was modificed by a folic acid active substances (FA-PEG-NH_2) modification, they successfully prepared the folic acid-starch

SciRes Copyright © 2010

nanoparticles (FA-PEG/StNP) which the average diameter was about 130 nm. FA-PEG/StNP was combined with the anti-cancer drug doxorubicin (DOX) through penetration and got nano-drug containing folic acid-starch. Compared with StNP through hepatoma cells (BEL7404) culture experiments found that the cell lethality of using FA-PEG/StNP carrier was 3 times higher than that of StNP carrier. The result proved that FA was modified on the particles can significantly increased the particle targetting to the liver targeting cancer cells, made more drugs actting on the tumor cells and enhanced the drug's effect.

Jie [23] synthesized nanoparticles (NPs) of the blend of a component copolymer for targeted chemotherapy with paclitaxel used as model drug. The component was poly (lactide)-D-a-tocopheryl polyethylene glycol succinate (PLA-TPGS), which was of desired hydrophobic-lipophilic balance, which facilitates the folate conjugation for targeting. The nanoparticles were decorated by folate. The drugs were evidently promoted to targeting gather the surface of the breast cancer cells (MCF-7) and C6 glioma cells, thereby enhancing its efficacy.

Terada [24] established the specific targetting drug delivery system to the human hepatoma cell line (HCC). Through amino of dioleoyl phosphatidylethanolamine (DOPE) linked to substrate peptide of peginterferon matrix metalloproteinase-2 that was modified by PEG and obtained PEG-PD, which could be enzymed cut by matrix metalloproteinase-2, then integrated the PEG-PD into the galactose-liposome and got the GaL-PEG-PD-liposomes. Because the steric effect caused by PEG shielding the galactosyl of the surface of liposome complex, GaL-PEG-PD-liposomes could not be uptaken by the normal liver cells. But there was has high concentration of secreted matrix metalloproteinase-2 around the HCC cells and could hydrolysis the peptide of Gal-PEG-PD-liposomes to remove the polyethylene glycol, relief the steric effects of polyethylene glycol, exposure the galactose residues of liposome surface. At this time the liposome could be recognised and uptaken by HCC cells and got the purpose of specific targeting to HCC cells.

Thirdly, suitable adjuvant was encapsulated into the micelles with physical method. The micellar will pulse release drug under the influence of the external excitation conditions (such as IR light, magnetic field). The adjuvant does not affect performance of micelles (stability, permeability, etc.), but impact the performance of the drug that is wrapped up in micellars (under certain conditions, hydrophilic can be converted to lipophilic, etc.). For example, Sershen [25] prepared N-isopropylacrylamide hydrogel could encapsulate γ-Fe2O3. Under the effect of outside magnetic field, when the temperature of hydrogel rised 10 ℃ and is higher than the critical solution temperature, hydrogel will rupture and sudden release the drugs.

Nanoparticles interacte with electromagnetic pulse or ultrasonic pulse can also enhance the release of drug. When the nanoparticles reach to the tumor vascular system and was adsorbed to the vessel wall, because electromagnetic pulse or ultrasonic pulse lead to the local thermal effects and further caused cavitation, tumor cell membrane is perforated, large molecular drugs enter into the cancer cells from blood, play the therapeutic effect.

3. CELL PENETRABILITY OF NANO-DRUG

There are many natural biological barriers to prevent the body suffering damage, such as blood brain barrier, blood-eye barrier, biomembrane barrier and so on, but the existence of these barriers also gives the difficulty to the treatment of morbidity spot. Nanoparticles is solid colloid particles that composed of macromolecule substance and the particlesize is 1~1000nm. It can pass various barriers. But as drug-carrier, if it can use its cell penetration and carries bioactive molecules into the targeting cell is the key problem of drug playing curative effect. In order to solve this problem, the researchers tested many sorts of nanomaterials. Yue [26] prepared nanometer sized-liposome that was produced from phosphatidylcholine to encapsulate fluorescent dyes 10^{-6} fluorescein isothiocyanate ihydrochloride (FITC), 10^{-6} Rhodamine B (RhoB). Liposome and fluorescent dyes was put into culture medium. After 2h, the result of confocal microscope screen showed that the FITC and Rho B couldn't go through cell membranes, fluorescence didn't exist in the cell, but green and red fluorescence were obserived in the liposomes groups. This explained that nano-liposomes could go into cell by cell endocytosis or fusion process, transfer fluorescent reagent that couldn't through membrane into cells. When the FITC-liposomes and liposomes Rho B coacted on cell, yellow fluorescence exited in cell, this account for liposomes containing different substances could into the cell at the same time.

According to Sivararnakrishnan [27] report, Betamethasone 17-valerat (BMV)-SIM had a good stability compared to traditional drug emulsion and skin absorption increased. In recycling experiments, the drug dose of skin containing was above 75%.

Ding [28] prepared monostearin solid lipid nanoparticles (MSIN), investigated the cellular uptake of MSIN and the influence on the cellular uptake by MSIN modified with PEG2000 in human-type Ⅱ cell alveolar epithelial cell line (A549) and murine macrophages cell line ($J774A_1$). Rhodamine was incorporated into solid lipid nanopartides as fluorescent marker. The experimental results showed MSIN that was modified with PEG2000 had low toxicity to cell and had good physiological compatibility. It was also highly taken by A549 cell line

SciRes Copyright © 2010

and could be fast reached to saturation. Pantarotto [29] prepared single walled carbon nanotubes modified by derivatization and single walled carbon nanotubes coupling peptides. They were all marked by FITC. Investigated the cellular uptake of the two-type functionalized carbon nanotubes (f2CNTs) and found that they all could penetrate the cell membrane: CNT1 mainly entered into the cytoplasm and the CNT2 that was modified by peptide could enter into the nucleus.

The studies also found that nano-materials that were uptaken by cells have the size critical point. Becker [30] prepared DNA-wrapped single-walled cabon and investigated length-dependent cellular uptaken of these carbon nanotubes. Studies showed that the cellular uptake of carbon nanotubes had a choice of lengths and the cut-off point was (180±17) nm. They speculated that different cell might have different selective range of length to uptake the carbon nanotubes. Ito [31] used carbon nanotubes as EPO (erythropoietin, EPO) oral agent vector and found that the short carbon nanotubes could be used to carry more EPO to the target cells approved the speculation of Becker.

4. THE CONTROLLABILITY OF NANO-DRUGS

Nano-drug interactions with nano-carrier and made to be the controlled-release formulations with appropriate methods. When drug-carrier complex enter into the body, the drug is slowly released out of nanoparticles at the constant speed automatic in the scheduled time through the leaching, infiltration and proliferation or dissolution and act on the specific organ, tissue and cell. In addition, the nano-carriers prevent drug be degraded by various enzyme, extends the effective time of drugs. At the same time this controlled-release nano-drug can reduce the peak phenomenon of blood concentration, reduce side effects and improve efficacy. Mainly through diffusion control, chemical control, solvent control and other methods to achieve the purpose of controlled release of drug. Generally speaking, a controlled-release preparation has two or more controlled-release mechanisms.

4.1. Diffusion-Controlled Release

Drugs or other biologically active substances are combined with carriers; the drug is released in a certain of time and at a certain rate to the environment through diffusion. Diffusion-controlled is the most common mechanism in the controlled-release of drug delivery system, especially the nondegradable polymers carriers; the drug is mainly through this way released. In a biodegradable polymer carriers, when material degradation rate is slower than the diffusion of drug, diffusion of the drug still play a leading role in the release. There are many factors impact the diffusion-controlled release, such as geometric designs of system, condition and quality of ambient medium, the character and structure of the host materials, the solubility and loading amount of the drug [32].

4.2. Chemical-Controlled Release

Through hydrolysis, zymohydrolysis and other chemical reactions, chemical-controlled release system control the rate of drug release. According to the role of drug and substrate, mechanism of release, Chemical controlled system can be divided into degradable system and side-chain system. 1) Degradable system: the biological activity drugs is embedded or dispersed in biodegradable polymer, but there is no chemical bonding effects between drug and polymer, the rate of drug release is controlled by the rate of polymer degradation and erosion. The material of drug carrier is mainly include of biodegradable poly vinegar (such as polylactic acid, polycaprolactone with vinegar), poly polysaccharide (such as chitosan, gelatin), and so on. These materials is nontoxic, and the ultimate metabolites can be discharged in vitro or absorbed by organism, through regulating the rate of polymer degradation or dissolution to controll the release of drug on a specific location within regular hour. In these systems, the rate of polymer degradation or dissolution mainly influence the rate of drug's release, but the speed of degradation or dissolution also has an important relationship with the quality of the polymer (such as polymer molecular weight, crystallinity, the hydrophilic property and hydrophobicity, etc.), many researchers controlled and regulated the rate of degradation or dissolution material with chemical or physical methods such as reshaping, modification, blending to the polymer, further regulate the speed of drug release. But the nature of drug is also an important factor of the drug's release [33]. 2) The side-chain system of drug carrier may be degradable type or nondegradable type. Through the chemical bond that can be hydrolyzed or enzymolied, drugs in the side-chain system can be connected to the primary chain or side chain (side chain can be used to change the drug's release rate) of polymer. The release of drug is controllied through hydrolysis or enzymolysis.

Qing [34] used bovine serum albumin (BSA) as the model drug, at first, the nanoparticles containing proteins were obtained by absorbing BSA from the solution onto the surface of nano-scale SiO2, then, PLGA microsphere loading the solid nanoparticles were fabricated with the solid-in-oil-in-water-emulsion method. Study found with the increasing of the mass fraction of BSA in the product of adsorption, the rate of solvent controlled release of BSA is faster. The main mechanism of drug release is the diffusion of drugs and the degradation of the polymer. In the release process, the BSA that was on the surface of microspheres was first diffused and

SciRes Copyright © 2010

formed pores. It was conducive to the diffusion of the BSA in the inner layer. Water also could go into the microspheres and resulted in the degradation of microspheres. Microspheres that loaded more drugs diffused more BSA in the early period and also the pores that formed were more and larger, the degradation of the microspheres is faster in the late period, so release of BSA was faster.

Yang [35] prepared microspheres that containing antiphthisic drug Rifampin was prepared from poly lactic-co-glycolic acid (PLGA) as carrier by emulsion and solvent evaporation method. In vitro experiment of release, investigated the performance of PLGA microspheres that was as a carrier of drug delivery. The release time of rifampicin in the PLGA microspheres was more than 30 days, and there was no obvious phenomenon of sudden release. But the release of the mass fraction of rifampicin without microspheroidization was up to 96% in 10 minutes. At the same time, they found PLGA molecular weight and the LLA / GA mass ratio had significant impact on the time of the release [36,37]. Because the rate of degradation of low molecular weight PLGA was significantly higher than that of high molecular weight and in the PLGA copolymer, with the GA mass increaseing, hydrophilicity of PLGA enhanced, the degradation significantly speed up. While the rate of the drug's release was mainly controlled by the degradable rate, so with the reducing of PLGA molecular weight and LLA/GA mass ratio, the release of rifampicin speed up. The drug release was simultaneously controlled by drug-diffusion and degradation of carrier material, but in this system, degradation played a decisive role in the mechanism of control. Observed the surface morphology of the degradation rifampicin-PLGA microspheres, they found the surface and inside of microspheres appeared large holes, spherical shape almost disappeared, the red faded and turned to white. These result showed that in early period the drug's release was out of carrier materials only through the drug's diffusion and dissolution, with the drug release time prolonging, the mass fraction of the unit of drugs in microspheres reduced, lead to the release rate of drug that diffusion and degradation decrease, however, with the carrier material degrading and the rate of degradation speeding up, the primarily release of drug was degradation of materials, and made up the rate of diffusion and dissolution release reducing, eventually led to the drug in microsphere carrier was release in a constant velocity.

Solvent-control include of infiltration and swelling mechanisms. 1) The release of solvent infiltration controlled. It accord to the penetration principle of semipermeable membrane. Soluble drug is wrapped in polymer, when it is added in environmental media, the external solvent go into polymer matrix by infiltration and forms saturated solution and then under the action of osmotic pressure between saturated solution and environmental media to release drugs outside. 2) Matrix solvent control, the more common mechanism is swelling. The controlled-release mechanism is using solvent penetration to makes polymer swelling and achieve the purpose of release. At the beginning, solvent penetrate into polymer matrix and cause to swelling, the polymer glass transition temperature to the environment, and chemical chain get slack, so that drugs can be released. Solvation process often contains the spread process of drugs at the same time.

The release of drug is affected by many factors and conditions, including nature of polymer and drugs, temperature of environment, pH value of medium and so on. The change of one factor or condition will affect the controlled mechanism of drug's release. For example, changing the hydrophilicity and hydrophobicity of degradable polymer not only affect the rate of degradation of materials, but also affect swelling and permeability of the material, further affect the release of drugs.

Wang [38] prepared self-assembled nanomicelle of N-acylcholesteryl succinate-O-carboxymethyl chitosan, paclitaxel was used as a model drug. In vitro experiment, they found that release rate of paclitaxel in nano-CCMC micelle was closely related with the pH value. For example the rate of release is low when the pH value of PBS was equal to 7.2, but when pH value was equal to 4.0 or 9.0, the release rate increased. Because CCMC molecules were a new type of polymer ampholyte and containing much free-NH2 and-COOH, the isoelectric point was about 7.14 by the turbidity method detection [39]. In meta-acid or alkaline solution, the free-NH_2 or-COOH in CCMC molecules was ionized to -NH^{+3} or-COO^-. Under the action of charges with the same electrical sign repel each other; the gel network structure of self-assembled nano-micelles (CCMC) fully absorbed water, increased permeability of paclitaxel, accelerated the release rate.

5. THE SAFETY OF NANO-DRUG

Accordance to the interpretation of ISO meeting [40]: biocompatibility means that the capability that the lives tissue has a reaction to inactive materials. Generally refers to the compatibility between materials and host, including histocompatibility and blood compatibility. Nano-bio-medical materials not only has the long-term stable physical and mechanical properties in the biological conditions, but also has side effect to the organization, blood, immune system, etc, that is, non-toxic, tissue compatibility, blood compatibility and so on. At the same time biocompatibility is generally considered to have two major principles, one is the principle of 'biosafety' and the second is the principle of 'biofunctionality' (or the effect of promoting the function to the body). Nano-biological materials are a foreign body for

SciRes Copyright © 2010

the host, so there will be some sort of response or repulsive phenomenon in the body. If nano-biological materials could be applied successfully, at least, the response that it caused should be acceptable by host, and shouldn't make harmful effects. So the biological materials should be carried on the evaluation of the nano-bio-safety, that is, the biological evaluation. This is also the key tache that if nano-biological material can enter to clinical research [41]. So research about this area is active. As early as 1999, Richardson, etc. [42] had been studied the distribution of chitosan gene carriers in vivo. Highly purified chitosan fractions of <5000 Da, 5000–10000 Da and >10000 Daltons were prepared and characterised in respect of their cytotoxicity, ability to cause haemolysis, ability to complex DNA as well as to protect DNA from nuclease degradation. The observations that the highly purified chitosan fractions used were neither toxic nor haemolytic, that they have the ability to complex DNA and protect against nuclease degradation and that low molecular weight chitosan can be administered intravenously without liver accumulation suggest there is potential to investigate further low molecular weight chitosans as components of a synthetic gene delivery system. Kim [43] synthesized biocompatible silica-overcoated magnetic nanoparticles containing rhodamine B isothiocyanate (RITC) within a silica shell of controllable thickness [MNPs@SiO2(RITC)]. In that study, the MNPs@SiO2(RITC) with 50-nm thickness were used as a model nanomaterial. After intraperitoneal administration of MNPs@SiO2(RITC) for 4 weeks into mice, the nanoparticles were detected in the brain, indicating that such nanosized materials can penetrate blood–brain barrier (BBB) without disturbing its function or producing apparent toxicity. After a 4-week observation, MNPs @SiO2(RITC) was still present in various organs without causing apparent toxicity. Through labeling with rhodamine and got 50nm MNPs@ SiO2 (RITC). Taken together, they demonstrated that magnetic nanoparticles of 50-nm size did not cause apparent toxicity under the experimental conditions of this study.

Yang [44] studied the distribution and toxicity of silicon nanoparticles in vivo. When silica nanoparticles suspension injected in mice , after 96 h, electron microscopy result showed that silica nanoparticles distributed in the brain, liver, heart, spleen, lung, kidney, stomach, intestines, prostate, testis and other organs, and found a large quantity of silica nanoparticles had enter into the cell nucleus of liver and a small amount that cell nucleus of brain. Gave 4500 ug / kg nanoparticles to mice through intraperitoneal injection, two weeks later, there was no obvious abnormalities among mice body weight, appetite, defecation when compared to the control group, none was dead. But some scholars also believe that when the particle size reduced to a certain degree, the substance and material that original have non-toxic or low toxic begin to appear toxicity or toxicity significantly strengthened ; and nano-materials may cause special situation of metabolism, have special toxicity.

Lam *et al*. [45] studied toxicity of carbon nanotubes to the organisms. Compared with carbon black and quartz (pink), carbon nanotubes (0.1-0.5 mg/kg) were injected into rats through trachea. The result showed that the group of carbon black rats was normal, the group of quartz rats had mild to moderate inflammation, observed lung epithelial granuloma in carbon nanotubes group and had relationship with dose-response. These results show that, if carbon nanotubes reach the lungs, they are much more toxic than carbon black and can be more toxic than quartz, which is considered a serious occupational health hazard in chronic inhalation exposures. Service [46] used polytetrafluorethylene (PTFE)-nano to do the inhalation contamination experiment on rat, the diameter of PTFE-nano was 20 nm, the rats were contaminated 15 min, the majority of rats died within 4 h, but rats would not be affected when the diameter was 130 nm. Yang [47] studied the distribution of the original single-walled carbon nanotubes in rats. They found carbon nanotubes mainly distributed in the liver, lungs and spleen, and had long residual time, minute quantity was excluded outer the body through urine or feces. Though hadn't found acute toxicity reaction and allergic reaction, the chronic toxicity of carbon nanotubes to the human body need to be studied in-depth.

6. CONCLUSIONS

Because Nano-drug is a new type drug, the development of nano-drug will cause the revolution of the diagnosis and treatment. In recent years, nano-technology was applied in traditional Chinese medicine and birth to the new concept 'nano Chinese medicine'. Among the active ingredients of Chinese medicine, effective site, the original drug, compound and new agents that using nano-technology making has made some progress. However, at present, the basic theory of nano-technology appiled in medicine and the preparation of nano-drugs are still incomplete, especially the safety of nano- medicines has many problems remain to be explored in depth. Therefore, the research in the field of nano-technology appiled in medicine has a great deal of work needs to be done, but the superior capability that nano-drugs owns indicates a very wide range of applications in the clinical disease treatment.

7. ACKNOWLEDGEMENTS

This work was jointly supported by the Scientific Innovation Project of Northwest Normal University (Grant Nos: NWNU-KJCXGC-03-57, NWNU-KJCXGC-03-49) and the Proficient Talent Project of lanzhou Institute of Chemical Physics, Chinese Academy of Sciences (Grant

SciRes Copyright © 2010

No: 070430SRC1).

REFERENCES

[1] Balogh, L.P. (2009) The future of nanomedicine and the future of Nanomedicine: NBM. *Nanomedicine*, **5**, 1.

[2] Shephard, M.J., Todd, D., Adair, B.M., Po, A.L.W., Mackie, D.P. and Scott, E.M. (2003) Immunogenicity of bovineparainfluenza type 3 virus proteins encapsulated in nanoparticle vaccines, following intranasal administration to mice. *Res. Vet. Sci.*, **74**, 187-190.

[3] Cui, Z.R.and Mumper, R.J. (2002) Intranasal administration of plasmid DNA-coated nanoparticles results in enhanced immune responses. *J. Pharm. Pharmacol.*, **54**, 1195-1203.

[4] Vijayanathan, V., Thomas, T. and Thomas, T.J. (2002) DNA nanoparticles and development of DNA delivery vehicles for gene therapy. *Biochemistry*, **41**, 14085-14094.

[5] Cleland, J.L. (1998) Solvent evaporation processes for the production of controlled release biodegradable microsphere formulations for therapeutics and vaccines. *Biotechnol. Prog.*, **14**, 102-107.

[6] Esfand, R.and Tomalia, D.A. (2001) Poly (amidoamine) (PAMAM) dendrimers:from biomimicry to drug delivery and biomedical applications. *Drug Discovery Today*, **6**, 427-436.

[7] Aukunuru, J.V., Ayalasomayajula, S.P. and Kompella, U.B. (2003) Nanoparticle formulation enhances the delivery and activity of a vascular endothelial growth factor antisense oligonucleotide in human retinal pigment epithelial cells. *J. Pharm. Pharmacol.*, **55**, 1199-1206.

[8] Maeda, H., Wu, J., Sawa, Y., Matsumura, Y. and Hori, K. (2000) Tumor vascular permeability and the EPR effect in macromolecular therapeutics:a review. *J. Control. Release*, **65**, 271-284.

[9] Lukyanov, A.N. and Torchilin, V.P. (2004) Micelles from lipid derivatives of water-soluble polymers as delivery systems for poorly soluble drugs. *Adv. Drug Delivery Rev*. **56**, 1273-1289.

[10] Torchilin, V.P. (2002) PEG-based micelles as carriers of contrast agents for different imaging modalities. *Adv. Drug Delivery Rev*., **54**, 235-252.

[11] Mitra, S., Gaur, U., Ghosh, P.C. and Maitra, A.N. (2001) Tumour targeted delivery of encapsulated dextran doxorubicin conjugate using chitosan nanoparticles as carrier. *J. Control. Release*, **74**, 317-323.

[12] Du, S.L., Pan, H., Lu, W.Y., Wang, J., Wu, J. and Wang J. Y. (2007) Cyclic Arg-Gly-Asp peptide-labeled liposomes for targeting drug therapy of hepatic fibros is in rats. *J. Pharmacol. Exp. Ther*., **322**, 560-568.

[13] Briz, O., Macias, R.I.R., Vallejo, M., Silva, A., Serrano, M.A. and Marin, J.J.G. (2003) Usefulness of liposomes loaded with cytos tatic bile acid derivatives to circumvent chemotherapy res is tance of enterohepatic tumors. *Mol. Pharmacol*., **63**, 742–750.

[14] Saul, J.M., Annapragada, A.V. and Bellamkonda, R.V. (2006) A dual-ligand approach for enhancing targeting selectivity of therapeutic nanocarriers. *J. Control. Release*, **114**, 277-287.

[15] Hashida, M., Akamatsu, K., Nishikawa, M., Yamashita, F., Yoshikawa, H. and Takakura, Y. (2000) Design of polymeric prodrugs of PGE1 for cell-specific hepatic targeting. *Pharmazie*, **55**, 202-205.

[16] Chung, J.E., Yokoyama, M., Aoyagi, T., Sakurai, Y. and Okano, T. (1998) Effect of molecular architecture of hydrophobically modified poly (N-isopropylacrylamide) on the formation of thermoresponsive core-shell micellar drug carriers. *J. Control. Release*, **53**, 119-130.

[17] Kohori, F., Sakai, K., Aoyagi, T., Yokoyama, M., Sakurai, Y. and Okano, T. (1998) Preparation a characterization of thermally responsive block copolymer micelles comprising poly (N-isopropylacrylamide-β-DL-lactide). *J. Control. Release*, **55**, 87-98.

[18] Meyer, O., Papahadjopoulos, D. and Leroux, J.C. (1998) Co- polymers of N-isopropylacrylamide can trigger pH sensitivity to stable liposomes. *FEBS Lett.* **421**, 61-64.

[19] Stover, T.C., Kim, Y.S., Lowe, T.L. and Keste, M. (2008) Thermoresponsive and bio-degradable linear-dendritic nanoparticles for targeted and sustained release of a pro-apoptotic drug. *Biomaterials*, **29**, 359-369.

[20] Na, K., Lee, E.S. and Bae, Y.H. (2003) Adriamycin loaded pullulan acetate/sulfonamide conjugate nanoparticles responding to tumor pH: pH-dependent cell interaction, internalization and cytotoxicity in vitro. *J. Control. Release*, **87,** 3-13.

[21] Yoo, H.S., Lee, E.A. and Park, T.G. (2002) Doxorubicin-conjugated biodegradable polymeric micelles having acid-cleavable linkages. *J. Control. Release*, **82**, 17-27.

[22] Xiao S.Y., Tong, C.Y., Liu, X.M., Yu, D.M., Liu, Q.L., Xue, C.G., Tang, D.Y. and Zhao, L.J. (2006) Preparation of folate-conjugated starch nanoparticles and its application to tumor-targeted drug delivery vector. *Chin. Sci. Bull*, **51**, 1151-1155.

[23] Pan, J. and Feng, S.S. (2008) Targeted delivery of pa clitaxel using folate-decorated poly(lactide)-vitaminE TPGS nan-oparticles. *Biomaterials*, **29**, 2663-2672.

[24] Terada, T., Iwai, M., Kawakami, S., Yamashita, F. and Hashida, M. (2006) Novel PEG-matrix metalloproteinase-2 cleavable peptide-lipid containing galactosylated liposomes for hepatocellular carcinoma-selective targeting. *J. Control. Release*, **111**, 333-342.

[25] Sershen, S.R., Westcoot, S.L., Halas, N.J. and West, J.L. (2000) Temperature-sensitive polymer-nanoshell composites for photothermally modulated drug delivery. *J. Biomed. Mater. Res.*, **51**, 293-298.

[26] Sun, Y., Lu, M. and Yin, X.F. (2006) Ntracellular delivery of fluoresent dyes mediated by nanometer-liposomes. *Chem. J. Chin. U*., **27**, 632-634.

[27] Sivaramakrishnan, R., Nakamura, C., Mehnert, W., Korting, H.C., Kramer, K.D. and Schafer-Korting, M. (2004) Glucocorticoid entrapment into lipid carriers-characterization by parelectric spectroscopy and influence on dermal uptake. *J. Control. Release*, **97**, 493-502.

[28] Ding, J.C., Hu, F.Q. and Yuan, H. (2004) Uptake of mono-stearin solid lipid nanoparticles by A549 cells. *Acta Phamaceutica Sinica*, **39**, 876-880.

[29] Pantarotto, D., Partidos, C.D., Hoebeke, J., Brown, F., Kramer, E., Briand, J.P., Muller, S., Prato, M. and Bianco, A. (2003) Mmunization with peptide-functionalized carbon nanotubes enhances virus-specific neutralizing antibody responses. *Chem. Biol.*, **10**, 961-966.

SciRes Copyright © 2010

[30] Becker, M.L., Fagan, J.A., Gallant, N.D., Bauer, B.J., Bajpai, V., Hobbie, E.K., Lacerda, S.H., Migler, K.B. and Jakupciak, J.P. (2007) Length-dependent up take of DNA-wrapped single-walled carbon nanotubes. *Adv. Mater*., **19**, 939-945.

[31] Ito, Y., Venkatesan, N., Hirako, N., Sugioka, N. and Takada, K. (2007) Effect of fiber length of carbon nanotubes on the absorption of erythropoietin from rat small intestine. *Int. J. Pharm*., **337**, 357-360.

[32] Masaro, L. and Zhu, X.X. (1999) Physical models of diffusion for polymer solutions, gels and solids. *Prog. Polymer Sci.*, **24**, 731–775.

[33] Frank, A., Rath, S.K. and Venkatraman, S.S. (2005) Controlled release from bioerodible polylners : effect of drug type and polymer composition. *J. Control. Release*, **102**, 333-344.

[34] Du, Q., Hu, J.L., Han, Y.D., Chen, X.S. and Jing, X.B. (2008) Preparation of controlled-release microspheres loading protein through solid-in-oil-water emulsion method. *Chem. J. Chin. U*., **29**, l262-1266.

[35] Yang, Y.N., Lou, L., Liang, Q.Z., Chen, X.S. and Jing, X.B. (2004) Preparation and in vitro release of rifampin microspheres encapsulated in biodegradable polyesters. *Chem. J. Chin. U.*, **25**, 162-165.

[36] Jain, R.A. (2000) The manufacturing techniques of various drug loaded biodegradable poly(lactide-co-glycolide) (PLGA) devices. *Biomaterials*, **21**, 2475-2490.

[37] Wang, Y.M., Sato, H. and Horikoshi, I. (1997) In vitro and in vivo evaluation of taxol release from poly(lactic-co-glycolic acid) microspheres containing isopropyl myri- state and degradation of the microspheres. *J. Control. Release*, **49**, 157-166.

[38] Wang, Y.S., Wang, Y.M., Li, R.S., Zhao, J. and Zhang, Q.Q. (2008) Chitosan-based self-assembled nanomicelles as a novel carrier for paclitaxel. *Chem. J. Chin. U.*, **29**, 1065- 1069.

[39] Li, J.H., Yu, Y.W., Yu, Y.L. and Shen, W. (2000) Studies on preparation of carboxymethylchitosan. *Chin. J. Biochem. Pharmaceutics*, **21**, 175-177.

[40] Yang, X.F. and Xi, T.F. (2001) Progress in the studies on the evaluation of biocompatibility of biomaterials. *J. Biomed. Eng*., **18**, 123-128.

[41] Fan, C.X. and Chen, L. (2004) Application of molecular biological methods to the study of biomaterial evaluation. *Biomed. Eng.: Foreign Med. Sci.*, **27**, 375-379.

[42] Richardson, S.C., Kolbe, H.V. and Duncan, R. (1999) Potential of low molecular mass chitosan as a DNA delivery system: biocompatibility, body distribution and ability to complex and protect DNA. *Int. J. Pharm.*, **178**, 231-243.

[43] Kim, J.S., Yoon, T.J., Yu, K.N., Kim, B.G., Park, S.J., Kim, H.W., Lee, K.H., Park, S.B., Lee, J.K. and Cho, M.H. (2006) Toxieity and tissue distribution of magnetie nanopartieles in mice. *Toxicol. Sci.*, **89**, 338-347.

[44] Yang, J.Y., Chen, Y.X. and Zhang, Y.D. (2005) In vivo distribution of silicon nanoparticles and toxicity tests, China Medical Engineering. *Chin. Med. Eng.*, **13**, 585-590.

[45] Lam, C.W., Jmes, J.T., McCluskey, R. and Hunter, R.L. (2004) Pulmonary toxicity of single-wall carbon nanotubes in mice 7 and 90 days after intratracheal instillation. *Toxicol. Sci*., **77**, l26-134.

[46] Service, R.F. (2003) Nanomaterials show signs of toxicity. *Science*, **300**, 243.

[47] Yang, S.T., Guo, W., Lin, Y., Deng, X. Y., Wang, H. F., Sun, H.F., Liu, Y.F., Wang, X., Wang, W., Chen, M., Huang, Y.P. and Sun, Y.P. (2007) Biodistribution of pristine single-walled carbon nanotubes in vivo. *J. Phys. Chem. C*, **111**, 17761-17764.

SciRes Copyright © 2010

Vol.2, No.1, 49-53 (2010)
doi:10.4236/ns.2010.21007

Natural Science

Face recognition based on manifold learning and Rényi entropy

Wen-Ming Cao, Ning Li

Intelligent Information Processing Key Laboratory, Shenzhen University, Shenzhen, China; wmcao@szu.edu.cn

Received 10 September 2009; revised 29 October 2009; accepted 9 November 2009.

ABSTRACT

Though manifold learning has been successfully applied in wide areas, such as data visualization, dimension reduction and speech recognition; few researches have been done with the combination of the information theory and the geometrical learning. In this paper, we carry out a bold exploration in this field, raise a new approach on face recognition, the intrinsic α-Rényi entropy of the face image attained from manifold learning is used as the characteristic measure during recognition. The new algorithm is tested on ORL face database, and the experiments obtain the satisfying results.

Keywords: Manifold Learning; Rényi Entropy; Face Recognition

1. INTRODUCTION

Face recognition has becoming a research hotspot in the fields of image processing, pattern recognition and artificial intelligence in recent years. Numerous research papers appear on the famous international publications, a great deal of capital and manpower is invested to this research and its relevant application system developments. However, the performance of the face recognition could be influenced by many factors, such as illumination, gesture, age, facial expressions, image resolution, and noise, etc; which cause difficulties for the computer processing of face recognition, and turn it into a challenging task at the same time.

The existing face recognition methods can be roughly classified into two categories [1]: local feature based, and global feature based. A local feature based method symbolizes a human face with the extracted feature vectors (eyes, nose, mouth, hair, and face contours), designs certain kinds of classifiers to make recognition. On the other hand, a global feature based method employs the whole images as the input feature vectors, and then low-dimensional features are extracted by some learning algorithms. The main difference between the two categories lies in the way how the features are extracted. In a local feature based method, features are designed completely by the algorithm designers; while in global feature based method, features are automatically extracted or learned by some self-learning algorithms.

Local feature based or learning based methods can be further divided into two classes: 1) statistical learning, such as artificial neural networks (ANN) [2-4], support vector machine (SVM) [5,6], and Boosting [7,8]; 2) manifold learning(or dimensionality reduction), such as linear methods like PCA [9,10], LDA [11,12], and nonlinear methods like Isomap [13], LLE [14], Laplacian Eigenmaps [15,16].

In recent years, nonlinear dimensionality reduction (NLDR) methods have attracted great attentions due to their capability to deal with nonlinear and curved data [1]. All these algorithms rely on an assumption that the image data lie on or close to a smooth low-dimensional manifold in a high-dimensional input image space. A big limitation of NLDR algorithms is the way how to estimate the intrinsic dimension of the manifold. LLE and Laplacian Eigenmaps do not give method to estimate the intrinsic dimension; Isomap shows a simple way to estimate the intrinsic dimension by searching for the "elbow point" where the residual error decreases significantly. However, for some real data, it is difficult to find an obvious "elbow point" to indicate the intrinsic dimension.

The intrinsic dimensionality estimation of a data set is a classical problem of pattern recognition. From the math point, the intrinsic dimension of a manifold is the dimension of the vector space that is homeomorphic to local neighborhoods of the manifold; in other words, intrinsic dimension describes how many "degrees of freedom" are necessary to generate the observed data. When the samples are drawn from a large population of signals one can interpret them as realizations from a multivariate distribution supported on the manifold. The intrinsic entropy of random samples obtained from a manifold is an information theoretic measure of the complexity of this distribution. The entropy is a finite value when the distribution satisfies the restriction of

SciRes Copyright © 2010

Lebesgue integral on the lower dimensional manifold.

In 2003, Costa and Hero proposed an algorithm that can jointly estimate both the intrinsic dimension and intrinsic entropy of a dataset randomly distributed on a smooth manifold [17,18]. The algorithm constructs the Euclidean K-NN graph over all the sample points and use its growth rate to estimate the intrinsic dimension and entropy by simple linear least squares and method of moments procedure. This approach allows for the estimation of the desired quantities using algorithms with low computational complexity that avoid reconstructing the manifold or estimating multivariate distributions.

Considering the fact that on the various conditions of distance, direction, illumination or gestures, one object can form different face images; the corresponding high-dimensional dataset of those images can be viewed as a nonlinear low-dimensional embedded manifold determined by factors of illumination, location, scale, gesture, etc. Based on Costa's algorithm, we take Rényi entropy as the characteristic vector; present a novel face recognition method—Face Recognition Based on Manifold Learning and Rényi Entropy.

2. MANIFOLD LEARNING USING K-NEAREST NEIGHBOR GRAPHS

Costa's algorithm is based on minimal Euclidean graph methods. Let $\chi_n = \{X_1, \cdots, X_n\}$ be n independent identically distributed (i.i.d.) random sample points in a compact subset of $\mathbb{R}^d$, with multivariate Lebesgue density f. x_n is also called the set of random vertices on a minimal Euclidean graph. First, a Euclidean k-nearest neighbors (k-NN) graph is constructed over all the sample points. Let $N_{k,i}(\chi_n)$ be the set of k-nearest neighbors of x_n in X_i. Then the total edge length functional of the Euclidean k-NN graph is:

$$L_\gamma^{K-NN}(\chi_n) = \sum_{i=1}^{n} \sum_{X \in N_{k,i}(\chi_n)} d^\gamma(X, X_i)$$

where γ is a power weighting constant, $d(X, X_i)$ is the Euclidean distance between X and X_i. The k-NN graph exhibits an asymptotic behavior of their total edge functional:

$$\lim_{n\to\infty} L_\gamma(\chi_n)/n^\alpha = \beta_{d,L_\gamma} \exp\{(1-\alpha) H_\alpha(f)\}$$

where β_{d,L_γ} is a constant independent of f, and

$$H_\alpha^{\mathbb{R}^d}(f) = \frac{1}{1-\alpha} \log \int_{\mathbb{R}^d} f^\alpha(x)\, dx$$

is the extrinsic Rényi α-entropy of the multivariate Lebesgue density f. So the asymptotic unbiased and strongly consistent estimator of the α-entropy is:

$$\hat{H}_\alpha(\chi_n) = \frac{1}{1-\alpha}\left[\log L_\gamma(\chi_n)/n^\alpha - \log \beta_{d,L_\gamma}\right]$$

The convergence results for k-NN graphs are extended from Euclidean spaces to general Riemannian manifolds. Let (M, g) be a compact smooth Riemann m-dimensional manifold. Suppose $y_n = \{Y_1, \cdots, Y_n\}$ are i.i.d. random elements of M with bounded density f relative to the volume element μ_g. Let $\hat{L}_\gamma$ be the total edge length of the k-NN graph. Assume $m \geq 2, 1 \leq \gamma < m$ and let $\alpha = (m-\gamma)/m$. Then

$$\lim_{n\to\infty} \frac{\hat{L}_\gamma(y_n)}{n^\alpha} = \beta_{m,L_\gamma} \int_M f^\alpha(y)\, \mu_g(dy)$$

where β_{m,L_γ} is a constant independent of f and M. Accordingly, the asymptotic unbiased and strongly consistent estimator of the α-entropy $H_\alpha^{(M,g)}(f)$ is:

$$\hat{H}_\alpha^{(M,g)}(y_n) = \frac{m}{\gamma}\left[\log(L_\gamma^M(y_n)/n^{(m-\gamma)/m}) - \log \beta_{m,L_\gamma}\right]$$

Define $l_n = \log \hat{L}_\gamma(y_n)$, the convergence theorem (5) suggests the log-linear model below:

$$l_n = a \log n + b + \varepsilon_n$$

where

$$a = (m-\gamma)/m,$$
$$b = \log \beta_{m,L_\gamma} + \gamma/m\, H_\alpha^{(M,g)}(f)$$

and ε_n is an error residual that goes to zero as $n \to \infty$.

Bootstrap resampling is used here to estimate mean graph length $E[L_\gamma^M(y_n)]$, and linear least squares (LLS) is applied to jointly estimate slope $\hat{a}$ and intercept $\hat{b}$ from sequence $\{\log E[L_\gamma^M(y_n)], \log n\}_n$. After that, the following estimates of dimension $\hat{m}$ and entropy $\hat{H}$ are obtained by inversion of the relations:

$$\hat{m} = round\{\gamma/(1-\hat{a})\}$$
$$\hat{H}_\alpha^{(M,g)} = \frac{m}{\gamma}\left(\hat{b} - \log \beta_{\hat{m},L_\gamma}\right)$$

The specific steps of the algorithm are described as:

1) Using entire database of signals $y_n = \{Y_1, \cdots, Y_n\}$ to construct K-NN graph.

2) Estimate the dimension and α-Rényi entropy of the manifold that the sample sets lie in.

a) Set parameters M, N, $p_1, \cdots, p_Q$, ($p_1 < \cdots < p_Q \leq n$);

b) Initialize $\bar{m} = 0, \bar{H} = 0, M' = 1$;

c) Choose P from $p_1, \cdots, p_Q$ in turn,

Ⅰ. $\bar{L} = 0; N' = 1;$

SciRes Copyright © 2010

Ⅱ. Randomly select a subset of P signals y_p from y_n; Compute graph total edge length L_p;

$$\overline{L} = \overline{L} + L_p;$$

Ⅲ. $N' = N' + 1$; if $N' = N$, goto step Ⅳ, else goto Ⅱ;

Ⅳ. Compute sample average graph length $\hat{E}\left[\hat{L}\left(y_p\right)\right] = \overline{L} / N$;

d) Use **Eq.9** to estimate dimension $\hat{m}$ and entropy $\hat{H}$ from $\left\{\hat{E}\left[\hat{L}\left(y_p\right)\right]\right\}_{p=p_1}^{p_o}$;

$$\overline{m} = \overline{m} + \hat{m}_{M'}, \ \overline{H} = \overline{H} + \hat{H}_{M'};$$

e) $M' = M' + 1$, if $M' = M$, goto step (f), else goto (c).

f) The estimate dimension $\hat{m} = \overline{m} / M$; α-Rényi entropy $\hat{H} = \overline{H} / M$.

g). End.

The parameters M and N are used to provide a trade-off between the bias and variance performance of the estimators for finite n. β_{m,L_γ} is the limit of the normalized length functional of the corresponding Euclidean entropic graph for a uniform distribution on the unit cube $[0,1]^m$. It can be determined by performing Monte Carlo simulations of the entropic graph length on the unit cube $[0,1]^m$ for uniform random samples.

Unlike previous solutions, Costa's algorithm can prove statistical consistency of the obtained estimators under weak assumptions of compactness of the manifold and boundedness of the (Lebesgue) sampling density supported on the manifold. This approach allows for the estimation of the desired quantities using algorithms with low computational complexity ($O(n \log n)$) that avoid reconstructing the manifold or estimating multivariate distributions.

3. FACE RECOGNITION ALGORITHM BASED ON MANIFOLD'S RÉNYI ENTROPY

We applied the method to a real high-dimensional dataset with unknown manifold structure and intrinsic dimension and entropy---face images. We chose "ORL Face Database" [19] of AT&T Laboratories Cambridge. There are 10 different images of each of 40 distinct people (40 sample sets). The images were taken at different times, varying the lighting, facial expressions (open / closed eyes, smiling / not smiling) and facial details (glasses / no glasses).

The original image is in PGM format, 92*112 pixels, with 256 grey levels per pixel. We first processed each image into BMP format, 64*64 pixels, normalized the pixel values between [0, 1]. Then we arranged each image in a 4096*1 matrix using the common lexicographic order.

From each of the 40 sample sets $s_i, (i = 1, \cdots, 40)$, we randomly chose 3,4,5,6,7,8 images as the training samples; hence there were 40*3=120, 40*4=160, 40*5=200, 40*6=240, 40*7=280, 40*8=320 samples in the training set respectively. All 400 images were treated as test samples. Each 5,6,7,8 images of the same sample set (4096*5, 4069*6, 4069*7, 4069*8 matrix) were trained at one time to get an estimate Rényi Entropy $\hat{H}_{s_i}$ according to the algorithm introduced in section 2. The estimate entropy served as the characteristic vector of the recognition, each test image X was combined with every 3,4,5,6,7,8 sample images in one sample set (4096*n,n=3,4,5,6,7,8 matrix respectively) to get an estimate Rényi entropy $\hat{H}_x$, then the classification criterion is :

$$\left\{X \in s_k \mid \hat{H}_X - \hat{H}_{S_k} = \min_{i=1,\cdots,40}\left(\hat{H}_X - \hat{H}_{S_i}\right)\right\}$$

X would be classified to the set where its combined entropy is nearest to the origin entropy of the training set.

4. EXPERIMENT RESULTS

The parameters used in the experiment were set as follows: $k = 3, \gamma = 1, M = 1, N = 5, n = 6$. **Figure 1** shows the 5 training images of face 1; and **Figure 2** displays the results of running 20 simulations of the Costa's algorithm

Figure 1. The 5 training images of face 1.

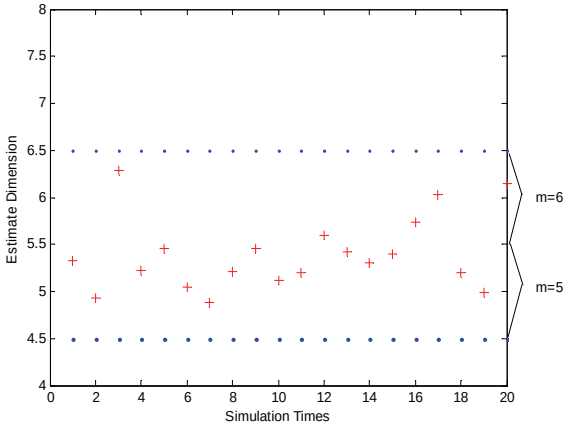

Figure 2. The estimate manifold dimension of face 1 is between 5~6.

SciRes Copyright © 2010

using the 5 training images in **Figure 2**. In same conditions, as shown in Table 3, our Rényi Entropy method gives a weakly higher recognition accuracy compared with PCA and 2DPCA methods for ORL face database in **Figure 3**.

Table 1 shows a part of estimate results of the training set from ORL face database.

Using the Face recognition algorithm in section3, the results of our method are showed in **Table 2**.

The results indicate that the face recognition algorithm based on Manifold's Rényi Entropy we present in this paper works effectively. The K–NN graph is employed so that we avoid the complex estimation of geodesic distances on the manifold.

An important factor influenced the recognition efficiency is the sample number of the same set we used is a little small (only 10), which induce the lack of information needed for training samples. Besides, there must be certain inevitable information loss during the procedure of image pretreatment. Further work includes add bootstrap confidence intervals for the estimators and apply other classification method to minimize the error.

Table 1. Dimension estimate $\hat{m}$ and entropy $\hat{H}$ for some training face images

	$\hat{m}$	$\hat{H}$ (bits)
Face 1	5	20.856
Face 4	6	19.890
Face 7	6	21.052
Face 14	5	20.175
Face 17	5	18.706
Face 39	5	17.804

Table 2. The results of Face recognition algorithm based on Manifold's Rényi Entropy.

Training samples	Computational complexity	Test samples	Error recognition	Correct Recognition rate
120	7	400	118	70.5%
160	8	400	51	87.2%
200	11	400	19	95.2%
240	13	400	12	97%
280	18	400	10	97.5%
320	21	400	7	98.2%

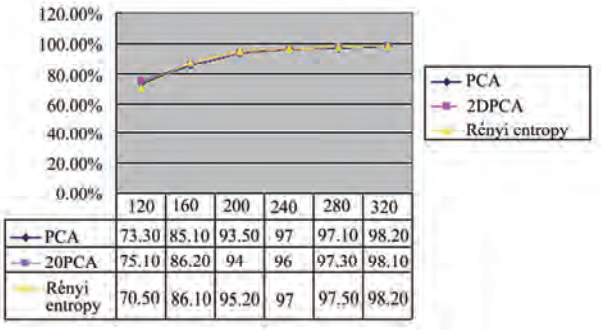

Figure 3. PCA , 2DPCA, Rényi entropy.

5. CONCLUSIONS

We have presented a new face recognition algorithm based on Manifold's Rényi Entropy. The algorithm is applied to ORL face database and the experiments obtain the satisfying results. At present we are studying the theoretic prove of this method, and trying to make further utilizations in other research fields such as pattern recognition and artificial intelligence.

6. ACKNOWLEDGMENTS

The work is supported by the National Science Foundation of China (No.60871093), and Pre-Research and Defense Fund of China: No.9140C80002080C80.

REFERENCES

[1] Lin, T. (2005) Machine perception of human faces: a grand challenge. The Korea Foundations for Advanced Studies (KFAS).

[2] Rowley, H.A., Baluja, S. and Kanade, T. (1998) Neural network-based face detection [J]. *IEEE Trans Pattern Analysis and Machine Intelligence*, **20(1),** 23-38.

[3] Feraud, R., Bernier, O.J., Villet, J.E. and Collobert, M. (2001) A fast and accurate face detector based on neural networks [J]. *IEEE Trans Pattern Analysis and Machine Intelligence*, **22(1)**, 42-53.

[4] Garcia, C. and Delakis, M. (2004) Convolutional face finder: a neural architecture for fast and robust face detection [J]. *IEEE Trans Pattern Analysis and Machine Intelligence*, **26(11)**, 1408-1423.

[5] Osuna, E., Freund, R. and Girosi F. (1997) Training support vector machines: an application to face detection [J]. *Proc, IEEE Conf Computer Vision and Pattern Recognition*, 130-136.

[6] Phillips, P.J. (1998) Support vector machines applied to face recognition [J]. *Adv. Neural Inform. Process. Syst.* **11**, 803-809.

[7] Viola, P. and Jones, M. J. (2004) Robust real-time face detection [J]. *Int. J. Computer Vision*, **57(2)**.

[8] Li, S.Z. and Zhang, Z. (2004) Float boost learning and statistical face detection [J]. *IEEE Trans Pattern Anal. Mach. Intel.*, **26(9)**, 1112-1123.

[9] Kirby, M. and Sirovic, L. (1990) Application of the karhunen-loeve procedure for the characterization of human faces [J]. *IEEE Trans Pattern Anal. Mach. Intel.*, **12(1)**, 103-108.

[10] Turk, M. and Pentland, A. (1991) Eigenfaces for Recognition [J]. *J. Cogn. Neurosci*, **3**, 72-86.

[11] Belhumeur, P.N., Hespanha, J.P. and Kriegman, D.J. (1997) Eigenfaces vs. fisherfaces: recognition using class specific linear projection [J]. *IEEE Transactions on Pattern Analysis and Machine Intelligence*, **19(7)**, 711- 720.

[12] Kim, T.K. and Kittler, J. (2005) Locally linear discriminant analysis for multimodally distributed classes for face recognition with a single model image [J]. *IEEE Transactions on Pattern Analysis and Machine Intelligence*, **27(3)**, 318-327.

SciRes Copyright © 2010

[13] Tenenbaum, J.B., de Silva, V. and Langford, J.C. (2000) A global geometric framework for nonlinear dimensionality reduction [J] *Science*, **290**, 2319-2323.

[14] Roweis, S.T. and Saul L.K. (2000) Nonlinear dimensionality reduction by locally linear embedding [J]. *Science*, **290**, 2323-2326.

[15] Belkin, M. and Niyogi, P. (2003) Laplacian eigenmaps for dimensionality reduction and data representation [J]. *Neural Computation*, **15(6)**, 1373-1396.

[16] He, X., Yan, S., Hu, Y., Niyogi, P., and Zhang, H. (2005) Face recognition using laplacianfaces [J]. *IEEE Transactions on Pattern Analysis and Machine Intelligence*, **27(3)**, 328-340.

[17] Costa, J.A. and Hero, A.O. (2003) Entropic graphs for manifold learning [J]. *In the Thirty-Seventh Asilomar Conference on Signals, Systems and Computers*, 316- 320.

[18] Costa, J.A. and Hero, A.O. (2004) Manifold learning using *k*-nearest neighbor graphs [J]. *Proc. of IEEE Int. Conf. on Acoust. Speech and Signal Processing*. Montreal, Canada.

[19] ORL, *Face Database*, AT&T Laboratories Cambridge. [DB/OL]. http://www.cl.cam.ac.uk/Research/DTG/attarchive/pub/data/att_faces.zip.

SciRes Copyright © 2010

Vol.2, No.1, 54-55 (2010)
doi:10.4236/ns.2010.21008

Natural Science

Relationship between normalized thermal energy and conductivity for cylindrical tokamak geometry

M. Asif

Department of Physics, COMSATS Institute of Information Technology, Lahore, Pakistan

Received 23 November 2009; revised 4 December 2009; accepted 7 December 2009.

ABSTRACT

The relation between normalized thermal energy and conductivity, with no particle sources in cylindrical tokamak geometry has been derived. It is obtained, $\beta_p = \frac{\sigma_\perp}{\sigma_\parallel}$. This relationship is of importance for tokamak confinement and heating.

Keywords: Thermal Energy; Cylindrical Geometry; Confinement

1. INTRODUCTION

It was previously shown [1], using a numerical analysis, that from the poloidal and toroidal components of Ohm's law for a tokamak, there follows a relation between the normalized thermal-energy content, β, and the normalized plasma current, 1/q, which only depends on the plasma refueling and not on thermal-energy transport. Previously, the relation was examined only numerically and it is the purpose of [2] to provide an approximate analytical expression for this relation valid for tokamaks, showing explicitly the dependence on the fueling parameters. The relation [3] implies a constraint on the thermal-energy content which cannot be violated, whatever the energy transport present and the plasma heating used. It should be noted that a different relation [4,5] has been derived. Analogous to that of above models, can be obtained by following the same procedure but using Ohm's law [6]. The main focus of this paper is to show the relation between normalized thermal energy and conductivity, with no particle sources in cylindrical tokamak geometry. It is obtained, $\beta_p = \frac{\sigma_\perp}{\sigma_\parallel}$. This relationship is of importance for tokamak confinement and heating, since it provides a direct constraint on the thermal-energy content which cannot in any case be violated, whatever the energy transport presents.

2. RELATION BETWEEN NORMALIZED THERMAL ENERGY AND CONDUCTIVITY

We consider the problem of determining the steady state in cylindrical tokamak geometry with no particle sources. First of all, we recall the expressions for the toroidal and poloidal components of Ohm's law, which can be put in the following form [6], with no particle sources in the limit of large aspect ratio and circular magnetic surfaces:

$$j_\phi = E_\phi / \eta_{II} \tag{1}$$

$$\frac{dp}{dr} = -E_\varphi B_\theta / \eta_\perp \tag{2}$$

where all quantities are surface-averaged and depend on the minor radius r, J_ϕ is the toroidal component of the current density, E_ϕ is the electric field, η_{II} and $\eta_\perp$ is the parallel and perpendicular resistivities, B_ϕ and B_θ are the toroidal and poloidal components of the magnetic field, p is the plasma pressure. The safety factor is $q=r\,B_\phi/R\,B_\theta$ and R is the major radius. The minor radius of the last closed magnetic surface will be indicated by a, and B_θ and J_ϕ are related by Ampere's law

$$j_\phi = \frac{1}{\mu_0 r}\frac{d(rB_\theta)}{dr} \tag{3}$$

Substituting **Eq.1** into **Eq.2**, one obtains the following equation:

$$\frac{dp}{dr} = -\frac{\eta_{II} j_\phi B_\theta}{\eta_\perp} \tag{4}$$

It should be stressed that, in comparing tokamak experiments with theory, one can certainly use the cylindrical approximation where all quantities depend only on minor radius *r*; however, one must then consider the relations between surface-averaged quantities. In this

SciRes Copyright © 2010

case, the perpendicular component of Ohm's law contains the toroidal corrections (Pfirsch-Schlüter and viscosity or trapping terms) which are proportional to the square of the safety factor and which are absent for the exactly cylindrical case. In this paper these terms were not considered.

The normalized thermal-energy content β_p can be defined by

$$\beta_p = \frac{2\mu_0}{B_\theta^2(a)}\langle p \rangle \tag{5}$$

where $\langle .. \rangle$ indicates the volume average and, in the cylindrical approximation,

$$\langle p \rangle = \frac{2}{a^2}\int_0^a p(r) r dr \tag{6}$$

So that, if $p(a)=0$, we also have, by integrating by parts,

$$\langle p \rangle = -\frac{1}{a^2}\int_0^a \frac{dp}{dr} r^2 dr \tag{7}$$

Substituting **Eq.7** into **Eq.5**, one obtains the following equation:

$$\beta_p = -\frac{2\mu_0}{a^2 B_\theta^2(a)}\int_0^a \frac{dp}{dr} r^2 dr \tag{8}$$

Substituting **Eqs.3** and **4** into **Eq.8**, one obtains the following equation:

$$\beta_p = \frac{\sigma_\perp}{\sigma_\parallel} \tag{9}$$

We have obtained relation between normalized thermal energy (poloidal beta) and conductivity, with no particle sources in cylindrical tokamak geometry. This relationship is a generalization of the usual Bennett relation and it is of importance for tokamak confinement and heating. It should be noted that different relations, analogous to that given above, can be obtained by following the same procedure using Ohm's law [6]. The consideration of the generalized Bennett relation is of importance for the problem of plasma confinement and heating, since it provides a direct constraint on the thermal-energy content which cannot in any case be violated, whatever the energy trans-port present and the heating used.

3. CONCLUSIONS

We have obtained relation between normalized thermal energy and conductivity, with no particle sources in cylindrical tokamak geometry. It is obtained, $\beta_p = \frac{\sigma_\perp}{\sigma_\parallel}$.

This relationship is of importance for tokamak confinement and heating, since it provides a direct constraint on the thermal-energy content which cannot in any case be violated, whatever the energy transport present and the heating used.

REFERENCES

[1] Segre, S.E. and Zanza, V. (1992) A profile constraint and the value of beta in tokamak experiments. *Plasma Physics and Controlled Fusion*, **34(11),** 1619-1637.

[2] Segre, S.E. and Zanza, V. (1993) A relation between the normalized thermal energy and the safety factor for tokamaks. *Nuovo Cimento*, **15D(6),** 897-901.

[3] Bennett, W.H. (1934) Magnetically self-focusing streams. *Physical Review*, **45,** 890-897.

[4] Asif, M. (2008) Relationship between current density and mass density for ohmic tokamak plasmas. *International Journal of Modern Physics B*, **22(30),** 5329-5333.

[5] Asif, M. (2009) Relationship between viscosity and conductivity for tokamak plasmas. *Brazilian Journal of Physics*, **39(1),** 59-61.

[6] Segre, S.E. and Zanza, V. (1992) Is the perpendicular resistivity in tokamaks really much greater than the Spitzer value? *Physics of Fluid*, **4(10),** 3457-3459.

SciRes Copyright © 2010

Vol.2, No.1, 56-62 (2010)
doi:10.4236/ns.2010. 21009

Natural Science

Research of handwriting detecting system for space pen

Zong-Yu Gao[1], De-Sheng Li[1], Wei Wang[1], Chun-Jie Yang[2]

[1]MEMS Technology Research Center, Beijing University of Technology, Beijing, China; gzy19750510@163.com
[2]Department of Information & Contral XI'AN University of Posts & Telecommunications, Xi'an, China; ycj2000@hotmail.com

Received 27 August 2009; revised 27 September 2009; accepted 28 September 2009.

ABSTRACT

A handwriting detecting system based on Micro-accelerometer and Micro-gyros is proposed. And the algorithm of the detecting system is also described in detail. And the error analysis of the detecting system is also described in detail. The motion contrail of the handwriting detecting in the 3-D space can be recognized through compute the matrix of attitude angles and the dynamic information of the handwriting detecting which is mapped on the 2-D plane. Then the information of contrail can be recurred on the writing plane by integral. There were good results in the actual experiment.

Keywords: Handwriting Detecting; Micro-Gyro; Micro-Accelerometer

1. INTRODUCTION

MEMS (Micro-Electro-Mechanical Systems) inertial sensors because of its small size, lightweight and low power characteristic etc, in the portable device Human-Computer Interaction pay close attention. Acceleration sensor has been loaded in the mobile and through its gesture to replace parts of the keyboard input, such as implementation in applications of menu selection. However, these function are through contact with the touch screen under the situation, how to off-line and without the case of optical instruments to achieve the above function is a problem to be resolved.

The article introduces a contrail detecting system in 3-D space, which does not need a pad below. The system based on spatial navigation technology, which computes the dynamic information of the handheld devices in the mapping plane through detecting the acceleration of the handheld devices in the space relative to the writing plane [1-3]. The system uses three Micro-accelerometer and three Micro-gyros as the sensor unit, through computation the attitude angles of the handheld devices in 3-D space in real time, the linear acceleration of each axis of the handheld device's coordinates can be gotten, then the contrail information on the mapping plane also can be gotten after mapping and integration [4,5].

2. SYSTEM STRUCTURE

The handheld devices uses a single DSP chip as the control unit, its function is computation of attitude angles of the pen in 3-D space and the linear acceleration. The data sample unit is constituted by one tri-axis Micro-gyros and one tri-axis accelerometer ADSI16350, both of the two kinds of sensors are manufactured by ADI company, and there also is a 16-bit A/D converter LTC1867 which is made by Linear company. The handheld device communicates with PC by RF mode, thus the contrail of the handheld devices will be displayed, and a LCD also can work.

3. CONTRAIL DETECTING ALGORITHM

3.1. The Handheld Device System Model

Figure 1 shows the handheld devices model in 3-D space, the XOY plane is the writing plane, namely the plane that info of the handheld devices mapped. The oxyz coordinates is attached to the handheld devices, namely the coordinates of the sensor installed. To get the contrail that is mapped on the writing plane, several physical variables are needed. These variables are acceleration of each axis of measurement coordinates (A_x, A_y, A_z), and the pitch angle (φ, the angle between axis oz and XOY plane), the roll angle (θ, the angle between axis ox and XOY plane), and the yaw angle (ψ, the angle between axis oy and XOY plane). Yaw angle can be ignored because of its little influence on result.

3.2. The Algorithm Introduction

The algorithm contains three parts: the measurement coordinates confirmation, the matrix of attitude angles confirmation and the solution to the handheld devices of which the acceleration mapped on the writing plane.

SciRes Copyright © 2010

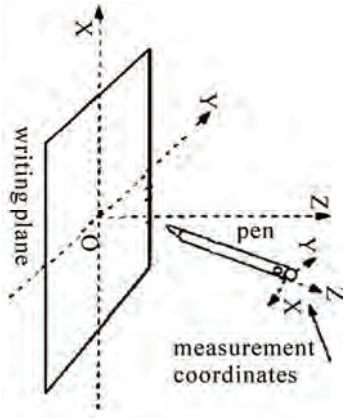

Figure 1. System model.

The simplest instance is that the object is regarded as a point to be measured, so that the attitude changes caused by rotation can be ignored. So we only need to measure the movement characteristics on the 3 axes. Thus, the movements of this object can be expressed simply by kinematics equations. The velocity and displacement information can be gotten through computing the acceleration by following equations.

$$\begin{cases} v_n = \int_{t_0}^{t_e} a_n dt + v_0 \\ s_n = \int_{t_0}^{t_e} v_n dt + s_0 \end{cases} \quad (1)$$

'n' on behalf of any axis among X, Y, Z of the absolute coordinates, v_0, s_0 on behalf of original velocity and displacement respectively, t_0 is start time of measurement, t_e is stop time of measurement. So we only need to measure the acceleration of 3 axes, the start time and stop time to get the velocity and displacement characteristics on the 3 axes. The handheld devices cannot be seen as a point, because of its shape, shown as in **Figure 1**. Firstly, the handheld device's coordinates need to be confirmed. Suppose g_x, g_y, g_z on behalf of the weights of gravitational acceleration on 3 axes of handheld device's coordinates. Because the changes of yaw angle have a little influence on the accelerometer when the handheld device moves horizontally or vertically, the system can be simplified as yaw angle equal to zero. The pitch angle φ and roll angle θ between handheld device's coordinates and writing plane's coordinates can be gotten in following equations. In this system writing plane's coordinates superposes with geographical coordinates.

$$\begin{cases} \varphi = \arcsin(g_x / g) \\ \theta = \arcsin(g_y / g) \end{cases} \quad (2)$$

The relationship of acceleration mapped on writing plane from handheld device's coordinates expressed by equations:

$$\begin{pmatrix} a_X \\ a_Y \\ a_Z \end{pmatrix} = \begin{pmatrix} 1 & 0 & 0 \\ 0 & \sin\theta & -\cos\theta \\ 0 & \cos\theta & \sin\theta \end{pmatrix} \begin{pmatrix} \cos\phi & -\sin\phi & 0 \\ \sin\phi & \cos\phi & 0 \\ 0 & 0 & 1 \end{pmatrix} \begin{pmatrix} \cos\psi & 0 & -\sin\psi \\ 0 & 1 & 0 \\ \sin\psi & 0 & \cos\psi \end{pmatrix} \begin{pmatrix} a_x \\ a_y \\ a_z \end{pmatrix} \quad (3)$$

There into the **Eq.3**

$$\theta = \theta_0 + \theta', \phi = \phi_0 + \phi', \psi = \psi_0 + \psi',$$

θ', ϕ', ψ' on behalf of the dynamic angle changes which sample by micro-gyros during the writing action [6].

Original attitude angle determines the beginning situation of writing plane, the angles between writing plane and geographical coordinates are pitch ϕ_0, roll θ_0, and yaw ψ_0. Because the yaw angle varies little during the handheld device's movement, the yaw angle regards as a constant, namely $\psi' \approx 0$, the above equations can be simplified as:

$$\begin{pmatrix} a_X \\ a_Y \\ a_Z \end{pmatrix} = \begin{pmatrix} 1 & 0 & 0 \\ 0 & \sin\theta & -\cos\theta \\ 0 & \cos\theta & \sin\theta \end{pmatrix} \begin{pmatrix} \cos\phi & -\sin\phi & 0 \\ \sin\phi & \cos\phi & 0 \\ 0 & 0 & 1 \end{pmatrix} \begin{pmatrix} a_x \\ a_y \\ a_z \end{pmatrix} \quad (4)$$

Through (4), the three weights of gravitational acceleration mapped on writing plane can be gotten by the same way. As shown in (5), A_* on behalf of the linear acceleration of each axis of writing plane' coordinates, a_* on behalf of the actual output acceleration of each axis of handheld device's coordinates, g_* on behalf of the mapping gravitational acceleration value of writing plane' coordinates [7].

$$A_* = a_* - g_* \quad (5)$$

The basic equations to compute the velocity and displacement are shown in the following equations [8]:

$$\begin{cases} v_d = \int_{t_0}^{t_e} A_d dt + v_0 \\ s_d = \int_{t_0}^{t_e} v_d dt + s_0 \end{cases} \quad (6)$$

'd' on behalf of any direction among X, Y, and Z.

After sampling the acceleration signal becomes discrete signal, so the accumulative total will instead of the integral. Suppose the weights of acceleration on mapping plane (writing plane) are shown as follow:

$$a_{0i} = \left(a_{0ix},\ a_{0iy},\ a_{0iz}\right)^T$$

Sampling interval is Δt, $\Delta T = 5\Delta t$ suppose displacement variable $S = (S_x,\ S_y,\ S_z)$, following equations can be gotten.

$$\begin{aligned} S_x &= \sum_{j=u}^{u+4} \left(\sum_{i=k}^{k+4} a_{0x}(i+j)\Delta t \right) \Delta T \\ S_y &= \sum_{j=u}^{u+4} \left(\sum_{i=k}^{k+4} a_{0y}(i+j)\Delta t \right) \Delta T \end{aligned} \quad (7)$$

SciRes Copyright © 2010

(k=1,2,3,4,…n; u=0,1,2,3,…n-4).

Recurrence formulas of displacement can be gotten from **Eq.7** which is shown as follow:

$$\begin{aligned} S_{x(i+1)} &= S_{xi} - (\sum_{k=i}^{i+4} a_{0xk}\Delta t)\Delta T + (\sum_{k=i+5}^{i+9} a_{0xk}\Delta t)\Delta T \\ S_{y(i+1)} &= S_{yi} - (\sum_{k=i}^{i+4} a_{0yk}\Delta t)\Delta T + (\sum_{k=i+5}^{i+9} a_{0yk}\Delta t)\Delta T \end{aligned} \tag{8}$$

The **Eq.8**

$$S_1 = \sum_{j=0}^{4}(\sum_{i=1}^{5} a_0(i+j)\Delta t)\Delta T$$

3.3. The Error Analysis

In an ideal process of writing directly to mind is the measured acceleration in all axes whether zero at the beginning and end of exercise. But because of inherent acceleration sensor error and pen gesture of placing will lead to all directions on the different components of the acceleration due to gravity. Because of the sensor itself error and AD conversion error, even in the handheld device to maintain stationary, signal acquisition is not entirely the same, so the time points should not have direct access $t_0 = 0$ and $t_e = T$. For determine the starting point and termination points of each contrail. Here the first analysis method carried out using differential treatment. For the static sensor error is relatively small and homogeneous data, according to whether the difference exceeds a certain threshold to determine whether exercise has happened. But the problems of the difference method are individual points fluctuations may result in greater volatility, however the exercise is not happen. In addition in a sport the course may also appear repeatedly volatility, so this difference should not describe the problem very well. Standard deviation analysis method can be used on this phenomenon, in the writing process can be seen in a single point because of the existence of measurement error and the entire writing process of non-continuous and high acceleration characteristics, should not only depend on a single point to distinguish the beginning and end of a sign. Therefore it need to consider the local statistical characteristics to the process of writing .such as through calculated standard deviation of multiple points as a criterion exercise.

The equation of standard deviation is expressed:

$$\begin{cases} \bar{x}_k = \left(\sum_{i=0}^{N-1} x_{k-i}\right)/N \\ \sigma_k = \sqrt{\left[\sum_{i=0}^{i=N-1}\left(x_{k-i} - \bar{x}_k\right)^2\right]/(N-1)} \end{cases} \tag{9}$$

‘$\bar{x}_k$’ on behalf of mean of x, ‘σ_k’ on behalf of standard deviation.

Calculating the standard deviation of each point except to capitalize on the current point, but also necessary to use the previous $N-1$ points.

Writing at the track which also need to reduce the signal noise ratio, where the use of smoothing methods. If the true signal is smooth, smooth deal will only reduce the signal noise, it will not distort the true picture signal.

Point smoothing algorithm's basic equation:

$$S_j = \frac{f_k Y_{j-k} + \cdots + f_0 Y_j + \cdots + f_k Y_{j+k}}{2\sum_{i=1}^{k} f_i + f_0},$$

$$k = \frac{m-1}{2},\ j = k+1, \cdots, n-k \tag{10}$$

S_j on behalf of the j point value of the Smooth signal, Y_j on behalf of the j point value of original signal. Through selection of different factors f_i can get smoothing of different forms and noise level. Here we used the triangular approach to deal with smooth, triangular smooth manner can avoid the disturbance to the peak signal, which is a weighted smoothing method. Here $f_i \equiv k+1-i$, the basic equation of triangle smoothing:

$$S_j = \frac{1 \bullet Y_{j-k} + \cdots + (k+1) \bullet Y_j + \cdots + 1 \bullet Y_{j+k}}{(k+1)^2},$$

$$k = \frac{m-1}{2},\ j = k+1, \cdots, n-k \tag{11}$$

Triangle smoothing can be seen as two k point rectangular smooth superposition, so the triangular smooth approximation to reduce the level of random noise is k. After smoothing process and standard deviation calculated, the finally signal can be used to determine the contrail starting point and termination point. The use of triangular smoothing method reduces the data noise, after smoothing the bias reduces, but does not change shape. **Figure 2** is the view of five untreated Error. **Figure 3** is the view of five treated Error. The curve of **Figure 3** is more smoothness than this **Figure 2**.

4. SENSOR CALIBRATION

4.1. Micro-Gyro Rate Test Model

In this system gyro is used for real-time detect the change of initial state attitude angle, it is very important for elimination gravity acceleration components, so the gyro calibration also is very important. In the following

SciRes Copyright © 2010

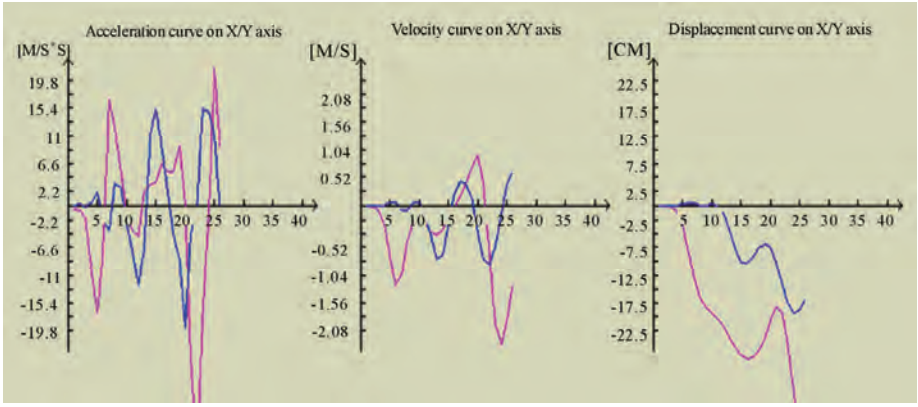

Figure 2. View of five untreated error.

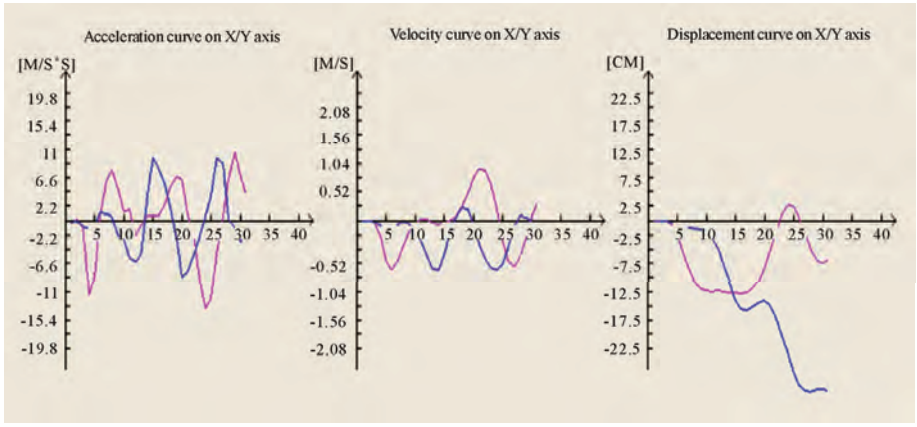

Figure 3. View of five treated error.

is the gyro rate test model [9]. Take ADXRS401 micro-gyro, for example:

$$V = K0 + K1 \times \omega \quad (12)$$

V-Output voltage of micro-gyro, unit is V;
K0-Drift value of micro-gyro, unit is V;
K1-Scale factor of micro-gyro, unit is V/°/s;
ω-Angular velocity input of micro-gyro, unit is °/s。

4.2. Micro-Gyro Calibration Test

① Put the micro-gyro in the test equipment and fixes the sensor on the turntable, the equipment we used is DTOP300E type uniaxial turntable.

② Give micro-gyro power supply of 5 V.

③ Through the turntable computer given ±10°/s, ±20°/s, ±30°/s, ±40°/s, ±50°/s, ±60°/s, ±70°/s angular velocity input.

④ After the turntable rotated at least four round by one angular velocity we began to sample and sampled continuously for one minute, then recorded one group data, finally we can get 15 group data, shown in the following **Table 1**.

Table 1. Micro-gyro calibration data.

augular velocity (°/s)	gyro I output (V)	gyro II output (V)
70	3.265	3.594
60	3.125	3.441
50	2.988	3.291
40	2.849	3.132
30	2.702	2.981
20	2.558	2.832
10	2.419	2.670
0	2.290	2.520
-10	2.150	2.330
-20	2.010	2.209
-30	1.870	2.061
-40	1.731	1.914
-50	1.593	1.757
-60	1.455	1.602
-70	1.317	1.451

Through Matlab data fitting can get:
Gyro Ⅰ: K0=2.290, K1=0.0139 namely: V= 2.290 + 0.0139 ω
Gyro Ⅱ: K0=2.520, K1=0.0153 namely: V= 2.520+0.0153 ω

SciRes Copyright © 2010

4.3. Micro-Accelerometer Calibration Test

The micro-accelerometer is used to test the attitude angles when the pen hasn't yet write, in other word it's used to test the static attitude angles. Due to the acceleration sensor adopted for integrated triaxial acceleration sensor, so the orthogonal error will not affect the precision, then, the most error sources are zero error and sensitivity error and the error caused by the A/D conversion errors. We select ±g and 0g as the special points to calibration the sensor's zero output and sensitivity[10]. The **Table 2** shows calibration results of each axis of x, y, z. The ADC is 16bit and reference voltage is 4.096V.

5. SYSTEM TEST RESULT ANALYZE

In the system test process we tested the round contrail and analyzed the dynamic characters of this contrail which is representative. The dynamic curves are shown in following figures. Axis z of accelerometer is perpendicular to the mapping plane due to the sensor installation, so the axis z has no effect on the contrail recurrence. To recur the writing contrail the acceleration of axis x and axis y of accelerometer are needed both. As shown in **Figure 2** are curves of acceleration, velocity and displacement of the five contrail without error treatment. As shown in **Figure 3** are curves of acceleration, velocity and displacement of the five contrail through error treatment. As shown in **Figures 4,5 and 6** are curves of acceleration, velocity and displacement of the five contrail through error treatment. Analysis of **Figures 4,5 and 6**. According to **Figure 4**, the acceleration is positive between the sample points 7 to 14. According to the **Eq.1** we can know that the speed is increased at these points, as **Figure 5** show, the speed curve is rising from point 7 to 14. However because of the error，this paragraph curve is not ideal one, Thus, the use of Ⅲ C error handling can be used for their amendments in order to

Table 2. Micro-accelerometer calibration data.

			X axis (V)			mean
0	1.501	1.498	1.496	1.505	1.495	1.499
+g	1.795	1.793	1.790	1.798	1.791	1.793
-g	1.205	1.203	1.200	1.211	1.202	1.204
S			0.295v/g			
			Y axis (V)			mean
0	1.524	1.520	1.522	1.518	1.525	1.522
+g	1.823	1.820	1.818	1.820	1.824	1.821
-g	1.225	1.220	1.222	1.220	1.224	1.222
S				0.299v/g		
			Z axis (V)			mean
0	1.504	1.505	1.508	1.503	1.505	1.505
-g	1.807	1.805	1.811	1.812	1.801	1.807
+g	1.203	1.203	1.201	1.208	1.205	1.204
S			0.302v/g			

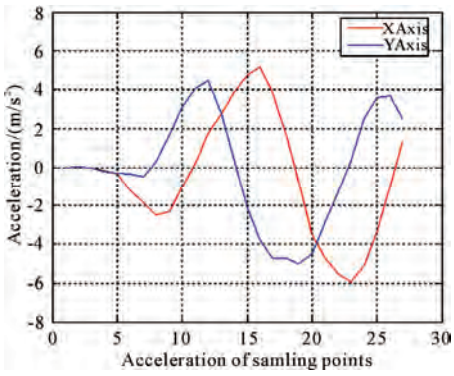

Figure 4. Acceleration curve.

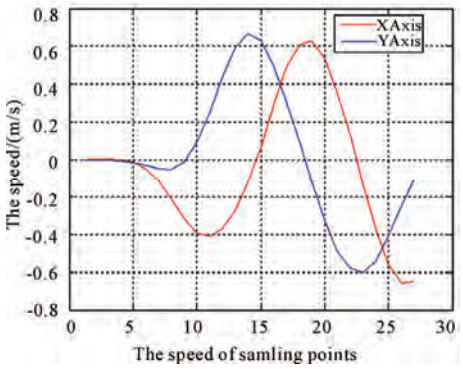

Figure 5. Velocity curve.

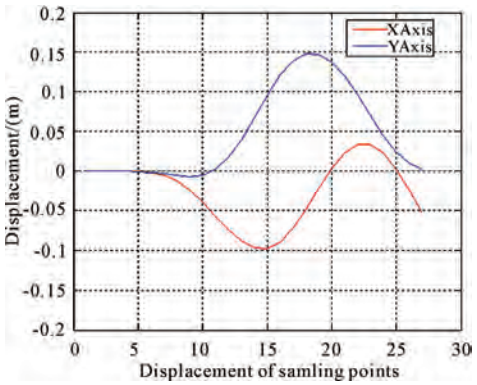

Figure 6. Displacement curve.

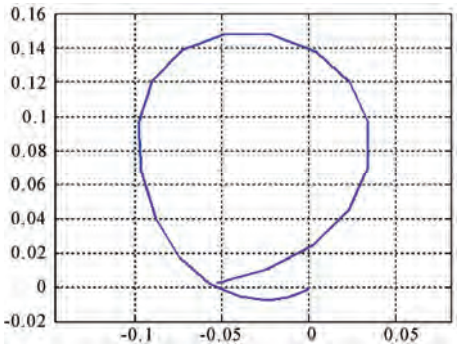

Figure 7. Contrail curve.

SciRes Copyright © 2010

obtain the corresponding curves of **Figure 5**. Similarly according to the **Eqs.1,8** and **11** we can obtain displacement curve from the velocity curve. After error correction a smooth curve of **Figure 6** is obtained, Last using the two displacement curves represents x, y-axis of the plane coordinate system respectively.

Therefore, in accordance with their corresponding points the contrail curve can be drawn on the plane coordinate system, as shown in **Figure 7**.

Other contrail identified pictures are shown in **Figure 8** and **Figure 9**:

6. CONCLUSIONS

In this paper a kind of handwriting detecting system based on MEMS inertia sensors is introduced. The system samples the pen's acceleration and attitude angles changes and then computes the movement contrail of pen, finally the recurrence of handwriting is finished. The test result validates correctness of the theory. The system is different with usual 2-D electronic pen system, its greatest strength is freely writing in 3-D space and this is the first case of the inertial navigation theory is

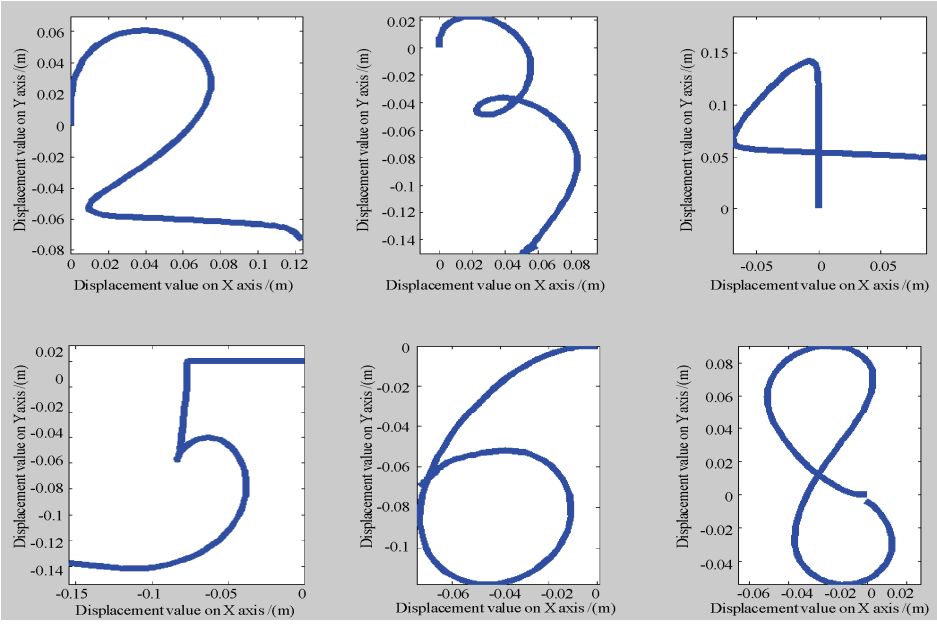

Figure 8. Number contrail.

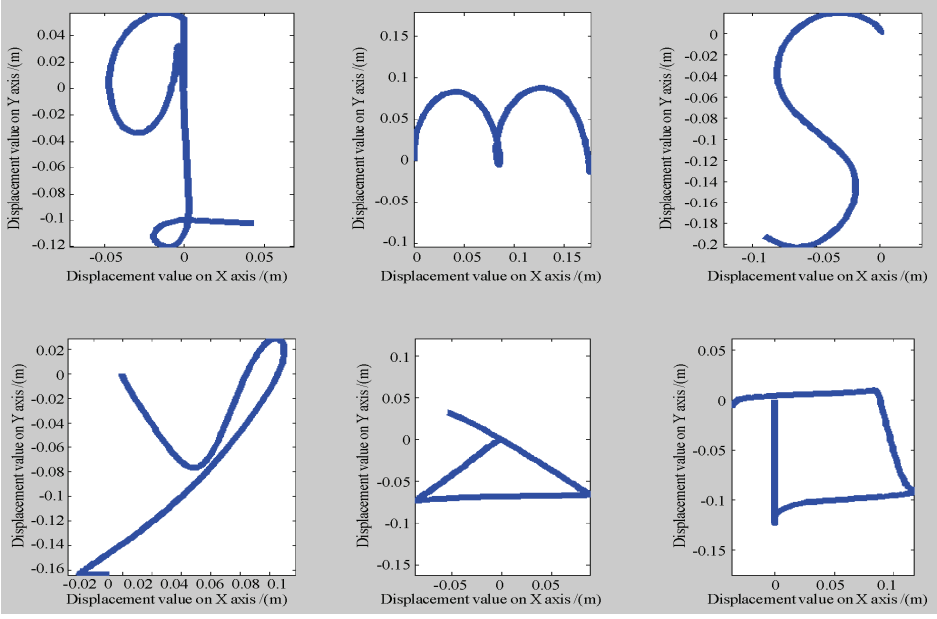

Figure 9. Letter and symbol contrail

SciRes Copyright © 2010

used for pen.

The next tasks will content sensors data fusion and the accumulate errors analysis of the double integral. Then the more accurate contrail can be gotten. In additional, a better algorithm of weights of gravitational acceleration removal is needed to look for, so that the more pure dynamic acceleration can be gotten.

7. ACKNOWLEDGEMENTS

This work was supported by Siemens China Research Center under Grant 40001014200611.

REFERENCES

[1] MiyakawaI, T., Yunezawan, *et al.* (2000) Character pattem reproduction from handwriting pen acceleration [J]. **(2)**, 671-679.

[2] Won-chul, B., Wook ch, Kyeong-ho, K., *et al.* (2003) Self-contained spatial input device for wearable computers [C]. *Proceedings of the 7th IEEE International Symposium on Wearable Computers*.

[3] GUANGL IE ZH G SH, YLUNL (2005) Towards an ubiquitous wireless digital instrument using MEMS motion sensing technology [C]. *Proceedings of the 2005 IEEE/ ASME*.

[4] Lam, A.H.F., Liw, J. (2002) MIDS: GUI and TUI in mid2 air using MEMS sensors [J]. *IEEE/RSJ International Conference*, **2**, 1184-1189.

[5] Humphreys, D. (2003) An input device for the control of 3D graphics [R]. *Birmingham: Final Report of University of Birmingham.*

[6] Zhang, S.X., Li, J. (1992) Strapdown inertial navigation system [M]. *Beijing: Defense Industry Press.*

[7] Hou, X.F., Liu, R., Zhou, Z.R. (2007) Application of accelerometer MMA7260 for abstraction of walking character [J]. *Chinese Journal of Sensors and Actuators*, **20(3)**, 507-511.

[8] Zhang, R.H., Jia, H.G., Chen, T. *et al*. (2008) Attitude solution of strapdown inertial navigation system based on the method of quaternions [J]. *Optics and Precision Engineering*, **30(10)**, 1963-1971 (in Chinese).

[9] Zhu, R., Zhou, Z.Y. (2002) An attitude measurement system based on MEMS [J]. *Measurement and Control Technology*, **21(10)**, 6-8 (in Chinese).

[10] Du, H.L., Zhang, R.H., Liu, P. *et al*. (2008) The attitude solution modules of strapdown inertial navigation system [J]. *Optics and Precision Engineering*, **29(10)**, 1956-1963 (in Chinese).

SciRes Copyright © 2010

Vol.2, No.1, 63-66 (2010)
doi:10.4236/ns.2010.21010

Natural Science

Photocurrents induced by stimulated absorption of light

Alexey Kavokin[1], Giuseppe Eramo[2]

[1]Physics and Astronomy School, University of Southampton, Highfield, Southampton, United Kingdom
[2]Dipartimento di Fisica, Universita di Roma II, via della Ricerca Scientifica, Rome, Italy

Received 23 October 2009; revised 13 November 2009; accepted 17 November 2009.

ABSTRACT

In organic materials absorption of light results in creation of the Frenkel excitons, Coulomb -bound electron-hole pairs having an integer spin. Being composite bosons, Frenkel excitons may accumulate in significant quantities in a single quantum state. The probability of photon absorption by such a state increases as (N+1) where N is the occupation number of the state. This enhancement is due to the stimulated absorption of light, which is a final-state stimulated process analogous to the well-known stimulated emission of light. We propose using the stimulated absorption for creation of solar cells of a record quantum efficiency. We are going to use the organic microspheres to accumulate the Frenkel excitons at the discrete frequencies corresponding to the photonic whispering gallery modes of the sphere. The dissociation of accumulated Frenkel excitons will be effectuated periodically using the transparent carbon contacts on a piezoelectric mechnical support.

Keywords: SolarCell; Photovoltaics; Exciton; Bose-EinsteinCondensation

1. INTRODUCTION

Development of the renewable sources of energy is a strategic economic priority nowadays. The solar energy is especially important for the tropical countries due to their favorable climate conditions. At present, the commercially available solar cells are based on silicon monocrystals which are relatively expensive and can hardly compete with the conventional energy sources therefore. Organic materials are widely discussed now as a valuable alternative to silicon but several obstacles still block the full-scale development of organic photovoltaics. First, unlike silicon, absorption of light in organics does not produce the free electron-hole pairs, but bound electrically neutral states known as Frenkel excitons. A significant external voltage needs to be applied to help dissociating the Frenkel excitons with formation of the unbound electrons and holes which contribute to the photocurrent [1]. Second, the metallic contacts used at present absorb light themselves which reduces significantly the quantum efficiency of photocells. The revolutionary improvement of the performance of the organic photocells due to the use of new materials and new physical effects is in the focus of this Letter. The starting idea is to take advantage of the bosonic properties of Frenkel excitons and use them to achieve the stimulated absorption of light. The photocells based on stimulated absorption are expected to posses a dramatically enhanced quantum efficiency with respect to traditional photocells based on the spontaneous absorption of light. The expected difference is as huge as the difference between a light emitting diode (producing light by spontaneous emission) and a laser source (producing light by stimulated emission). Furthermore, we take advantage of the experience accumulated in the recent years in production of the optically transparent electric contacts based on the diamond-like-carbon (DLC) with embedded carbon nanotubes and to operate with the organic microspheres characterized by the photonic whispering gallery modes of extremely high quality factors. We emphasize the important role of photonic confinement in our photocells, which allows for resonant generation of macroscopic number of Frenkel excitons in the same quantum state during the life-time of the corresponding photonic mode. In turn, once being created, the macroscopic population of Frenkel excitons reproduces itself by stimulated absorption of new solar photons. We propose a new technology based on a new physics, new structures and new materials. The targeted outcome is a new generation of photocells with a drastically improved quantum efficiency.

In 1917 Einstein has proposed the theory of radiation of atoms which accounted for three essential processes of light-matter interaction: the spontaneous emission of light, the spontaneous absorption of light by atoms and the stimulated emission of light. This latter process has found its use in the new coherent sources of light (lasers,

SciRes Copyright © 2010

from Light Amplification by Stimulated Emission of Radiation, which we frequently meet in the everyday life now). In lasers, generation of new photons by matter is stimulated by existing population of the photon mode in a laser cavity. The fourth essential process of light-matter coupling is the stimulated absorption of light. It may only take place in the systems where the absorbed photons generate bosonic quasiparticles, e.g. excitons. Excitons are Coulomb correlated electron-hole pairs, a direct analogy of hydrogen atoms, created inside inorganic semiconductor crystals due to resonant absorption of light at the energies slightly below the bandgap (Wannier-Mott excitons [2]) or in organic crystals at the energy below the HOMO-LUMO transition (Frenkel excitons [3]). While electrons and holes are fermions, the excitons possess integer spins and are composite bosons therefore. As such, the excitons can be accumulated in large quantities in a single quantum state, forming the Bose-Einstein condensate (BEC). Recently, multiple experimental evidences for the BEC of excitons coupled to light modes in semiconductor microcavities have been reported [4-6]. An exciton coherently coupled to a confined photon in a microcavity forms a so-called exciton-polariton. A new generation of semiconductor light sources called "polariton lasers" and based on the Bose-Einstein condensation of exciton-polaritons has been suggested and experimentally realized very recently [7,8].

2. STIMULATED ABSORPTION OF LIGHT BY EXCITONS

Creation of a new exciton in a quantum state already occupied by N excitons has a probability (N+1) times higher than creation of an exciton in an empty state. This is why the stimulated absorption of light by excitonic condensates is expected to be extremely efficient. Several conditions need to be met to ensure stimulated absorption: 1) the seed exciton population exceeding 1 must be created; 2) the life-time of the exciton state (accounting for its radiative and non-radiative life-times) must be longer than the generation rate of excitons. The first condition is readily satisfied due to the intensity fluctuations in the solar light: statistically, simultaneous excitation of two or more excitons is always possible within a sufficiently long time interval. The second condition can be satisfied if the intensity of incident light exceeds some critical intensity dependent on the exciton-life time. In this case the amplification of the seed population takes place, the exciton condensates stabilizes itself and the rate of stimulated absorption keeps steadily growing up to the saturation value dependent on the spectral density of incident light and the Mott transition threshold for the exciton system. Making use of the stimulated absorption of light would be a fundamental breakthrough in photovoltaics which may be compared with invention of lasers in optical lighting. The research in this direction is timely and relevant given the overall high interest to organics materials for photovoltaic applications in the world.

The qualitative analysis shows that the most important condition to be satisfied to ensure the stimulated absorption going on is a sufficiently long life-time of an exciton state of interest. Sufficiently long means about 100 ps according to our estimations based on the average intensity of the day-time light in the Mediterranian region. Another important practical issue is linked with a necessity to have a significant absorption within the large frequency range of the visible and near ultraviolet light, in order to avoid losses of the solar energy. This is partly resolved because of the natural inhomogeneous broadening of Frenkel exciton resonances in the most part of organic materials, which is of the order or several hundreds meV, typically. In order to further extend the frequency range of efficient stimulated absorption and to control the life-time of the concerned exciton states we propose using the organic microspheres as a main element of the solar cell. In is well known that dielectric or semiconductor microspheres are characterized by discrete optical spectra composed by a multitude of sharp resonances. These resonances are associated with so-called whispering gallery modes, i.e. the light modes confined near the surface of the microsphere (**Figure 1**). The whispering gallery modes of high orbital and magnetic indices may have a quality factor (ratio of the mode frequency to its linewidth) of the order of 10^5-10^6 which ensures the photonic life-time of 100 ps or more. In the same time, the finesse of these modes (ratio of the frequency splitting between different modes to the linewidth of the mode) remains quite low (of the order of several units). This is why a microsphere filled by an absorbing aggregate would absorb light at the huge multitude of discrete frequencies corresponding to the whispering gallery modes. The life-time of excitons coupled to each of these modes would be long enough to ensure stimulated absorption. Between these selected frequencies the absorption of light would be still spontaneous.

3. DEVICE CONCEPT

In order to cover the most part of the visible spectrum of light we propose to operate with the microspheres of different radii ranging from several microns to several tens of microns. Furthermore, in order to ensure efficient collection of the charge carriers accumulated in the microsphere due to stimulated absorption, we propose using the transparent contacts made of a diamond-like-carbon (DLC). Fabrication of such contacts which may serve as Fresnel lenses as well is now a registered know-how in Europe. The DSC cover layer would pro-

SciRes Copyright © 2010

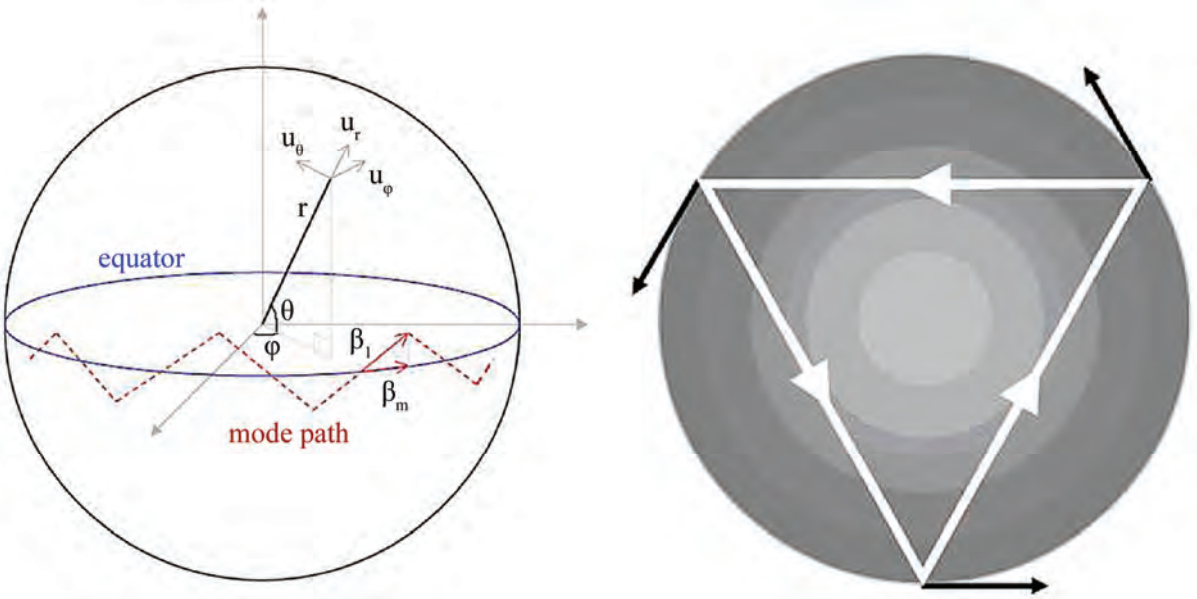

Figure 1. A dielectric sphere and the path of light in the whispering gallery mode (left); localization of light in a sphere due to multiple internal reflections (right).

tect the organic solar cell from chemical and mechanical damage, ensure focusing of light on the microsphere and play a role of a non-absorbing upper contact (see the scheme in **Figure 2**). In order to allow for efficient accumulation of Frenkel excitons inside the organic microsphere we plan discharging it periodically which could be achieved by placing the upper contact on a piezoelectric support which would extend and contract

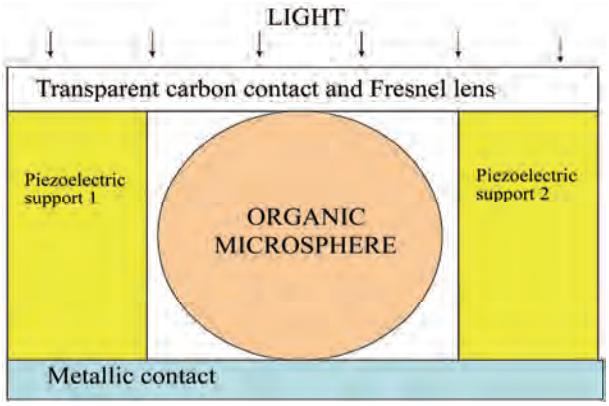

Figure 2. Scheme of the proposed photovoltaic device structure composed by an organic microsphere, where the Bose-Einstein condensate of exciton polaritons will be created by resonant optical pumping, a lower metallic contact and an upper transparent carbon contact supported by two piezoelectric pillars operating in a THz modulating regime: when the voltage between two contacts drops due to the current passing through the sphere the piezoelectric supports extend which leads to the break of current. As soon as the current is broken, the supports contract again, which allows for the new discharge of the microsphere etc.

with a Tera-Hertz frequency.

The proof-of-concept demonstration device would be a standard porphirine microsphere of the radius from 10 to 100 microns connected to two platinum microcontacts. One would measure a photocurrent generated by an accordable laser as a function of the frequency and the intensity of the laser light. A threshold-like superlinear dependence of the photocurrent as a function of the laser intensity at the discrete frequencies corresponding to the whispering gallery modes of the microsphere would be a "smoking gun" for the stimulated absorption. In the next phase the optimized microspheres would be assembled with the metallic and carbon contacts on the piezoelectric support. To improve the collection of solar light, the organic Fresnel lenses covered by a DSC protective film would be assembled on the top of the structure. The main risk at this stage is linked with the proposed discharge mechanism for the microspheres which has not yet been tested experimentally.

4. CONCLUSIONS

In conclusion, the recent advances in the Bose-Einstein condensation of excitons and exciton-polaritons open new horizons for the organic photovoltaics. A revolutionary concept of stimulated absorption of light may allow for a dramatic increase of the quantum efficiency of organic solar cells. In this Letter a device concept suitable for demonstration of photocurrents generated by stimulated absorption of light is proposed.

We acknowledge support from the EU IRSES grants

SciRes Copyright © 2010

"POLALAS" and "ROBOCON".

REFERENCES

[1] Kim, J., Lee, K., Coates, N., Moses, D., Nguyen, T., Dante, M., Heeger, A. (2007) Efficient tandem polymer solar cells fabricated by all-solution processing. *Science*, **222**, 317-5835.

[2] Mott, N.F. (1938) Conduction in polar crystals. II. The conduction band and ultra-violet absorption of alkali-halide crystals. *Trans. Faraday Soc*, **34**, 500.

[3] Frenkel, J. (1931) On the transformation of light into heat in solids. I, *Phys. Rev.* **3,** 17.

[4] Kasprzak, J. *et al*. (2006) Bose-einstein condensation of exciton polaritons. *Nature*, **443**, 409.

[5] Balili, R., Hartwell, V., Snoke, D., Pfeiffer, L. and West, K. (2007) Bose-einstein condensation of microcavity polaritons in a trap. *Science*, **316**, 1007.

[6] Lai, C.W., Kim, N.Y., Utsunomiya, S., Roumpos, G., Deng, H., Fraser, M.D., Byrnes, T., Recher, P., Kumada, N., Fujisawa, T. and Yamamoto, Y. (2007) Coherent zero-state and pi-state in an exciton-polariton condensate array. *Nature*, **450**, 529.

[7] Christopoulos, S. *et al*. (2007) Room temperature polariton lasing in semiconductor microcavities. *Phys. Rev. Lett.* **98**, 126405.

[8] Christmann, G. *et al*. (2008)Room temperature polariton lasing in a GaN/AlGaN multiple quantum well microcavity. *Appl. Phys. Lett.* **93**, 051102.

SciRes Copyright © 2010

Call for Papers

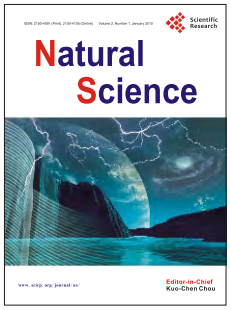

Natural Science

A Journal Published by Scientific Research Publishing, USA
www.scirp.org/journal/ns

Editor-in-Chief

Prof. Kuo-Chen Chou	Gordon Life Science Institute, San Diego, California, USA

Editorial Board

Fridoon Jawad Ahmad	University of the Punjab, Pakistan
Giangiacomo Beretta	University of Milan, Italy
Bikas K. Chakrabarti	Saha Institute of Nuclear Physics, India
Dr. Brian Davis	Research Foundation of Southern California, USA
Mohamadreza Baghaban Eslaminejad	Cell Sciences Research Center, Royan Institute, Iran
Dr. Marina Frontasyeva	Frank Laboratory of Neutron, Russia
Neelam Gupta	National Bureau of Animal Genetic Resources, India
Dr. Yohichi Kumaki	Institute for Antiviral Research, Utah State University, USA
Dr. Petr Kuzmic	BioKin Ltd., USA
Dr. Ping Lu	Communications Research Centre, Canada
Dimitrios P. Nikolelis	University of Athens, Greece
Caesar Saloma	University of the Philippines Diliman, Philippines
Prof. Kenji Sorimachi	Dokkyo Medical University, Japan
Swee Ngin Tan	Nanyang Technological University, Singapore
Dr. Fuqiang Xu	National Magnetic Resonance Research Center, China
Dr. W.Z. Zhong	Pfizer Global Research and Development, USA

Editorial Advisory Board

Prof. James J. Chou	Harvard Medical School, USA
Prof. Reba Goodman	Columbia University, USA
Dr. Robert L. Heinrikson	Heinrikson, Proteos, Inc., USA
Prof. Robert H. Kretsinger	University of Virginia, USA
Dr. P. Martel	Chalk River Laboratories, AFCL Research, Canada
Dr. Michael Mross	Vermont Photonics Technologies Corp., USA
Prof. Harold A. Scheraga	Baker Laboratory of Chemistry, Cornell University, USA

Natural Science is an international journal dedicated to the latest advancement of natural sciences. The goal of this journal is to provide a platform for scientists and academicians all over the world to promote, share, and discuss various new issues and developments in different areas of natural sciences. All manuscripts must be prepared in English, and are subject to a rigorous and fair peer-review process. Accepted papers will immediately appear online followed by printed hard copy. The journal publishes original papers including but not limited to the following fields:

- **Astronomy & Space Sciences**
  - Astronomy
  - Astrophysics
  - Atmospheric Science
  - Space Physics
- **Earth Science**
  - Geography
  - Geology
  - Geophysics/Geochemistry
  - Oceanography
- **Chemistry**
  - Analytical Chemistry
  - Biochemistry
  - Computational Chemistry
  - Inorganic Chemistry
  - Organic Chemistry
  - Physical Chemistry
- **Life Science**
  - Cell Biology
  - Computational Biology
  - Genetics
  - Immunology
  - Medicine/Diseases
  - Microbiology
  - Molecular Biology
  - Neuroscience
  - Pharmacology/Toxicology
  - Physiology
  - Psychology
  - Virology
- **Physics**
  - Applied Physics
  - Atomic, Molecular, and Optical Physics
  - Biophysics
  - High Energy/Particle Physics
  - Material Science
  - Plasma Physics
- **Others**
  - Education
  - History of Science
  - Science and Innovations

We are also interested in: 1) Short Reports—2-5 page papers where an author can either present an idea with theoretical background but has not yet completed the research needed for a complete paper or preliminary data; 2) Book Reviews—Comments and critiques.

Notes for Intending Authors

Submitted papers should not be previously published nor be currently under consideration for publication elsewhere. Paper submission will be handled electronically through the website. For more details, please access the website.

Website and E-Mail

http://www.scirp.org/journal/ns ns@scirp.org

Natural Science, 2010, 2, 1-66
Published Online January 2010 in SciRes (http://www.scirp.org/journal/ns).

TABLE OF CONTENTS

Volume 2, Number 1, January 2010

Predicting numerically the large increases in extra pressure drop when Boger fluids flow through axisymmetric contractions
H. R. Tamaddon-Jahromi, M. F. Webster, K. Walters..... 1

Synthesis of nano crystalline spatulae of lead zirconate titanate ($PbZr_{0.52}Ti_{0.48}O_3$)
S. S. Bhatt, S. C. Chaudhry, N. Sharma, S. Gupta..... 12

Hydriding and dehydriding kinetics of melt spun nanocrystalline $Mg_{20}Ni_{10-x}Cu_x$ (x=0-4) alloys
Y. H. Zhang, D. L. Zhao, B. W. Li, H. P. Ren, S. H. Guo, X. L. Wang..... 18

Study of some Indian medicinal plants by application of INAA and AAS techniques
R. Lokhande, P. Singare, M. Andhele, R. Acharya..... 26

Toxicity evaluation of produced formation waters after filtration treatment
L. Manfra, C. Maggi, J. Bianchi, M. Mannozzi, O. Faraponova, L. Mariani, F. Onorati, A. Tornambè, C. V. Lamberti, E. Magaletti..... 33

Review on nano-drugs
Y. Liu, T. S. Niu, L. Zhang, J. S. Yang..... 41

Face recognition based on manifold learning and Rényi entropy
W. M. Cao, N. Li..... 49

Relationship between normalized thermal energy and conductivity for cylindrical tokamak geometry
M. Asif..... 54

Research of handwriting detecting system for space pen
Z. Y. Gao, D. S. Li, W. Wang, C. J. Yang..... 56

Photocurrents induced by stimulated absorption of light
A. Kavokin, G. Eramo..... 63

Copyright©2010 SciRes

ISSN: 2150-4091